Laser Cooling and Trapping of Yb and Rb Atoms Towards Quantum Computing

A
Thesis Submitted
in Partial Fulfillment of the Requirements
for the Degree of

Doctor of Philosophy

by

Thilagaraj R
(206121036)

Department of Physics
Indian Institute of Technology Guwahati
Guwahati, Assam - 781039

June 2026


भारतीय प्रौद्योगिकी संस्थान गुवाहाटी
Indian Institute of Technology Guwahati

DECLARATION

I, hereby, declare that the thesis entitled **"Laser Cooling and Trapping of Yb and Rb Atoms Towards Quantum Computing"**, submitted by me to the Indian Institute of Technology Guwahati, for the award of the degree of Doctor of Philosophy, is a bonafide work carried out by me under the supervision of Dr. Kanhaiya Pandey. The content of this thesis, in full or in parts, has not been submitted to any other University or Institute for the award of any degree or diploma. I also wish to state that to the best of my knowledge and understanding, nothing in this report amounts to plagiarism.

Thilagaraj R
Roll No.: 206121036
Department of Physics
Indian Institute of Technology Guwahati
Guwahati, Assam – 781039

CERTIFICATE

This is to certify that the thesis entitled **"Laser Cooling and Trapping of Yb and Rb Atoms Towards Quantum Computing"**, submitted by **Thilagaraj R** (206121036), a Ph.D. scholar in the Department of Physics, Indian Institute of Technology Guwahati, for the award of the degree of Doctor of Philosophy, is a record of an original research work carried out by him under my supervision and guidance. The thesis has fulfilled all requirements as per the regulations of the institute and in my opinion, has reached the standard needed for submission. The results embodied in this thesis have not been submitted to any other University or Institute for the award of any degree or diploma.

Dr. Kanhaiya Pandey
Associate Professor
Department of Physics
Indian Institute of Technology Guwahati
Guwahati, Assam – 781039

ABSTRACT

Neutral atom systems form an important platform for quantum computing and quantum simulation due to the scalability and controllability enabled by optical trapping and manipulation techniques. Laser cooling and trapping provide essential tools for preparing and controlling such systems. In this thesis, we present an experimental and theoretical study of laser cooling and trapping of neutral Yb and Rb atoms.

We demonstrate magneto-optical traps (MOT) for Yb operating on the 399 nm and 556 nm transitions, with particular emphasis on the direct loading of a green MOT using the narrow intercombination transition at 556 nm. We achieve direct loading of the green MOT by superimposing the green laser beam within the hollow core of the blue MOT beam. Using this core-shell configuration, we load up to 3.4×10^8atoms within 1 s. We also investigate an alternative center-shifted dual-MOT configuration, in which we shift the overlap region of the blue MOT toward the Zeeman slower. Although this configuration avoids loss of blue laser power, it yields a lower atom number of approximately 2×10^7.

In parallel, we carry out experimental studies with Rb atoms that are central to neutral-atom quantum computing architectures. We demonstrate single-atom trapping in an optical dipole trap, a building block for neutral-atom quantum computing. We investigate electromagnetically induced transparency (EIT) involving Rydberg state in a thermal Rb vapor cell. We study EIT in a V+inverted Ξ system ($5S_{1/2} \rightarrow 5P_{3/2}$ and $5S_{1/2} \rightarrow 6P_{1/2}$ $\rightarrow r = 69D_{3/2}$) using probe and control lasers at 780 nm, 421 nm, and 1003 nm. This configuration exhibits a high signal-to-noise ratio at room temperature with a linewidth of about 9 MHz. For completeness and comparison, we also study EIT in an inverted Ξ system using the $5S_{1/2} \rightarrow 6P_{1/2} \rightarrow 69D_{3/2}$ transitions.

PUBLICATIONS

List of journal publications resulting from the work reported in this thesis:

[1] **Thilagaraj Ravi**, Rajnandan Choudhury Das, Samir Khan, Heramb Vivek Bhusane, and Kanhaiya Pandey, **"EIT in V+inverted Ξ system using Rydberg state in thermal Rb atoms,"** *Optics Communications* **597** (2025), 132592.

[2] **Thilagaraj Ravi**, Rajnandan Choudhury Das, Heramb Vivek Bhusane, Samrat Roy, and Kanhaiya Pandey, **"Efficient direct loading of the green MOT of Yb with low green laser power,"** *Physics Letters A* **577** (2026), 131429.

Additional publications:

[1] Rajnandan Choudhury Das, **Thilagaraj Ravi**, Samir Khan, and Kanhaiya Pandey, **"Continuous loading of a magneto-optical trap of rubidium using a narrow transition,"** *Phys. Rev. A* **109**, 063107 (2024).

[2] Rajnandan Choudhury Das, **Thilagaraj Ravi**, Samir Khan, and Kanhaiya Pandey, **"Role of spontaneously transferred coherence in laser cooling,"** *Phys. Rev. A* **110**, 033101 (2024).

[3] Rajnandan Choudhury Das, Samir Khan, **Thilagaraj Ravi**, and Kanhaiya Pandey, **"Direct spectroscopy of rubidium using a narrow-line transition at 420 nm,"** *Eur. Phys. J. D* **78**, 40 (2024).

Dedicated to my beloved father

ACKNOWLEDGEMENTS

First, I would like to express my sincere gratitude to my PhD supervisor, Dr. Kanhaiya Pandey, for his constant guidance and support throughout my doctoral research. I have always admired his reasoning and logical approach to problem-solving. Working with him has shown me how effective experimental research can be carried out even with limited resources. He has been a source of guidance during experimental challenges, and his ability to remember even minor experimental details discussed long ago has often helped resolve issues efficiently.

Next, I would like to thank my doctoral committee members, Dr. Pankaj Kumar Mishra, Prof. Bosanta R. Boruah, and Dr. Arif Warsi Laskar, as well as former committee members Dr. Tapan Mishra and Prof. Gagan Kumar, for their support and valuable feedback.

I express my sincere gratitude to Prof. Gagan Kumar, Prof. Alika Khare, and Prof. Bosanta R. Boruah for kindly allowing me to borrow various instruments from their laboratories whenever required. I acknowledge the support, guidance, and advice provided by the Heads of the Department, as well as by the faculty and staff members, during the course of my doctoral studies.

I consider myself fortunate to have seniors, Dr. Dangka Shylla and Dr. Rajnandan Choudhury Das, who provided constant support and valuable insights during challenging phases of my PhD. I sincerely thank Dr. Rajnandan Choudhury Das for helping me feel comfortable on campus on my first day in the laboratory. I have always admired his kindness and depth of subject knowledge. I am also thankful for the discussions we had on experimental problems, which contributed to a better understanding of experimental challenges and possible solutions.

I thank my lab members, Samir, Samrat, Noman, Dr. Mrigankadeep, Dr. Sajia, Abhiram, and Naveen, for their support and cooperation, and for fostering a friendly and positive laboratory environment. I also extend my gratitude to former lab members Arka, Heramb, Chiranta, Deepak, and Dr. Bilal.

I am sincerely grateful to IIT Guwahati for providing the necessary support, facilities, and resources, including the Institute Fellowship and access to the Central Workshop.

A heartfelt thanks to my friends Pradeep, Thirukumaran, Kannan, Giridhar, Jeeva, Allan, Vishwa, Deepika, Naveen, Jenny, Shanmugam, Stuti, Ajay, Sushanth, Dharshini, and Priyanka. Their friendship helped me momentarily step away from the struggles of my PhD and brought much-needed balance to my doctoral journey. Through countless shared moments on campus, ranging from weekend movie nights and morning badminton sessions to long conversations, they helped me appreciate and enjoy life during this phase, and supported me in coping with the challenges of the PhD. I would also like to thank the IITG Tamil Sangam for making IIT Guwahati feel like home during festival times and for helping me not miss home.

I would like to thank my M.Sc. friends, Pavithra Kumar, Naan Karthick, Ramesh (Jemini), Suresh, and Thirumoorthy (Mamooty) for their support and for making my M.Sc. years memorable. I also express my sincere gratitude to my M.Sc. mentors, Gopi Anna and Dillip Anna, for their encouragement and guidance.

Last but not least, I would like to express my heartfelt gratitude to my parents and my brother for their constant support and encouragement. Without them, my doctoral journey would not have been possible. I am deeply grateful for the sacrifices made by all three of them, whose patience, understanding, and unwavering belief in me sustained me throughout this journey.

Contents

List of Figures

List of Tables

1

Introduction

Contents

1.1 Introduction

Classical computers have become an integral part of modern life because we rely on them for many tasks, ranging from simple math calculations to complex scientific simulations. They operate using binary logic, where information is stored in bits that take the values 0 or 1. These bits form the basic unit of computation. By combining many bits, a computer can represent and process any kind of information. While classical computers have transformed modern life, their performance is limited when working with some complex tasks such as the factorization of large integers, the search and optimization of large datasets, and the accurate simulation of quantum many-body systems. For such problems, even the fastest supercomputers become ineffective because the memory and computation time required increase beyond any feasible bound. Solving these problems is not only of theoretical interest but also of great practical importance. Efficient factorization would have a direct impact on cryptographic security, which underpins digital communication and data protection. Faster search and optimization methods would benefit fields such as finance, logistics, and machine learning. Accurate simulations of quantum many-body systems would open pathways to designing new materials, understanding physics and chemical reactions at a fundamental level, and developing new drugs. Together, these applications show why overcoming the limits of classical computing is so crucial.

This challenge naturally leads to the development of quantum computing, which provides new ways of processing information. Quantum computing helps by using the unique principles of quantum mechanics to process information in ways that are not possible for classical machines. A quantum bit, or qubit, can exist in a superposition of states, which allows a quantum computer to explore many possibilities at once. Entanglement creates strong correlations between qubits, enabling coordinated operations across the system. Interference can then be used to enhance the probability of correct solutions while suppressing incorrect ones. Together, these features make it possible to design algorithms that outperform their classical counterparts. Although the conceptual foundations of quantum computing were laid in the 1980s, with Feynman highlighting the idea of quantum simulation [1], and Deutsch proposing the notion of a universal quantum computer [2], it was during the 1990s that the pursuit of building practical quantum devices began in earnest. This shift was driven by key algorithmic advances, most notably Shor's algorithm for efficient factorization [3] and Grover's algorithm for quantum search [4], which demonstrated clear advantages over classical computation. Moreover, the first proof-of-principle experiments were carried out using small systems such as trapped ions [5] and nuclear magnetic resonance [6, 7], providing tangible evidence that a quantum computer could be realized in the laboratory. Since then, the field has grown rapidly, with multiple physical platforms being pursued.

Any well-isolated physical system with at least two well-defined states can be utilized to encode a qubit. However, encoding a qubit is only the starting point, as realizing practical quantum computation imposes further demands on the physical platform. These requirements are systematically captured by the DiVincenzo Criteria, proposed by David P. DiVincenzo in 2000 [8], which define five necessary conditions for quantum computation: (1) a scalable physical system with well-characterized qubits, (2) the ability to initialize qubits to a known fiducial state, (3) long coherence times relative to gate operation times, (4) a universal set of quantum gates, and (5) qubit-specific measurement capability. Superconducting circuits, trapped ions, neutral atoms, photonic systems, and nitrogen-vacancy centers represent the leading physical implementations, each addressing these criteria through different physical mechanisms and with their own advantages and limitations. Among these, superconducting quantum circuits are one of the most advanced platforms. They use microwave circuits made from superconducting materials. The qubit is created by combining superconducting microwave circuits with Josephson junctions, which introduce the nonlinearity needed to define the quantum states [9, 10]. Superconducting qubits are industry-friendly because the fabrication follows standard lithography and can be produced with techniques similar to semiconductor manufacturing. They are also easy to integrate with control electronics. However, they require cryogenic temperatures for stable operation. Further, the qubits are not identical due to fabrication variations and require individual calibration. The coherence time is relatively shorter compared to other platforms, but it can be improved by using materials like tantalum in transmon qubits [11–13]. IBM invests heavily in the development of quantum computing based on superconducting platforms [14–17].

Trapped ions are another major and well-established platform for quantum computing. In this platform, ions such as Ca^+, Ba^+, and Yb^+ are trapped using electromagnetic traps such as Paul traps or Penning traps. The qubit states are encoded in the internal energy levels of the ions and manipulated using lasers. They offer high-fidelity gate operations but have slower gate times compared to superconducting qubits [18, 19]. Further, scaling to long ion chains is challenging due to motional-mode crowding [20]. In order to overcome this limitation and support larger trapped-ion quantum processors, several solutions have been proposed, including modular architectures connected through photonic links [21], segmented traps such as the quantum charge-coupled device (QCCD) architecture that move ions between different regions [22], and 2D surface-electrode traps. Companies such as Quantinuum and IonQ develop large-scale trapped-ion quantum processors [23, 24].

Another important platform for quantum computing is based on photonic systems [25, 26]. This platform uses the quantum states of light as qubits. The states are controlled and manipulated using optical components such as waveguides, phase shifters, and beam splitters [27]. This platform is excellent for quantum communication and networking because photons travel long distances with very little loss and do not interact strongly with the environment. They also allow easy transmission through optical fibers, which makes them suitable for distributed quantum networks. Industries such as PsiQuantum, Quandela, Xanadu, and ORCA Computing are developing photonic quantum processors using integrated photonic chips, deterministic photon sources, and continuous-variable architectures [28–30].

Nitrogen-vacancy centers are another evolving platform for quantum computing because of their atom-like properties and long-lived spin quantum states in a solid-state system [31]. The qubit is encoded in the electronic spin of the defect and can be initialized and read out optically. However, creating identical NV centers is difficult, and large-scale integration remains challenging.

Over the past two decades, neutral atoms have developed into a versatile platform for both quantum computation and simulation [32–42]. The neutral-atom approach is considered especially promising due to its scalability and precise control of large qubit arrays using laser fields. Neutral atoms are natural qubits and can be scaled to large systems because they do not interact with each other unless interactions are deliberately introduced. However, this lack of interaction was initially viewed as a limitation because strong interactions are required for fast multi-qubit operations. In 2000, a group of researchers proposed that fast multi-qubit gates could be implemented using strong dipole–dipole interactions by exciting atoms to Rydberg states [43]. When two atoms are placed within a certain distance, the excitation of one atom to a Rydberg state can block the excitation of the other due to the strong dipole–dipole interaction between Rydberg states. This effect is known as the Rydberg blockade, and it plays a central role in neutral-atom quantum computing [32–34].

The first step toward neutral-atom quantum computing is the laser cooling and trapping of atoms to the microkelvin regime. Laser cooling reduces the thermal motion of atoms so they can be localized and controlled with high precision. After cooling, a single atom can be isolated or confined using optical tweezers or optical lattices. Optical tweezers use a tightly focused laser beam to trap individual atoms, and they allow flexible rearrangement and reconfiguration of atomic arrays [35–37]. Optical lattices use interfering laser beams to create a periodic potential, which can hold large numbers of atoms in a regular structure [44]. These trapping methods enable individual-site control and manipulation of atoms, which is essential for performing single-qubit and two-qubit gate operations [45, 46]. The trapped atoms using optical tweezers and optical lattices form the basis of neutral-atom quantum computing.

Alkali metals such as rubidium (Rb) and cesium (Cs) are widely used in neutral-atom quantum computing [38, 40, 41, 45, 46]. They have simple electronic structures with a single valence electron, which makes laser cooling and state preparation straightforward. These atoms also have well-characterized Rydberg states that enable strong dipole–dipole interactions for fast two-qubit gates.

Alkaline-earth and alkaline-earth-like elements such as strontium (Sr) and ytterbium (Yb) are also promising candidates. They have two valence electrons, which produce additional narrow optical transitions that are useful for high-precision cooling and long-lived qubit states. These narrow-line transitions allow lower temperatures, reduced decoherence, and high-fidelity state preparation. For this reason, Sr and Yb systems are being actively explored for both quantum computing [47–50] and quantum simulation, and they provide new opportunities for clock-state qubits and advanced cooling techniques [51, 52].

Several companies have focused on developing neutral-atom quantum technology. QuEra uses Rydberg neutral atoms in large tweezer arrays and has demonstrated processors with over 300 qubits and fault-tolerant logical qubits [53, 54]. Pasqal develops analog and digital quantum processors based on Rydberg-atom arrays [55]. Atom Computing uses alkaline-earth atoms such as Yb and has demonstrated systems with more than 1,000 qubits using optical lattice geometries [56, 57]. These advances show that neutral-atom technology has moved beyond laboratory research and is progressing toward commercial quantum processors.

Motivated by the rapid progress of neutral-atom quantum computing, this thesis investigates laser cooling and trapping techniques and spectroscopic methods using Yb and Rb atoms relevant to neutral-atom quantum computing platforms.

For Yb, this thesis includes the demonstration of magneto-optical traps (MOT) operating on the 399 nm (blue) and 556 nm (green) transitions. Mainly, we focus on the direct loading of Yb atoms in MOT using the intercombination narrow optical transition $6s^2\ ^1S_0 \rightarrow 6s6p\ ^3P_1$ at 556 nm (green MOT). The practical motivation of this work lies in loading the green MOT at low green laser power. Achieving high green power typically requires cavity-enhanced frequency doubling, which adds significant optical and mechanical complexity, whereas green powers of a few tens of milliwatts can be obtained using a simpler single-pass frequency-doubling scheme. For applications such as portable atomic clocks and compact quantum devices, avoiding a frequency-doubling cavity is therefore highly desirable. Direct loading of the green MOT is achieved by superimposing the green laser beam inside a hollow core of the laser beam driving the broad $6s^2\ ^1S_0 \rightarrow 6s6p\ ^1P_1$ transition (blue) at 399 nm. We load up to 3.4×10^8 atoms in 1 s. We characterize the green MOT loading with various experimental parameters such as magnetic field gradient, power of the green and blue MOT lasers, and detuning of the green laser. We have also loaded the green MOT using a center-shifted dual MOT configuration. In this configuration, the overlap region of the three counter-propagating blue laser beams is shifted towards the Zeeman slower, where the magnetic field is non-zero. The atoms are first pre-cooled and partially trapped in the blue MOT. These atoms enter the green MOT region and are trapped. In this method, unlike in the core-shell MOT, we do not lose blue MOT laser power due to masking of the central region. However, we load only 10^7 atoms, which is one order of magnitude lower than that in the core-shell MOT. This study will be useful for developing compact and power-efficient Yb systems, including portable optical clocks and experiments with optical tweezer arrays.

For Rb, this thesis begins with the demonstration of single-atom trapping in an optical dipole trap, as a trapped single atom in an optical tweezer is the basic building block of neutral-atom quantum computing platforms. We demonstrate the successful trapping of Rb atoms in the optical dipole trap (ODT) with various beam waists. While further technical development is required to achieve long-term robust single-atom trapping in the current setup, the present work provides important experimental understanding relevant to single-atom trapping. Further, the thesis investigates electromagnetically induced transparency (EIT) involving the Rydberg state in a Rb vapor cell. Rydberg excitation using blue and IR transitions is an advantageous path for quantum computation in alkali elements. Aiming to stabilize the IR laser for quantum computation, we study electromagnetically induced transparency (EIT) spectrum using Rydberg state in V+inverted Ξ system ($5S_{1/2} \rightarrow 5P_{3/2}$ and $5S_{1/2} \rightarrow 6P_{1/2} \rightarrow r = 69D_{3/2}$) in Rb vapor cell at room temperature. The probe laser absorption at 780 nm is monitored in the presence of the two control lasers at 421 nm and 1003 nm. In comparison to the previously studied inverted Ξ system, this system has a good signal-to-noise ratio even at room temperature with a similar linewidth (around 9 MHz). We also observe Autler-Townes splitting of the EIT due to the high power of the probe and blue control lasers. For completeness and comparison, we also study the EIT in an inverted Ξ system using $5S_{1/2} \rightarrow 6P_{1/2} \rightarrow 69D_{3/2}$ transitions.

1.2 Thesis outline

This thesis presents a study of laser cooling and trapping of neutral Yb and Rb atoms, with a focus on applications in quantum technologies, especially quantum computing. The thesis consists of seven chapters, which are briefly described below.

Chapter 1, titled *Introduction*, discusses the motivation for neutral-atom quantum technologies. In this chapter, we introduce different quantum computing platforms and explain why neutral atoms are promising candidates. We also summarize the overall structure of the thesis.

Chapter 2, titled *Theoretical Framework*, presents the basic theory of atom–light interaction using a semiclassical approach. We begin with the two-level atom model and introduce the dressed-state picture. We then discuss dipole forces, optical dipole potentials, and light shifts in multi-level atoms. Finally, we describe the theory of single-atom loading and the fundamentals of Rydberg atoms, including Rydberg–Rydberg interactions and the Rydberg blockade.

Chapter 3, titled *Experimental Details of the Yb Setup*, describes the design and construction of the ytterbium experimental system. We present the vacuum apparatus, oven section, Zeeman slower, MOT chamber, and the bake-out procedure. We further describe the spectroscopic chamber, MOT coil system, and the design and testing of the Zeeman slower. The chapter also details the 399 nm, 556 nm and 507 nm laser systems used for Yb cooling and excitation.

Chapter 4, titled *Yb Experiments*, presents the experimental results obtained with Yb atoms. We discuss the loading and operation of the blue MOT using the 399 nm transition and the direct loading of the green MOT using the 556 nm transition. We describe the optical setup, theoretical considerations, and experimental results for the green MOT. We also present efforts toward observing three-photon Rydberg excitation in Yb.

Chapter 5, titled *Microscopic Optical Dipole Trap of Rb Atoms*, presents the design and implementation of a microscopic optical dipole trap for Rb atoms. We describe the vacuum systems, laser stabilization, MOT operation, and sub-Doppler cooling. We also discuss the loading of the dipole trap, single-atom trapping, and the technical improvements required to achieve better loading efficiency.

Chapter 6, titled *EIT in V+Inverted Ξ and Inverted Ξ Systems Using Rydberg State in Thermal Rubidium Atoms*, presents an experimental investigation of electromagnetically induced transparency involving Rydberg state in Rb atoms. We study the V+Ξ and inverted Ξ configurations separately. For each configuration, we present the experimental setup and discuss the observed EIT features in detail.

Chapter 7, titled *Conclusions and Future Work*, summarizes the main findings of this thesis. We also outline possible directions for future research in quantum computing using Yb and Rb atoms.

2

Theoretical Framework

Contents

This chapter presents the theoretical concepts relevant to the experiments described in this thesis. It begins with the basic principles of atom–light interaction, which form the foundation for laser cooling and trapping. The mechanisms of Doppler and sub-Doppler cooling are discussed elsewhere [58, 59] and are not covered here. In this chapter, we focus on the theory of optical dipole traps and the associated AC Stark shift. An overview of Rydberg interactions is also included, as these interactions play an important role in achieving quantum control and entanglement between neutral atoms.

2.1 Atom-light interaction

The interaction between atoms and light forms the foundation of laser cooling and trapping techniques [60, 61]. When atoms are exposed to near-resonant light, they experience momentum exchange through repeated absorption and spontaneous emission of photons. This process gives rise to forces that can alter both the internal and external states of the atom. The two key components of this interaction are the scattering (radiation pressure) force and the dipole (gradient) force, which together determine how light can manipulate atomic motion.

To study atom–light interactions, three theoretical frameworks can be used: the classical, semiclassical, and fully quantum pictures [61–63]. In the classical picture, both the atom and the light field are treated as classical systems [64]. This description is suitable for studying the interaction of light with macroscopic media and for analyzing macroscopic effects such as radiation pressure and dispersion. It also provides a qualitative understanding of optical forces that form the basis of laser cooling and trapping. The classical picture works well in the weak-excitation limit, because the atom behaves like a driven harmonic oscillator, and the electromagnetic field can be approximated as a continuous wave when many photons are present. However, to describe absorption, emission, or saturation correctly, the quantum nature of the atom (and eventually of light) must be included.

In the semiclassical picture, the atom is treated quantum mechanically, while the light field is treated classically [60, 61]. The energy levels of atoms are quantized, and the light can be represented as a classical electromagnetic wave characterized by its amplitude, frequency, and polarization. The semiclassical description is required to correctly explain laser cooling and trapping phenomena, as these processes depend on quantized absorption–emission cycles and population dynamics between atomic states.

This approach fails when it is necessary to describe photon statistics, non-classical states of light, and entangled states. In such cases, the fully quantum picture is required, where both the atom and the light field are quantized [62, 63]. In the following section, we use a semiclassical approach to describe the origin of the dipole force.

2.1.1 Two-level atom in a classical field

We consider a two-level atom with a ground state $|g\rangle$ and an excited state $|e\rangle$ separated by an energy difference of $\hbar\omega_0$. The atom interacts with a classical monochromatic light field of angular frequency ω_L. The total Hamiltonian of the system can be expressed as

$$H = H_0 + H_\mathrm{AF}, \tag{2.1.1}$$

where $H_0 = \hbar\omega_0 \left|e\right\rangle \left\langle e\right|$ is the bare atomic Hamiltonian (the ground-state energy is taken as zero), and H_{AF} represents the atom–field interaction Hamiltonian given by

$$H_{\mathrm{AF}} = -\,\mathbf{d}\cdot\mathbf{E}. \tag{2.1.2}$$

Here, $\mathbf{d} = -e\,\mathbf{r}$ is the electric dipole moment operator of the atom, where e is the electron charge and $\mathbf{r}$ is the position operator of the electron relative to the nucleus. We consider a classical monochromatic plane electromagnetic wave and the corresponding electric field can be written as

$$\begin{aligned}\mathbf{E}(t) &= \hat{\varepsilon}\frac{E_0}{2}\left(e^{-i\omega_{\mathrm{L}}t} + e^{i\omega_{\mathrm{L}}t}\right)\\ &= \mathbf{E}_0^{(+)}e^{-i\omega_{\mathrm{L}}t} + \mathbf{E}_0^{(-)}e^{i\omega_{\mathrm{L}}t}\\ &= \mathbf{E}^{(+)}(t) + \mathbf{E}^{(-)}(t),\end{aligned} \tag{2.1.3}$$

where $\hat{\varepsilon}$ denotes the polarization unit vector and E_0 is the field amplitude.

The spatial dependence of the field is neglected under the electric dipole approximation, which assumes that the wavelength of the light is much larger than the size of the atom.

The atomic dipole operator can also be decomposed into positive and negative frequency components as the electric field,

$$\begin{aligned}\mathbf{d} &= \langle g|\mathbf{d}|e\rangle(\sigma + \sigma^\dagger)\\ &= \mathbf{d}^{(+)} + \mathbf{d}^{(-)},\end{aligned} \tag{2.1.4}$$

where $\sigma = \left|g\right\rangle \left\langle e\right|$ and $\sigma^\dagger = \left|e\right\rangle \left\langle g\right|$ are the lowering and raising operators, respectively. The operators $\mathbf{d}^{(+)}$ and $\mathbf{d}^{(-)}$ correspond to the positive and negative frequency components of the dipole operator,

$$\mathbf{d}^{(+)} \propto \sigma, \qquad \mathbf{d}^{(-)} \propto \sigma^\dagger. \tag{2.1.5}$$

This decomposition is motivated by the time dependence of these operators under the unperturbed atomic Hamiltonian $H_0 = \hbar\omega_0 \left|e\right\rangle \left\langle e\right|$. In the interaction picture, the lowering and raising operators evolve as

$$\sigma(t) = \sigma e^{-i\omega_0 t}, \qquad \sigma^\dagger(t) = \sigma^\dagger e^{i\omega_0 t}, \tag{2.1.6}$$

so that

$$\mathbf{d}^{(+)}(t) \sim e^{-i\omega_0 t}, \qquad \mathbf{d}^{(-)}(t) \sim e^{i\omega_0 t}. \tag{2.1.7}$$

The component $\mathbf{d}^{(+)}$ is therefore associated with a positive frequency (since it oscillates as $e^{-i\omega_0 t}$), while $\mathbf{d}^{(-)}$ represents its complex conjugate part.

Including the same decomposition for the classical electric field,

$$\mathbf{E}(t) = \mathbf{E}^{(+)}(t) + \mathbf{E}^{(-)}(t) \tag{2.1.8}$$

The atom–field interaction Hamiltonian becomes

$$\begin{aligned} H_{\mathrm{AF}} &= -(\mathbf{d}^{(+)} + \mathbf{d}^{(-)}) \cdot (\mathbf{E}^{(+)} + \mathbf{E}^{(-)}) \\ &= -\mathbf{d}^{(+)} \cdot \mathbf{E}^{(+)} - \mathbf{d}^{(+)} \cdot \mathbf{E}^{(-)} - \mathbf{d}^{(-)} \cdot \mathbf{E}^{(+)} - \mathbf{d}^{(-)} \cdot \mathbf{E}^{(-)}. \end{aligned} \tag{2.1.9}$$

Using the time dependences $\mathbf{d}^{(\pm)} \sim e^{\mp i\omega_0 t}$ and $\mathbf{E}^{(\pm)} \sim e^{\mp i\omega_{\mathrm{L}} t}$, we find that the four resulting terms oscillate at different frequencies:

- $\mathbf{d}^{(+)} \cdot \mathbf{E}^{(+)}$ and $\mathbf{d}^{(-)} \cdot \mathbf{E}^{(-)}$ oscillate at the sum frequency $(\omega_{\mathrm{L}} + \omega_0)$ and are rapidly varying.
- $\mathbf{d}^{(+)} \cdot \mathbf{E}^{(-)}$ and $\mathbf{d}^{(-)} \cdot \mathbf{E}^{(+)}$ oscillate near the difference frequency $|\omega_{\mathrm{L}} - \omega_0|$ and are slowly varying near resonance.

Under the rotating-wave approximation (RWA), the fast-oscillating terms at $\omega_0 + \omega_{\mathrm{L}}$ average out and can be neglected, leaving only the near-resonant interaction terms. The interaction Hamiltonian then simplifies to

$$H_{\mathrm{AF}} \simeq -\mathbf{d}^{(+)} \cdot \mathbf{E}^{(-)} - \mathbf{d}^{(-)} \cdot \mathbf{E}^{(+)}. \tag{2.1.10}$$

This form describes the resonant exchange of energy between the atom and the field, and leads directly to the familiar Rabi oscillations.

Using the time dependence of the field and dipole operators, we obtain

$$H_{\mathrm{AF}} = \frac{\hbar\Omega}{2}\left(\sigma e^{i\omega_{\mathrm{L}} t} + \sigma^{\dagger} e^{-i\omega_{\mathrm{L}} t}\right), \tag{2.1.11}$$

where Ω is the Rabi frequency defined as

$$\Omega = -\frac{\langle g|\mathbf{d}\cdot\hat{\varepsilon}|e\rangle E_0}{\hbar}. \tag{2.1.12}$$

The Rabi frequency quantifies the strength of the coupling between the atom and the field.

In the rotating frame, the atomic and interaction Hamiltonians take simple forms that generate the same equations of motion as in the laboratory frame. The effective rotating-frame atomic Hamiltonian is given by

$$\tilde{H}_A = -\hbar\Delta\,|e\rangle\,\langle e|\,, \tag{2.1.13}$$

where $\Delta = \omega_\mathrm{L} - \omega_0$ is the detuning of the laser frequency from the atomic resonance.

The corresponding rotating-frame interaction Hamiltonian is

$$\tilde{H}_\mathrm{AF} = -\,\mathbf{d}^{(+)}\cdot\tilde{\mathbf{E}}^{(-)} - \mathbf{d}^{(-)}\cdot\tilde{\mathbf{E}}^{(+)} = \frac{\hbar\Omega}{2}\left(\sigma + \sigma^\dagger\right), \tag{2.1.14}$$

where Ω is the Rabi frequency defined in Eq. (2.1.12). These Hamiltonians describe the atomic dynamics in a frame rotating at the laser frequency, where the rapidly oscillating terms have been removed.

2.1.2 Dressed states

The bare atomic states $|g\rangle$ and $|e\rangle$ are no longer stationary when the atom interacts with the light field. To find the new eigenstates of the coupled atom–field system, we write the equations of motion for the probability amplitudes c_e and c_g in the rotating frame as

$$\partial_t \begin{bmatrix} c_e \\ c_g \end{bmatrix} = -i \begin{bmatrix} -\Delta & \Omega/2 \\ \Omega^*/2 & 0 \end{bmatrix} \begin{bmatrix} c_e \\ c_g \end{bmatrix} = -\frac{i}{\hbar}\,\tilde{H} \begin{bmatrix} c_e \\ c_g \end{bmatrix}, \tag{2.1.15}$$

where the effective rotating-frame Hamiltonian is

$$\tilde{H} = \hbar \begin{bmatrix} -\Delta & \Omega/2 \\ \Omega^*/2 & 0 \end{bmatrix}. \tag{2.1.16}$$

Diagonalization of this Hamiltonian yields the dressed-state energies

$$E_{\pm} = -\frac{\hbar\Delta}{2} \pm \frac{\hbar\Omega_R}{2}, \qquad \text{where} \quad \Omega_R = \sqrt{\Omega^2 + \Delta^2} \tag{2.1.17}$$

is the generalized Rabi frequency. The corresponding eigenstates, known as the dressed states, are linear combinations of the uncoupled states $|g\rangle$ and $|e\rangle$,

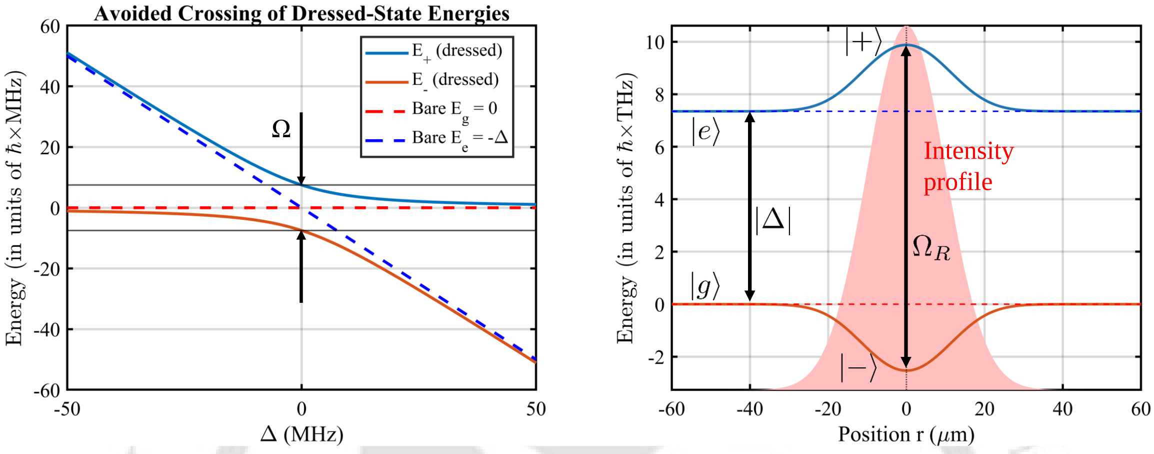

(a) (b)

Figure 2.1: (a) Dressed-state energies showing the avoided crossing with splitting determined by the Rabi frequency $\Omega = 15$ MHz. (b) Spatial variation of dressed-state energies due to the position-dependent Rabi frequency $\Omega_{\mathrm{R}}(r)$, assuming a Gaussian beam profile with a beam radius of 20 μm.

$$\begin{aligned} |+\rangle &= \sin\theta\ |g\rangle + \cos\theta\ |e\rangle\,, \\ |-\rangle &= \cos\theta\ |g\rangle - \sin\theta\ |e\rangle\,, \end{aligned} \tag{2.1.18}$$

where the mixing (or Stückelberg) angle θ is defined by

$$\tan(2\theta) = -\frac{\Omega}{\Delta}, \qquad (0 \le \theta < \pi/2). \tag{2.1.19}$$

By convention, the state $|+\rangle$ corresponds to the higher-energy dressed state. The coupling to the light field thus mixes the bare states and produces an avoided crossing in the energy spectrum at $\Delta = 0$, where the bare-state energies 0 and $-\hbar\Delta$ become degenerate as shown in Fig. 2.1(a).

2.2 Dipole force and optical dipole potential

The dipole potential can be qualitatively understood using the dressed-atom picture. In the presence of atom-field coupling, the energies of the dressed states shift by an amount proportional to the local electric-field amplitude. For large detuning, where $|\Delta| \gg \Omega$, the dressed states reduce almost entirely to the bare atomic states, and their energy shifts follow the spatial intensity profile of the laser beam.

For red detuning ($\Delta < 0$), the lower dressed state $|-\rangle$ shifts downward in energy. Since the shift is largest at the point of maximum intensity, the atom experiences an attractive optical dipole potential, as illustrated in Fig. 2.1(b). In this regime, the ground state is well approximated by the lower dressed state, and the light shift directly gives the trap potential.

The potential can be obtained from the dressed-state energies,

$$E_{\pm} = -\frac{\hbar\Delta}{2} \pm \frac{\hbar}{2}\sqrt{\Delta^2 + \Omega^2}, \tag{2.2.1}$$

and in the far-detuned limit $|\Delta| \gg \Omega$, the lower dressed state yields

$$U_{\mathrm{dip}}(r) \approx -\frac{\hbar\,\Omega^2(r)}{4\Delta}. \tag{2.2.2}$$

For red detuning ($\Delta < 0$), this potential is negative, producing an attractive trap whose depth follows the spatial variation of the laser intensity. Up to this point, the atom–light interaction has been treated as a closed Hermitian system using the dressed-state picture. In practice, however, the excited atomic state is coupled to the vacuum electromagnetic modes, leading to spontaneous emission and dissipation. These effects are incorporated using the density-matrix or optical Bloch equation formalism, where the finite excited-state lifetime is characterized by the spontaneous decay rate Γ [60–62]. The resulting dissipative dynamics give rise to photon scattering and heating in optical dipole traps. The same atom–field interaction also produces a small scattering rate due to the imaginary part of the atomic response. In the far-detuned and low-saturation limit, the spontaneous scattering rate is [65]

$$\Gamma_{\mathrm{sc}}(r) = \frac{3\pi c^2\Gamma^2}{2\hbar\omega_0^3}\frac{I(r)}{\Delta^2}, \tag{2.2.3}$$

where $I(r)$ is the local intensity, Γ is the natural linewidth, and ω_0 is the transition frequency. This expression shows that the scattering rate scales as $1/\Delta^2$, in contrast to the

$1/\Delta$ scaling of the dipole potential in Eq. 2.2.2. As a result, increasing the detuning reduces heating from scattering much faster than it reduces the trap depth. Large detuning is therefore preferred in optical dipole traps.

The conservative force associated with the dipole potential follows from the spatial gradient of $U_{\text{dip}}(r)$,

$$\mathbf{F}_{\text{dip}}(r) = -\nabla U_{\text{dip}}(r). \tag{2.2.4}$$

Because $\Omega(r)$ is proportional to the local electric-field amplitude, and hence to the square root of the intensity, the dipole force is strongest where the intensity gradients are largest. In a tightly focused beam, the intensity increases rapidly toward the focal region, giving rise to a strong restoring force for red-detuned light.

For a Gaussian laser beam with waist w_0 and power P, the intensity distribution is [66]

$$I(r,z) = \frac{2P}{\pi w^2(z)} \exp\left(-\frac{2r^2}{w^2(z)}\right), \tag{2.2.5}$$

with

$$w(z) = w_0\sqrt{1 + \left(\frac{z}{z_{\text{R}}}\right)^2}, \qquad z_{\text{R}} = \frac{\pi w_0^2}{\lambda}. \tag{2.2.6}$$

Since the Rabi frequency satisfies $\Omega(r,z) \propto \sqrt{I(r,z)}$, the dipole potential inherits the same Gaussian profile. The three-dimensional trapping potential is

$$U(r,z) = U_0 \frac{w_0^2}{w^2(z)} \exp\left(-\frac{2r^2}{w^2(z)}\right), \tag{2.2.7}$$

where the trap depth is

$$U_0 = -\frac{\hbar\Omega_0^2}{4\Delta}. \tag{2.2.8}$$

The detuning Δ in this expression corresponds to a two-level atom. For a real multilevel atom such as ^{87}Rb, the effective detuning must include all dipole-allowed transitions. The effective detuning is [65]

$$\frac{1}{\Delta_{\text{eff}}} = \frac{1}{3}\left(\frac{2}{\Delta_{\text{D2}}} + \frac{1}{\Delta_{\text{D1}}}\right), \tag{2.2.9}$$

which accounts for the different oscillator strengths of the D_1 and D_2 lines. The factor of 2 associated with the D2 transition arises from the larger oscillator strength of the $5S_{1/2} \to 5P_{3/2}$ transition compared to the D1 line due to angular-momentum degeneracy and dipole coupling coefficients. Here, the D_1 line corresponds to the $5S_{1/2} \to 5P_{1/2}$

transition at 795 nm and the D$_2$ line corresponds to the $5S_{1/2} \rightarrow 5P_{3/2}$ transition at 780 nm.

2.3 Light shift for a multi-level atom

The approach described in Sec. 2.2 is sufficient to qualitatively understand the origin of optical dipole traps using a simple two-level atom. However, this model is not adequate for describing the interaction between a multilevel atom and an off-resonant trapping field. In real atoms, the light shift receives contributions from all dipole-allowed transitions, including those arising from fine-structure and hyperfine-structure levels. Therefore, a complete description of the dipole potential requires summing the contributions from all relevant excited states [67, 68]. The light shift for the state $|\alpha, F, m_F\rangle$ can be derived from the second-order theory as [69]

$$\Delta E_{(\alpha,F,m_F)} = \langle \alpha, F, m_F | H_{\mathrm{AF}} | \alpha, F, m_F \rangle + \sum_{\alpha,F,m'_F} \frac{\left|\langle \alpha, F, m_F | H_{\mathrm{AF}} | \alpha, F, m'_F \rangle\right|^2}{E_{(\alpha,F,m_F)} - E_{(\alpha,F,m'_F)}}. \quad (2.3.1)$$

where α denotes additional quantum numbers that specify the electronic state (such as configuration, term, and parity), F is the total angular momentum, and m_F its magnetic sublevel. The first-order energy correction is zero since the dipole interaction operator does not have diagonal matrix elements in the atomic eigenbasis; the expectation value $\langle \alpha | \mathbf{d} \cdot \mathbf{E} | \alpha \rangle$ vanishes due to parity selection rules. Therefore, the AC Stark shift originates solely from the second-order term of perturbation theory.

Let us consider an atom trapped in a tightly focused laser. The corresponding light shift due to the trapping laser can be calculated as follows. The AC Stark shift of the state $|\alpha, F, m_F\rangle$ in the presence of trapping light is given by [68],

$$\begin{aligned} \Delta E_{(\alpha,F,m_F)} = -&\frac{I}{2\epsilon_0 c\hbar} \\ &\sum_{\alpha',F',m'_F} \delta^{\alpha F m_F}_{\alpha' F' m'_F} \left|\langle \alpha, F, m_F \mid e\mathbf{r} \mid \alpha', F', m'_F \rangle\right|^2, \end{aligned} \quad (2.3.2)$$

where

$$\delta^{\alpha F m_F}_{\alpha' F' m'_F} = \frac{1}{\omega^{\alpha F m_F}_{\alpha' F' m'_F} + \omega} + \frac{1}{\omega^{\alpha F m_F}_{\alpha' F' m'_F} - \omega}, \quad (2.3.3)$$

is the detuning factor, which satisfies $\delta^{\alpha F m_F}_{\alpha' F' m'_F} = -\delta^{\alpha' F' m'_F}_{\alpha F m_F}$. Here, I is the trapping beam intensity, ϵ_0 the vacuum permittivity, c the speed of light in vacuum, and $\hbar$ the reduced Planck constant. The operator $e\mathbf{r}$ represents the electric dipole operator, and $\langle \alpha, F, m_F \mid e\mathbf{r} \mid \alpha', F', m'_F \rangle$ is the corresponding electric-dipole matrix element. The quantity $\omega^{\alpha F m_F}_{\alpha' F' m'_F}$ is the difference between the unperturbed angular frequency of the transition $|\alpha, F, m_F\rangle \rightarrow |\alpha', F', m'_F\rangle$, and ω is the angular frequency of the trapping light.

In multilevel atoms, the strength of an optical transition depends on the dipole matrix element between the hyperfine states. The matrix element between the hyperfine states $|\alpha, F, m_F\rangle$ and $|\alpha', F', m_{F'}\rangle$ is written in terms of the reduced matrix element and angular momentum coupling coefficients as [68],

$$|\langle F, m_F | e\, r_q | F', m_{F'} \rangle|^2 = |\langle J || e\mathbf{r} || J' \rangle|^2 \, (2F+1)(2F'+1) \begin{pmatrix} F & 1 & F' \\ -m_F & q & m_{F'} \end{pmatrix}^2 \times \begin{Bmatrix} J & J' & 1 \\ F' & F & I \end{Bmatrix}^2 , \tag{2.3.4}$$

Here, the parameter q takes the values 0,±1 for the trap polarization of π, σ^+, and σ^-, respectively. The reduced matrix element satisfies the symmetry

$$\big|\langle J || er || J' \rangle\big| = \big|\langle J' || er || J \rangle\big|,$$

so that upward and downward electric-dipole transitions have identical strength. The normalization convention of the reduced dipole matrix element used here provides a consistent and unambiguous definition of the transition strength. This choice removes the ambiguity that arises from the relative ordering of the energy levels (whether a state lies higher or lower in energy), which is particularly important when evaluating transition strengths in multilevel atoms [70, 71]. This property ensures that the AC Stark shifts of two isolated states automatically satisfy the expected two-level relation $\Delta E^{\alpha F m_F}_{\alpha' F' m'_F} = -\Delta E^{\alpha' F' m'_F}_{\alpha F m_F}$ without requiring additional degeneracy factors. In contrast, the older spectroscopic normalization used in some earlier works [67] introduces factors such as $(2J+1)$ into the matrix elements. These extra terms break the simple symmetry above and require one to keep track of which level lies higher in energy, which can lead to inconsistencies and errors. Adopting the former convention, therefore, eliminates these ambiguities and provides a unified framework for calculating dipole matrix elements, Stark shifts, and transition strengths in real atomic systems.

2.4 Single atom loading

The atom loading dynamics in the dipole trap can be described by [72, 73],

$$\frac{dN}{dt} = R_{\text{load}} - \gamma_{\text{coll}} N - \beta' N(N-1), \tag{2.4.1}$$

where R_{load} is the loading rate determined by the MOT density and overlap with the dipole trap. The coefficient γ_{coll} represents one-body loss due to collisions with background-gas atoms. The coefficient β' accounts for two-body loss processes, such as light-assisted collisions between trapped atoms. The term $N(N-1)$ reflects the fact that two-body loss requires a pair of atoms in the trap. In the steady state ($\frac{dN}{dt} \approx 0$) there are two loading regimes characterized by loading rate (R_{load}) (i) weak loading regime when R_{load} is small (small flux MOT), (ii) strong loading regime when R_{load} is high (high flux MOT). In the weak loading regime, the collisions between trapped atoms are rare because the rate at which atoms enter the trap is low; therefore two-body loss term is negligible, which leads to $\langle N \rangle \approx R_{\text{load}}/\gamma_{\text{coll}}$. In the strong loading regime, many atoms enter the ODT, so the two-body loss is not negligible. The two-body collisions dominate the loss which leads to $\langle N \rangle \approx \sqrt{R_{\text{load}}/\beta'}$. The transition between the two regimes is defined as a collisional blockade regime. This regime is characterized by the critical atom number $N_c \approx R_{\text{load}}/\beta'$ with critical loading rate $R_c \approx \gamma_{\text{coll}}^2/\beta'$. In this regime, the trap ends up with either zero or one atom. If two atoms arrive in the ODT at the same time, a light-assisted collision ejects both atoms, and the trap becomes empty. If a single atom arrives, it remains trapped because no collisions occur, and the trap holds one atom. However, the trapping volume is also another parameter that decides the collisional blockade regime.

To illustrate the collisional blockade effect, we performed a Gillespie Monte-Carlo simulation of atom loading in a microscopic dipole trap as described in [73]. Three different trap beam waists were considered: (i) $\omega_0 = 0.7\ \mu$m, (ii) $\omega_0 = 1.4\ \mu$m, and (iii) $\omega_0 = 4\ \mu$m to show how the trapping volume influences the onset of blockade behavior. The simulation parameters were chosen following Ref. [73]: a one-body loss rate of $\gamma_{\text{coll}} = 0.2$ s^{-1}, corresponding to a background pressure of $\sim 10^{-9}$ mbar, and a two-body loss coefficient of $\beta' = 1000$ s^{-1} for the tightest trap ($\omega_0 = 0.7\ \mu$m). Since β' is inversely proportional to the trap volume, which scales as ω_0^4 for a Gaussian beam [73], its value decreases rapidly for

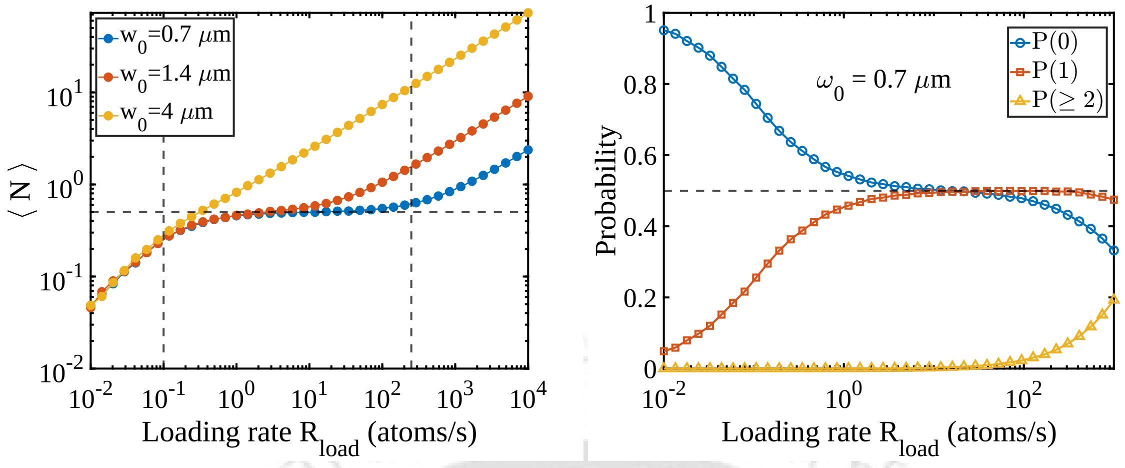

(a) (b)

Figure 2.2: (a) Mean atom number $\langle N \rangle$ versus loading rate R_{load} for three trap beam waists w_0. Dashed lines mark the transition regimes defined by $\gamma_{\text{coll}}/2$, $\beta'/4$, and the single-atom loading threshold $\langle N \rangle = 0.5$. (b) Loading probabilities $P(0)$, $P(1)$, and $P(\geq 2)$ as a function of the loading rate R_{load} for a trap waist of $w_0 = 0.7$ μm.

larger waists. The scaled values of β' were used for the other trap sizes in the simulation. The simulated results are shown in Fig. 2.2.

In Fig. 2.2(a), the blockade region appears around the loading rates $\gamma_{\text{coll}}/2$ in the weak-loading regime and $\beta'/4$ in the strong-loading regime, where the average atom number in the trap $\langle N \rangle$ reaches about 0.5. This region becomes narrower when the trap waist increases because the two-body collision rate decreases with larger trap volumes.

In the blockade regime, the total probability of loading either zero or one atom is close to 50%, as shown in Fig. 2.2(b). This value is a direct consequence of light-assisted collisions. When two atoms enter the ODT together, the cooling light excites them to a molecular state at the Condon point R_c, where the distance between the two atoms is such that the laser becomes resonant with the molecular excitation. This process is shown in Fig. 2.3. Under red-detuned conditions, this excited molecular state is attractive. The two atoms accelerate toward each other and gain a large amount of kinetic energy. This energy is much larger than the trap depth, and both atoms are lost in a single collision event. As a result, the trap remains empty until the next loading attempt. When the next atom arrives alone, it stays in the trap because no further collisions occur. This mechanism limits the trap to either zero or one atom. Using blue-detuned light-assisted collisions, it is possible to have almost a single atom in the trap after the collision event [74, 75]. In

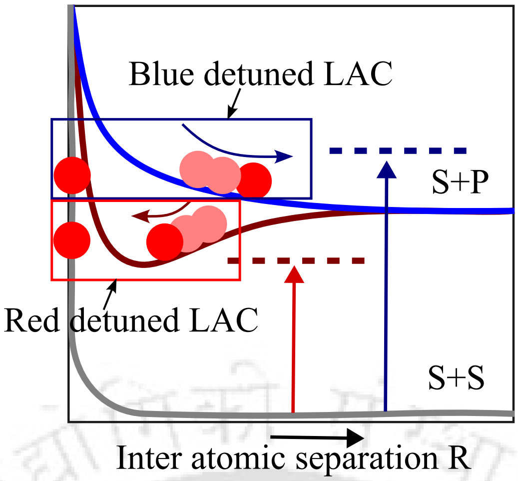

Figure 2.3: Schematic illustration of light-assisted collisions (LAC) showing red and blue-detuned molecular potentials that lead to single-atom survival or pair loss depending on the detuning.

the blue-detuned case, the excited molecular potential is repulsive instead of attractive. When two atoms are excited at R_c, they are pushed apart rather than pulled together. The kinetic energy they gain is limited by the detuning and is much smaller than the radiative-escape energy produced under red detuning. Because the energy gain is smaller, one of the atoms is more likely to remain trapped after the collision. This increases the probability of ending up with a single atom instead of losing both atoms. For this reason, blue-detuned light-assisted collisions lead to a higher single-atom loading efficiency.

Thus, the mechanism of the blockade regime is determined by the type of molecular excitation. Red-detuned excitation produces strong pair loss and limits the average atom number to 0.5, while blue-detuned excitation reduces pair loss and increases the probability of loading a single atom in the trap.

2.5 Rydberg atoms

Trapped single atoms offer many advantages because we can control their internal states with high precision. However, ground-state atoms interact very weakly at micrometer distances, and this makes it difficult to create entanglement between neighboring atoms. Entanglement requires strong and controllable interactions, which are essential for performing quantum logic operations. This limitation is overcome by exciting the atom to a Rydberg state ($n \gg 1$). A Rydberg atom has a highly excited electron and a very large electric dipole moment between adjacent Rydberg states, which produces strong interactions with nearby atoms [32]. These interactions can be several orders of magnitude stronger than those between ground-state atoms. As a result, Rydberg excitation becomes the key mechanism for implementing two-qubit gates in neutral-atom platforms. The central effect is the Rydberg blockade, where the excitation of one atom shifts the energy of a neighboring atom and prevents it from being excited [76, 77]. This blockade effect enables deterministic entanglement and forms the foundation of Rydberg-based quantum computing and quantum simulation.

2.5.1 Rydberg-Rydberg interaction

The main advantages of Rydberg interactions are flexibility, controllability, and tunability. The interaction strength can be adjusted by choosing appropriate Rydberg states or by using external optical fields. This enables fast control of the interaction strength on nanosecond to microsecond timescales. Several atomic properties that determine the interaction strength scale strongly with the principal quantum number n. In particular, the electric dipole matrix elements between nearby Rydberg states scale approximately as n^2. The size of the Rydberg electron orbital scales as n^2 (in atomic units), and the static polarizability scales roughly as n^7. These strong scaling laws explain why Rydberg atoms exhibit very large and tunable interactions [32, 78, 79]. In the following, we briefly discuss the dominant interaction types and their distance dependence.

A Rydberg atom can be viewed as an electric dipole formed by the positively charged ionic core and the highly excited electron. The dipole moment is

$$\boldsymbol{d} = -e\,\mathbf{r},$$

where $\mathbf{r}$ is the average distance between the electron and the ionic core. Since this distance scales as $\mathrm{r} \propto n^2$, the dipole moment of a Rydberg atom also scales as $d \propto n^2$.

The interaction between two electric dipoles separated by a distance R is given by [79]

$$V_{\mathrm{dd}} = \frac{1}{4\pi\varepsilon_0}\left[\frac{\boldsymbol{d}_1 \cdot \boldsymbol{d}_2}{R^3} - 3\frac{(\boldsymbol{d}_1 \cdot \mathbf{R})(\boldsymbol{d}_2 \cdot \mathbf{R})}{R^5}\right].$$

In the resonant dipole–dipole case, the energy spacing between two Rydberg pair states becomes nearly degenerate, and excitation can be exchanged between the atoms. This process is known as a Förster resonance. The interaction strength is

$$V_{\mathrm{dd}} \sim \frac{C_3}{R^3},$$

where the coefficient C_3 scales as $C_3 \propto n^4$.

In the off-resonant case, the pair of atoms occupies the same Rydberg state (for example, $ns + ns$). The interaction proceeds through virtual intermediate states and leads to a second-order energy shift known as the van der Waals [80],

$$V_{\mathrm{vdW}} = \frac{C_6}{R^6}.$$

The coefficient is approximately

$$C_6 \sim \frac{C_3^2}{\Delta E},$$

where ΔE is the detuning between the bare pair states. Since $C_3 \propto n^4$ and $\Delta E \propto n^{-3}$, the overall scaling becomes

$$V_{\mathrm{vdW}} \propto \frac{n^{11}}{R^6}.$$

The value of ΔE can be tuned by external static fields, which enables control of the interaction strength.

2.5.2 Rydberg blockade

The simultaneous excitation of two atoms to Rydberg states is suppressed when the atoms are separated by only a few micrometers. This effect is known as the Rydberg blockade. Consider two atoms with ground and Rydberg states $|g\rangle$ and $|r\rangle$. Initially, the atoms are in the ground state $|gg\rangle$. If they are far apart, they do not interact, and the laser can excite both atoms to the doubly excited state $|rr\rangle$. When the atoms are close to each other, and one atom is excited to $|r\rangle$, the strong Rydberg-Rydberg interaction shifts the energy of the $|rr\rangle$ state by an amount ΔE. This spatial region defines the blockade radius R_b. When ΔE is larger than the excitation linewidth, the $|rr\rangle$ state becomes off-resonant with the laser. As a result, simultaneous excitation to $|rr\rangle$ is blocked, and the system remains in the singly excited manifold. This is the Rydberg blockade [76, 77]. In this regime, the second atom becomes off-resonant with the excitation laser and cannot be excited to the Rydberg state. Inside this radius, only one Rydberg excitation is allowed. The blockade radius is typically a few micrometers, often less than 10 μm, depending on

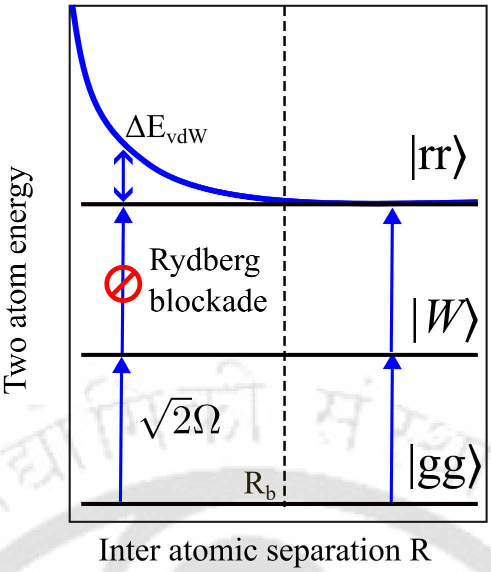

Figure 2.4: Rydberg blockade mechanism: At short interatomic separation $R < R_b$, the strong van der Waals interaction shifts the doubly excited state $|rr\rangle$ by ΔE_{vdW}, preventing simultaneous excitation of both atoms. The system instead couples to the collective singly excited state $|W\rangle$ with enhanced Rabi frequency $\sqrt{2}\Omega$.

the Rydberg state. When the atomic separation is much larger than R_b, the interaction is weak and simultaneous excitation of both atoms becomes possible again. The Rydberg blockade not only suppresses the double excitation of two nearby atoms but also allows controlled interactions that are useful for quantum gates. This conditional excitation creates a strong dependence of one atom's state on the state of the other. As a result, the two atoms evolve into a collective state such as the symmetric singly excited state $|W\rangle = (|gr\rangle + |rg\rangle)/\sqrt{2}$, which is an entangled state [76, 81]. Such entangled states cannot be written as independent product states of the two atoms, meaning that the quantum state of one atom is correlated with the state of the other. These non-classical correlations are essential for quantum information processing, quantum simulation, and the implementation of two-qubit quantum gates.

This conditional dynamics can be used to implement two-qubit gates [34, 45, 46, 82]. For example, in a controlled-phase (CZ) gate, the control atom is excited to the Rydberg state only when it is in the logical state $|1\rangle$. The blockade then shifts the energy of the target atom and prevents its excitation, producing the required conditional phase. In this way, the presence or absence of a Rydberg excitation on one atom determines the evolution of the other atom. This mechanism forms the basis of fast and high-fidelity two-qubit gates in neutral-atom quantum computers.

3

Experimental Details of the Yb Setup

Contents

In this chapter, we present the details of the experimental setup developed for working with Yb atoms. The main components of the setup include the vacuum system, Zeeman slower, and the laser systems used for cooling and trapping the atoms. The experiment primarily uses the strong ${}^1S_0 \rightarrow {}^1P_1$ singlet transition at 399 nm and the narrow ${}^1S_0 \rightarrow {}^3P_1$ intercombination transition at 556 nm for laser cooling and trapping. The relevant energy-level structure and optical transitions are shown in Fig. 3.1.

3.1 Design and construction of the vacuum system

In this section, we present the vacuum system used for cooling and trapping of Yb atoms. The overall layout of the ultra-high vacuum (UHV) system is illustrated in Fig. 3.2, which presents both the computer-aided design (CAD) model and a two-dimensional (2D) schematic view of the setup. The vacuum system is divided into various sections: The oven section, the Zeeman slower, and the MOT (magneto-optical trap) section. Many of our vacuum element designs are adapted and modified from the works [83–87].

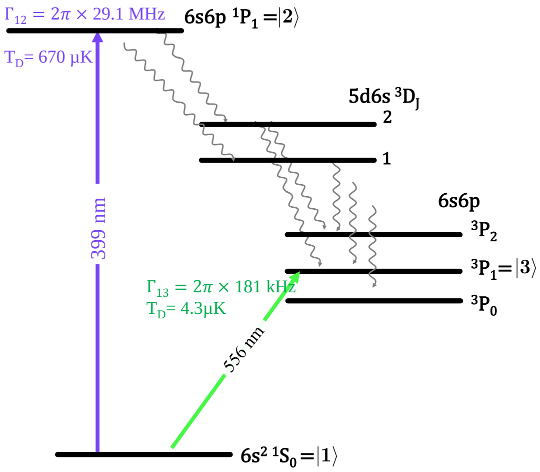

Figure 3.1: The relevant energy levels of Yb. Γ and T_D are the linewidth and the Doppler temperature of the transition. The wavy arrow shows the decay paths of the $^1P_1$ state.

3.1.1 Oven section

The oven section is designed to function at higher temperatures, up to 500 °C. Since Yb has an extremely low vapor pressure at room temperature, high oven temperatures are required to achieve a vapor pressure sufficient to produce the desired atomic flux. The sectional view of the oven assembly is shown in Fig. 3.3. It includes the Yb reservoir, the collimation section, the 2D cooling stage, and the pumping station.

The oven section starts with a Yb reservoir, which is a stainless-steel cylindrical cup attached to a bored CF40 flange with a bore diameter of 10 mm. The reservoir is loaded with 50 g of pure Yb chunks (Thermo Fisher Scientific, 7440-64-4) and is typically heated to 400 °C to generate adequate atomic flux.

Collimation section

Adjacent to the Yb reservoir is the collimation section, which begins with a nozzle made of a 10 mm thick circular disk featuring a hexagonal aperture packed with approximately 300 capillary tubes, as shown in Fig. 3.4(b) and 3.4(c). Each capillary tube (Coopers Needle Works Ltd) is made of stainless steel and has a length of 10 mm, an inner diameter of 0.190 mm, and an outer diameter of 0.305 mm. To prevent clogging of the capillaries, the nozzle is maintained at a temperature 40–50 °C higher than that of the reservoir. Both the reservoir and the nozzle are heated from outside using ceramic

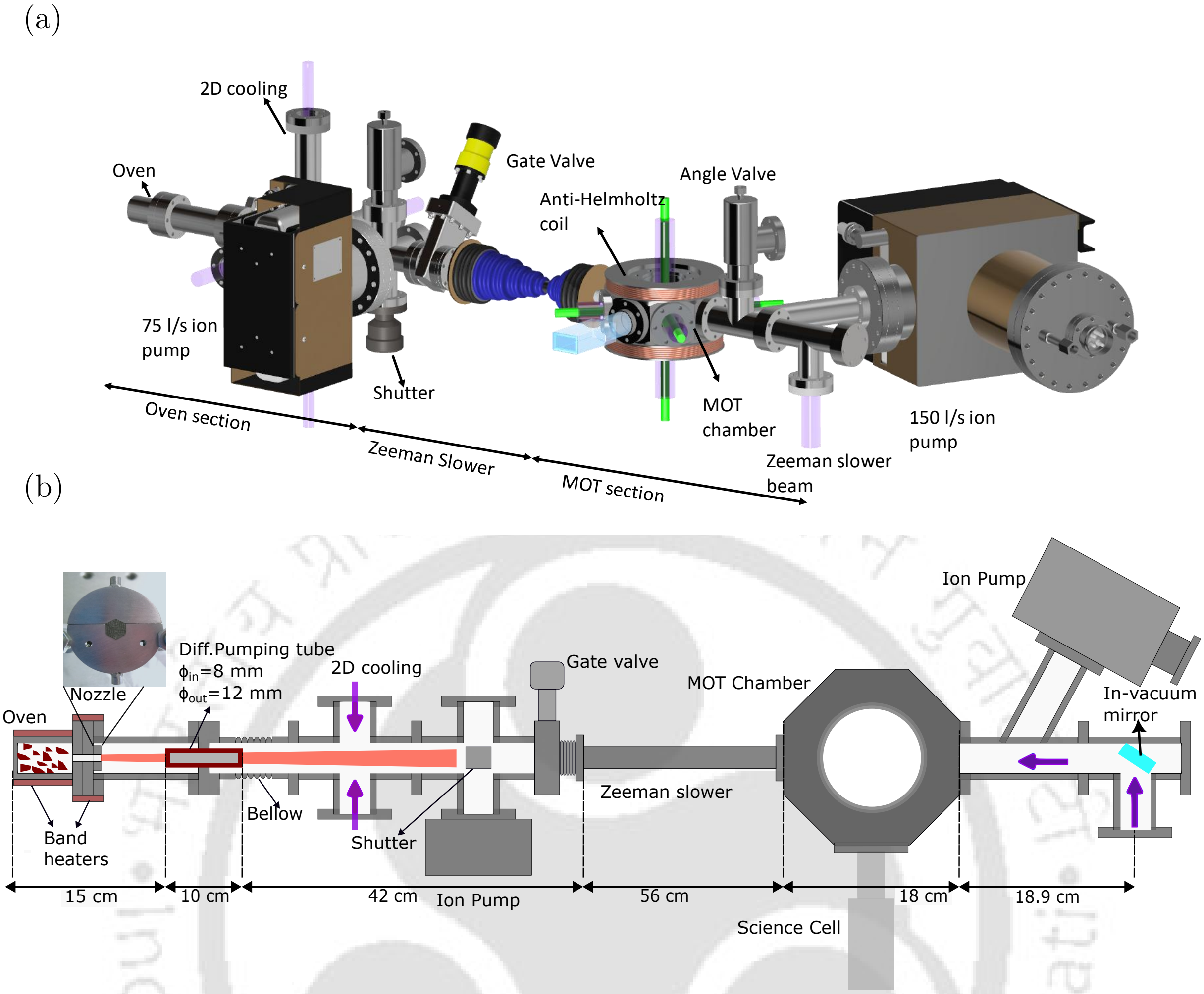

Figure 3.2: (a) CAD design of our vacuum system. It comprises various sections: oven, 2D cooling, Zeeman slower, and the MOT section. (b) 2D view of the vacuum system.

band heaters powered by variacs, as shown in Fig. 3.4(d). These ceramic band heaters are a cost-effective alternative to conventional band heaters or heating elements.

A differential pumping tube, 100 mm in length and 8 mm in inner diameter, is installed immediately after the nozzle to further collimate the atomic beam, as significant divergence was observed from the nozzle output. This tube also serves to establish a pressure differential between the oven section and the subsequent stages of the vacuum system, while simultaneously filtering out atoms with large transverse velocities. A bellow adapter with three adjustment screws connects the collimation section to the downstream part of the vacuum assembly and allows fine alignment of the atomic beam path.

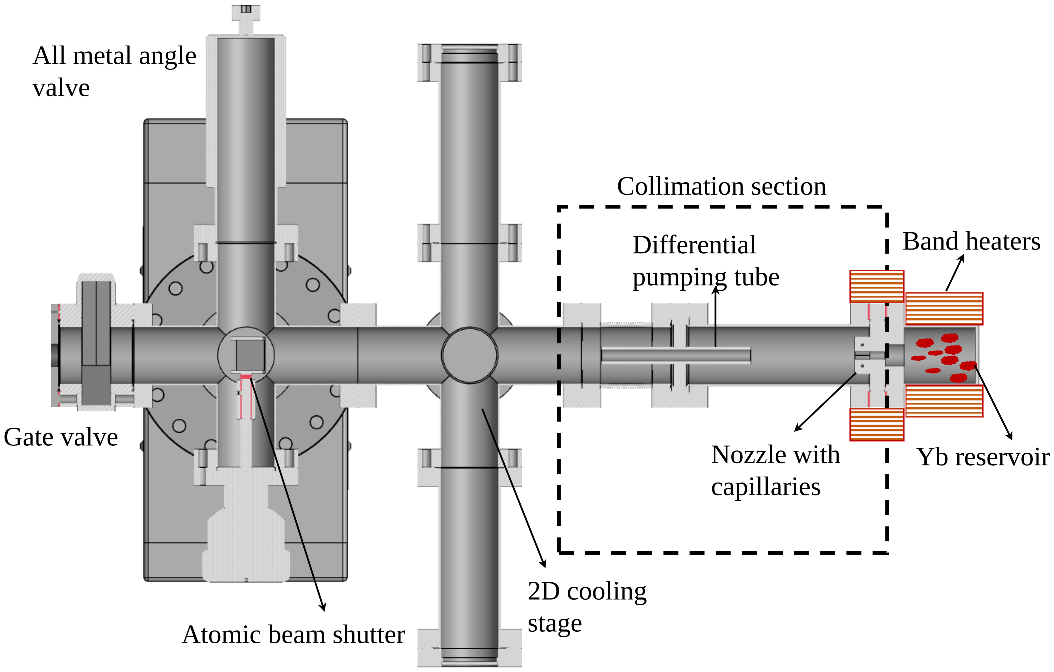

Figure 3.3: Sectional view of the oven section.

2D cooling stage

The transverse velocity components of the atomic beam emerging from the collimation section are further reduced by a transverse (2D) cooling stage. In this stage, two orthogonal pairs of counter-propagating laser beams act on the atoms to reduce their transverse motion through Doppler cooling. The purpose of this stage is to collimate the atomic beam more effectively, thereby increasing the atomic flux density in the downstream region and improving the overall loading efficiency of the MOT.

Optical access for the 2D cooling beams is provided by four Kodial glass viewports with anti-reflection (AR) coatings at 399 nm, which are attached to the four lateral arms of a six-way cross. To prevent the deposition of hot Yb atoms on the inner surfaces of the viewports, the arms of the six-way cross are extended to a length of 180 mm. This extension ensures that the viewports remain at a sufficient distance from the direct line of the atomic beam.

The combination of the differential pumping tube and the 2D cooling stage ensures that a well-collimated atomic beam propagates toward the MOT chamber, while atoms with higher transverse velocities or divergent trajectories are effectively filtered out.

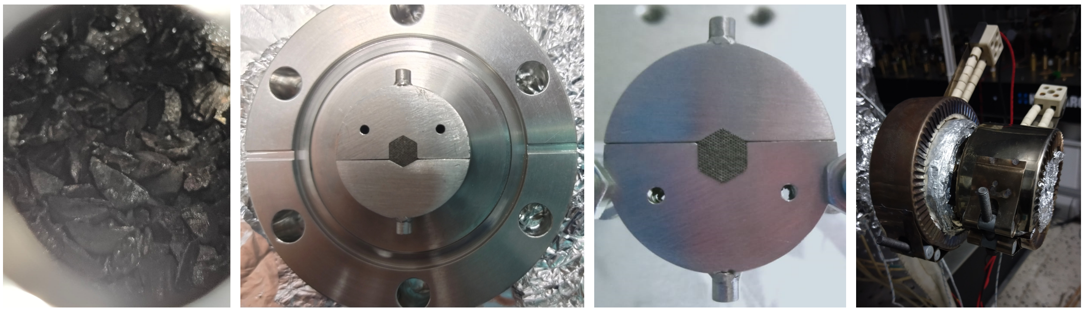

(a) (b) (c) (d)

Figure 3.4: (a) Yb metal pieces, (b) Nozzle mount on the CF40 flange, (c) Nozzle: circular disk featuring a hexagonal aperture packed with approximately 300 capillary tubes, and (d) Heating arrangement of the Yb reservoir and the nozzle with ceramic heaters.

Pumping stage and beam shutter

Next to the 2D cooling cross, a second CF40 six-way cross houses a 75 l s^{-1} ion pump (Vacion plus 75 star-cell pump, Agilent), an all-metal angle valve (MAV-150-V, MDC Vacuum limited), and a motorized rotary feed through (BRM-275-03, MDC Vacuum limited) equipped with a beam shutter. The beam shutter is used to block the atomic beam after MOT loading to prevent hot atoms from colliding with the trapped atoms. The shutter is made of a hollow stainless steel square block of slot dimensions 16 mm × 16 mm and has polished reflective surfaces, as shown in Fig. 3.5. The reason for the reflective finish is to measure the reflective efficiency of the Zeeman mirror, which reflects the slower beam into the vacuum system. An uncoated viewport is connected at a right angle to the rotary feed-through connection on the six-way cross to monitor the orientation of the beam shutter. A gate valve (E-GV-1500M-11, MDC Vacuum Limited) is attached next to it that enables us to open the oven vacuum assembly without affecting the vacuum of the MOT section. The pressure in the oven section is around 3×10^{-8} mbar during the operation of the oven at 400 °C.

3.1.2 Zeeman slower

The collimated atomic beam is slowed down by the spin-flip Zeeman slower [87, 88], which comprises a CF16 nipple of length 55 cm. The CF16 nipple helps in further collimation of the atomic beam. To generate the Zeeman slowing magnetic field profile, two types of wires are wound around a 50 cm long CF40 nipple, concentric with the CF16 slower nipple.

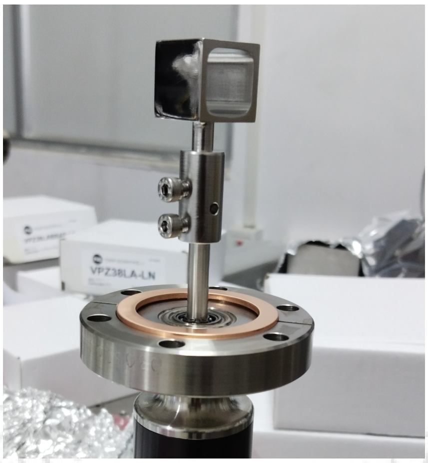

Figure 3.5: Atomic beam shutter with rotary feed through.

A high-current wire (diameter 11 mm), capable of carrying up to 130 A, is wound at both ends of the CF40 nipple. A lower-current wire (diameter 7 mm), carrying up to 30 A, is wound around the central portion of the CF40 nipple, as shown in Fig. 3.2. Due to the gap between the CF16 and CF40 nipples, heat from the current-carrying coils is dissipated without much transfer to the vacuum. The magnetic field is generated at the beginning and at the end of the slower nipple are +265 Gauss and −360 Gauss, respectively. With a −500 MHz[1] detuning of the slower laser, the Zeeman slower can slow the atom with velocities up to 350 m/s. Instead of sending the slowing laser beam through a window directly facing the Yb atomic beam, we use an in-vacuum mirror (PFE10-P01, Thorlabs) positioned at an angle of 45^o. This arrangement helps us to avoid Yb deposition on the window.

3.1.3 MOT section

The main component of this section is an octagonal chamber made of SS304 stainless steel, where the slowed atoms are trapped. The chamber features eight CF40 ports (VPZ38LABBAR-LN, Torr Scientific) on the sides and two CF63 ports (VPZ64BBAR-LN, Torr Scientific) on the top and bottom. Among the eight side ports, two are used to connect the chamber to the rest of the vacuum system, one is connected to the rectangular glass cell, and the remaining ports are fitted with Kodial glass viewports. These viewports are coated with a broadband anti-reflection (AR) coating effective in the wavelength

---

[1] Throughout this thesis, experimentally quoted detunings, linewidths, and Rabi frequencies are generally expressed in linear frequency units (Hz, MHz, GHz). Angular frequencies are used explicitly when denoted by ω.

range of 375–866 nm. A custom-designed angled CF40 four-way cross connects the MOT chamber to a 150 ls^{-1} ion pump (Vacion Plus 150 Starcell Combi Pump, Agilent) equipped with a titanium sublimator as shown in Fig. 3.2. The connection is made through one arm of the four-way cross, which is 200 mm long and oriented at an angle of 115° with respect to the atomic beam axis. This angled configuration provides additional space for mounting optics around the MOT chamber. The four-way cross also houses an all-metal angle valve that enables connection to the roughing pump during system evacuation.

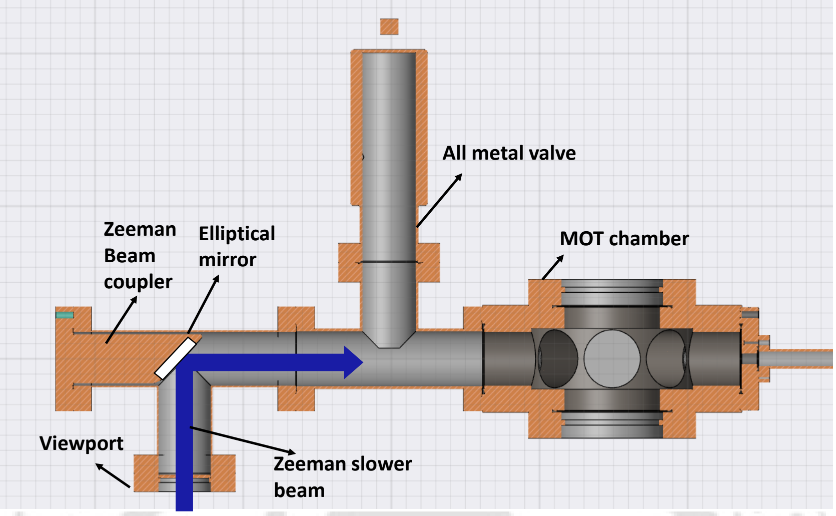

Figure 3.6: Sectional view of the MOT section.

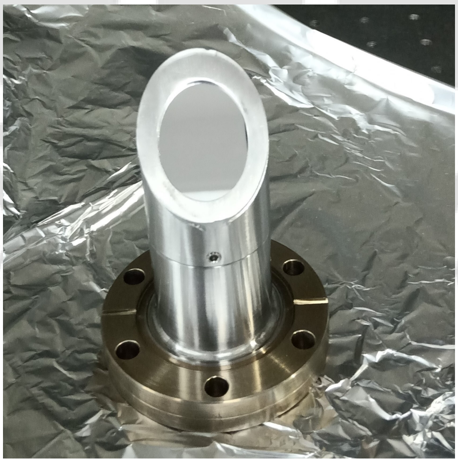

Figure 3.7: Zeeman mirror with beam coupler.

The final component of the MOT section is a CF40 tee that includes a Zeeman beam coupler and a viewport, oriented at right angles to each other as shown in Fig. 3.6. The Zeeman beam coupler is a mirror holder that contains a protected silver-coated elliptical mirror (PFE10-P01, Thorlabs). The mirror holder is fabricated from a cylindrical stainless-steel rod with a 45° angled face, welded onto a DN-CF40 blind flange, as shown in Fig. 3.7. The viewport is attached perpendicular to the beam coupler such that the beam entering through the viewport is incident on the mirror at 45°, and subsequently reflected towards the oven nozzle, as illustrated in Fig. 3.6. The 45° in-vacuum mirror is used to prevent the viewport from having a direct line of sight to the hot Yb atomic beam. This minimizes Yb deposition on the viewport surface and maintains optical transmission during long-term operation.

Science cell Our science chamber is a rectangular glass cell of dimensions 75 mm × 28 mm × 28 mm with a wall thickness of 2.5 mm, as shown in Fig. 3.2. It is connected to one of the CF40 ports of the octagon chamber perpendicular to the atomic beam. The glass cell is made of Pyrex and provides more optical access than steel chambers.

3.1.4 Cleaning and bake-out

In this section, we describe the cleaning of the vacuum components and the baking of the assembled vacuum system. Thorough cleaning of all vacuum components is essential to achieve the desired vacuum pressure. After receiving the components from the manufacturer, they were cleaned according to the following procedure. Each component was first cleaned in an ultrasonic (US) bath for 30 minutes using a 5% Simple Green detergent solution, followed by three successive US baths with demineralized water. Subsequently, the components were ultrasonically cleaned in acetone for 30 minutes and then in methanol. Finally, the cleaned parts were wiped with isopropanol using Kimwipes and covered with aluminium foil to prevent contamination. Certain vacuum components, such as ion pumps, all-metal angle valves, gate valves, and electrical feedthroughs, were pre-cleaned by the manufacturer and were ready for installation without further cleaning.

First Round of Baking and the Problems Encountered

After the careful assembly of all vacuum components, the bake-out procedure was carried out in two phases to achieve an ultra-high vacuum (UHV) environment. The objective of the first phase was to remove contaminants such as water vapor, hydrocarbons, and other adsorbed gases from the internal surfaces of the stainless-steel components. These gases, if not removed, can continuously desorb during operation and limit the base pressure achievable in the system. In the first phase, the system was baked at high temperatures ranging from 300–400 °C. Such high temperatures are necessary to desorb tightly bound impurities from the chamber walls and flanges. However, these conditions can damage delicate components like the glass cell, rotary feedthrough, gate valve, and optical viewports. To protect them, the corresponding ports were temporarily sealed using blind CF flanges during the baking.

During this phase, pumping was carried out using a turbomolecular pump backed up by a rotary pump to evacuate desorbed gases effectively. The ion pumps were intentionally kept off to prevent potential degradation of their internal elements under outgassing conditions. Heating was achieved using fiberglass heating tapes of different lengths, wrapped around the vacuum sections and powered through variacs for precise control. The temperature was monitored at multiple locations using K-type thermocouples distributed across the system to track temperature variations and avoid overheating. The vacuum system was covered with layers of aluminium foil to spread and trap the heat uniformly all over the system, as shown in Fig. 3.8.

The system temperature was gradually increased by slowly raising the variac voltage over two days until the target temperature range was reached. Once the temperature was stabilized, the system was maintained at the set temperature for approximately fifteen days to ensure thorough desorption of contaminants from all internal surfaces.

Throughout the baking process, readings were continuously monitored, and the pressure decreased steadily to the low 10^{-9} mbar range, indicating effective degassing of the system. Once the minimum pressure was achieved, we started lowering the temperature gradually. During the cooldown, when the temperature reached approximately 100 °C, a sudden pressure rise from 10^{-9} mbar to 10^{-3} mbar was observed. This abrupt increase is attributed to the development of a leak in one of the CF seals, most likely due to thermal expansion and contraction effects during cooling. A detailed leak test was performed using a residual gas analyzer (RGA) in combination with helium leak detection. By spraying helium gas over each CF joint sequentially, the leaking point was identified at the CF16–CF40 connection between the slower nipple and the gate valve. The leak was sealed by tightening the corresponding screws, after which the pressure stabilized. After this, the system temperature was gradually brought down to room temperature. Once the chamber cooled, the temporary blind flanges were replaced with the original components, including the optical viewports, gate valve, and rotary feed-through.

During the replacement process, some of the viewports were accidentally damaged while being mounted onto the side ports of the MOT chamber. The viewports were fixed using hex-head bolts and washers. While tightening, the washers came into contact with the inner edge of the viewport flanges, which led to excessive mechanical stress and caused the damage. Upon inspection, one of the five windows was found to be leaky, while the remaining four had only minor surface cracks. The defective window was replaced with a spare viewport without an anti-reflection (AR) coating, which allowed the reassembly process to continue without delay. To avoid a recurrence of window damage, socket head allen screws were used, and washers were omitted during the installation of all viewports to minimize mechanical stress on the flanges.

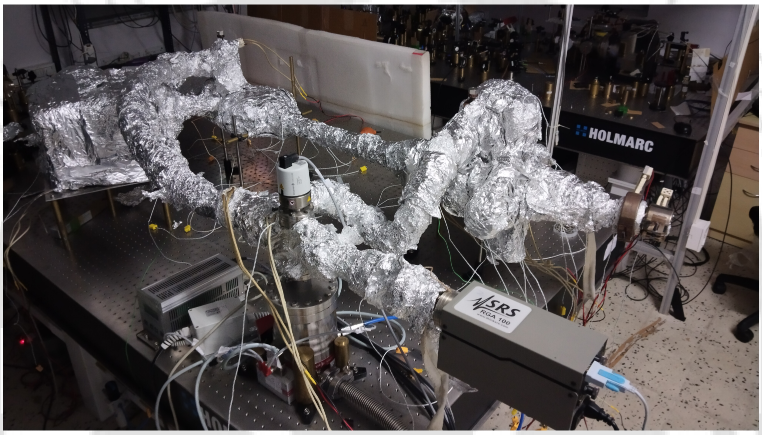

Figure 3.8: Vacuum system covered with aluminium foil for baking.

In the second phase of the bake-out, the target temperature was kept below 200 °C. Some delicate parts, such as the rotary feedthrough and gate valve, were kept below 150 °C to avoid damage. The elliptical mirror on the Zeeman beam coupler was also heated only up to 130 °C to protect its coating. This phase continued for about ten days at the target temperature.

We used only the rotary and turbo pumps to pump the vacuum system up to the final stage of baking. The ion pumps were turned on about 24 hours before the cooldown process. The temperature was then slowly brought down to room temperature over 24 hours to avoid strain on the metal seals and glass viewports. The titanium sublimation pump was fired when the temperature dropped below 100 °C to remove the remaining active gases. After cooling, the all-metal valves were closed, and the roughing pumps were disconnected from the system.

After completing the second bake-out, new issues were observed when the aluminium foils were removed. We found that Yb atoms had deposited on the viewports of the transverse

Figure 3.9: Deposition of Yb atoms on the 2D cooling stage viewports during baking. A ceramic band heater was used in an attempt to remove the coating by heating, but it was not effective.

cooling stage, as shown in Fig. 3.9. This occurred because the oven was heated to 380 °C during the bake-out, which caused Yb vapor to reach and stick to the nearby viewports, where the temperature was relatively lower.

In addition, some unknown material deposition was also found on the viewports of the MOT chamber, especially on the top and bottom windows. The deposits significantly reduced the light transmission through the glass viewports, and the transmission of the top and bottom windows decreased to approximately 50%. It may have originated either from the Yb source or from the metallic coating from the in-vacuum mirror used for sending the Zeeman slower beam. The exact cause of this deposition is still uncertain.

Second Bake-Out and Corrective Measures

After a few months, the coated viewports of both the 2D cooling section and the MOT chamber were replaced with new anti-reflection (AR) coated windows. Further, we installed a CF35 bellow of length 70 mm between the gate valve and the CF16 Zeeman nipple to reduce the mechanical strain that had caused the earlier leak. We further replaced the old Yb source (from Sigma-Aldrich) with new Yb chunks from Thermo Fisher Scientific. To prevent Yb deposition on the 2D viewports again, the 2D cooling section was kept at room temperature while the oven was maintained at a high temperature. Later, when the 2D cooling section was heated to about 150 °C, the oven temperature was lowered to 270 °C. Additionally, during the second baking process, the gate valve was kept closed to prevent any unwanted materials or vapors from entering the MOT section, as we had previously observed unknown coatings on the MOT viewports.

The final achieved pressure is about 2×10^{-9} mbar in the MOT section and 3×10^{-8} mbar in the oven section when the oven operates at its operating temperature. When the gate valve is closed, the pressure in the MOT section reaches approximately 5×10^{-11} mbar, while the pressure in the oven section remains around 2×10^{-9} mbar when the source temperature is about 350 °C. The Ti-sublimation pump is fired occasionally to bring it back to its normal level whenever we notice a rise in the MOT chamber pressure.

3.2 Spectroscopic chamber

A separate vacuum system was constructed for spectroscopy purposes. Although other options exist for performing Yb spectroscopy, such as using halogen lamps or Yb chunks in a heat-pipe setup, these methods are generally sufficient for the strong singlet blue transition. However, since the triplet green transition is much weaker, achieving a spectrum with a good signal-to-noise ratio requires a higher atomic flux. Therefore, it is preferable to have a dedicated vacuum system. The vacuum system consists of two DNCF40 six-way cubes, which are utilized for spectroscopy of green and blue transitions separately, as shown in Fig. 3.10(a). Each cube has four uncoated Kodial glass viewports attached perpendicular to the atomic beam for optical access. The oven design in this setup is nearly identical to the oven in the main vacuum setup. The oven is loaded with 25 g of high-purity Yb chunks broken into small pieces and heated to approximately 400 °C to generate a sufficient atomic flux. The atomic beam is collimated by a nozzle array of 300 capillary tubes, each 10 mm in length and 0.19 mm in inner diameter. The capillaries are stacked within the hexagonal aperture of the circular disk and clamped by two screws. The temperature of the nozzle is kept 50 ° C higher than the oven temperature. Further collimation of the atomic beam was enhanced by a differential pumping tube of length 50 mm and inner diameter of 8 mm. The collimated beam enters the spectroscopy cubes after passing through a DNCF40 six-way cross that includes connections of 75 l s^{-1} ion pump and an all-metal angle valve. This setup was baked at around 200 ° C temperature for five days. The final pressure achieved in the system is around 2×10^{-8} mbar at the oven temperature of 400 ° C.

Since a photomultiplier tube (PMT) is used for fluorescence collection, a customized optical assembly was designed to collect fluorescence from the atoms and to block stray light. The setup consists of a collection lens and a mirror arrangement, as shown in Fig. 3.10(b). The optical assembly is also designed to minimize background light reaching

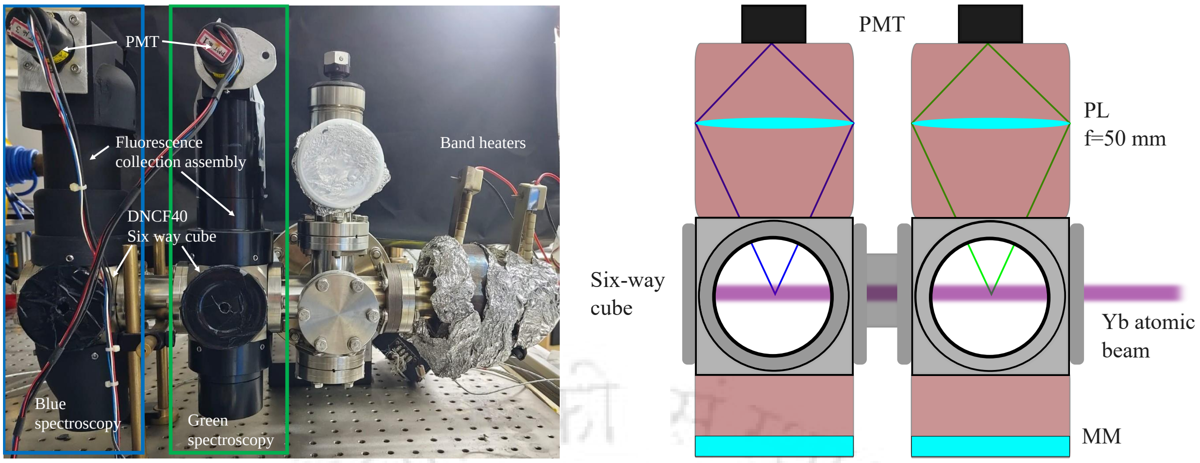

(a) (b)

Figure 3.10: (a) Vacuum system for spectroscopy. (b) Optical assembly for fluorescence collection. Abbreviations: MM – mirror; PL – plano-convex lens; PMT – photomultiplier tube.

the detector, as the PMT is highly sensitive to stray light. The optical components are mounted on adjustable holders to allow fine alignment and to maximize the collection efficiency. The first version of the holder was made of stainless steel, but it was expensive to fabricate. Therefore, a second version was made using 3D printing, which reduced the cost by nearly a factor of ten while maintaining sufficient mechanical stability for the setup.

3.3 MOT coils

The magnetic field for the MOT is generated by a pair of copper coils arranged in an anti-Helmholtz configuration. In the first design, no metal frame was used to avoid the formation of eddy currents, as shown in Fig. 3.11(a). Each coil consists of approximately 600 turns of copper wire. The two coils are separated by a distance of about 80 mm and can produce a magnetic field gradient of 7 G/cm per ampere. During operation, a current of around 5 A was used for the blue MOT. The issue with this version is that the Kapton tape was used between the layers for stability and insulation while winding the coils. During extended operation, the adhesive on the tape evaporated due to heating and deposited on the outer surface of nearby viewports. The deposits were later cleaned using isopropanol without causing any permanent coating on the viewports.

To overcome this issue, a second version of the coil was built using an aluminium frame to hold the windings, as shown in Fig. 3.11(b). The frame has an inner diameter of 118 mm, an outer diameter of 214 mm, and a thickness of 3 mm. The frame includes a 2 mm cut to prevent the formation of eddy currents. This version of coil consists of approximately 700 turns of copper wire of thickness 1.5 mm and can generate a magnetic field gradient of around 10 G/cm per ampere.

The coil winding was carried out in the IITG workshop using a lathe machine (manually) to ensure uniform and tight winding as shown in Fig. 3.11(c). After each layer was wound, the insulation quality was checked using a multi-meter by measuring the resistance between the copper wire and the aluminium frame to confirm that no short circuits or damage had occurred during the process.

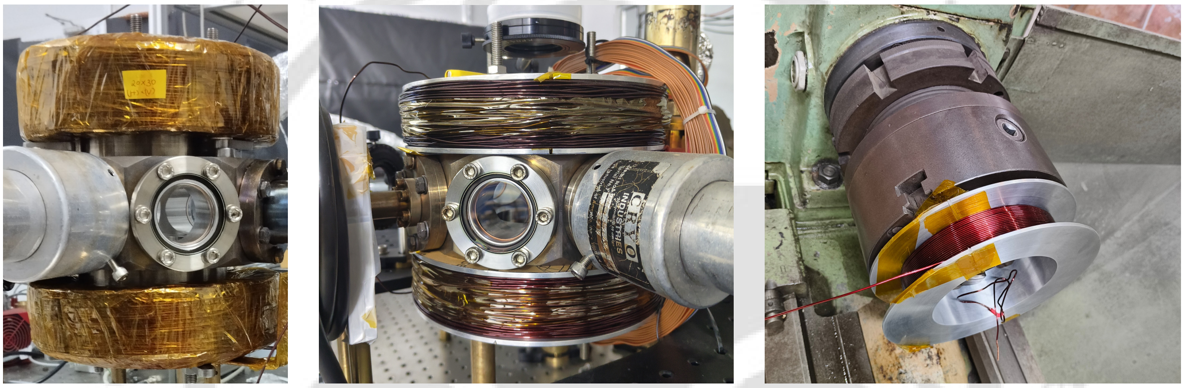
(a) (b) (c)

Figure 3.11: (a) First version of the MOT coil without frame. (b) Second version of the MOT coil with frame, (c) MOT coil wrapping process.

3.4 Zeeman slower design

In this section, we discuss the design of the Zeeman slower magnetic field coils, which are essential for the initial slowing of high-velocity atoms. The capture velocity for the MOT with beam diameter D can be estimated by [89],

$$v_c = \sqrt{\frac{\hbar k \Gamma D}{2m}} \tag{3.4.1}$$

This equation provides the upper limit of the atomic velocity that can be trapped in MOT. The capture velocity of the MOT operating on the narrow intercombination transition ^{1}S0 $\rightarrow$ ^{3}P$_1$ (green transition) is significantly lower than that of the MOT based on the broad singlet transition ^{1}S0 $\rightarrow$ ^{1}P$_1$ (blue transition). For instance, for MOT beam diameter of 20 mm, the capture velocity is approximately 102 m/s for the blue transition and about 7 m/s for the green transition. According to Maxwell-Boltzmann velocity distribution, most atoms from the oven travel with velocities up to 350 m/s at the oven temperature of 400 °C. To decelerate atoms moving faster than the MOT capture velocity, Zeeman slower can be employed. The maximum radiative force produced by laser cooling is

$$F_{\text{max}} = \frac{\hbar k \Gamma}{2}, \tag{3.4.2}$$

which gives a maximum acceleration

$$a_{\text{max}} = \frac{F_{\text{max}}}{m} = \frac{\hbar k \Gamma}{2m}, \tag{3.4.3}$$

where $k = 2\pi/\lambda$ is the wavevector, Γ is the natural linewidth of the transition, and m is the atomic mass [60]. Since the maximum acceleration scales linearly with the linewidth, the broad singlet transition ($\Gamma/2\pi \approx 29$ MHz) provides an acceleration approximately two orders of magnitude larger than the narrow triplet transition ($\Gamma/2\pi \approx 181$ kHz). Therefore, the broad singlet transition is used for Zeeman slowing, as it enables much faster deceleration and consequently requires a shorter Zeeman slower length. In order to completely slow down an atom, it should be in resonance with the slowing laser beam over the slowing length. It can be done by inducing the Zeeman effect by means of the magnetic field, which makes the atoms in resonance with the laser light.

The magnetic-field profile of the Zeeman slower is obtained by maintaining a constant effective detuning during the slowing process. The effective detuning experienced by an atom moving with velocity $v(z)$ is

$$\delta_{\text{eff}} = \delta + kv(z) + \frac{\mu B(z)}{\hbar}, \tag{3.4.4}$$

where δ is the laser detuning, $kv(z)$ is the Doppler shift, and $\mu B(z)/\hbar$ is the Zeeman shift. For continuous resonance during deceleration, the effective detuning is set to zero:

$$\delta + kv(z) + \frac{\mu B(z)}{\hbar} = 0. \tag{3.4.5}$$

Assuming constant deceleration a, the atomic velocity satisfies

$$v^2(z) = v_0^2 - 2az. \tag{3.4.6}$$

Defining the Zeeman slower length as

$$L = \frac{v_0^2}{2a}, \tag{3.4.7}$$

The velocity becomes

$$v(z) = v_0\sqrt{1 - z/L}. \tag{3.4.8}$$

Substituting this into the resonance condition gives the required magnetic-field profile:

$$B(z) = -\frac{\hbar}{\mu}\left(\delta + kv_0\sqrt{1 - z/L}\right). \tag{3.4.9}$$

We adopted a spin-flip Zeeman slower design which generates a zero crossing magnetic field profile that requires small coil currents to generate a larger field span [87, 88]. The required magnetic field profile aims for the atoms with a velocity of 350 m/s. In our setup, the magnetic field profile is shared by two segments of coils in which current flows in opposite directions. The first segment has two sets of coils, coil A and coil B, where the current flows in positive direction, and the second segment has coils C, and coil D, where the current flows in negative direction. Coils A and D are made of 11 mm diameter wire carrying the higher current around 115 A, but in opposite directions to generate the higher magnetic field at the end and entrance of the Zeeman slower. Coil A has five layers, while Coil D has six layers. Similarly, coils B and C are made of 7 mm diameter, in which 30 A current flows in opposite directions. Coil B and C have five and three layers, respectively, with progressively reducing loops, as shown in Fig. 3.12. A 4 cm space between coils B and C gives zero crossing. The coils are wound around 48 mm over the 50 cm CF40 nipple.

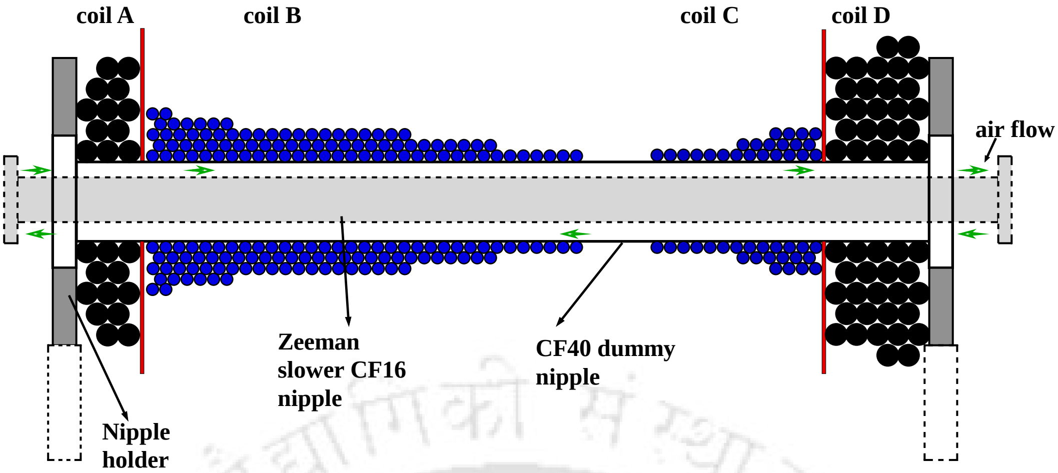

Figure 3.12: Zeeman slower coil design.

The number of layers and turns for each coil is determined by the Matlab simulation programme to match the generated magnetic field with the required magnetic profile as shown in Fig. 3.13(a). The simulated magnetic field was verified by replicating the coils on the dummy nipple as per the Matlab program, and the measured magnetic field matches the simulation as shown in Fig. 3.13(b). The field profile shown in Fig. 3.13(b) differs slightly from the required Zeeman-slower field of Fig. 3.13(a) because it was designed to be experimentally realizable with the available coil geometry and winding constraints. The profile in Fig. 3.13(b) was used primarily to validate the magnetic-field simulation by comparing the simulated field with the measured field. The close agreement between the two confirms the accuracy of the simulation.

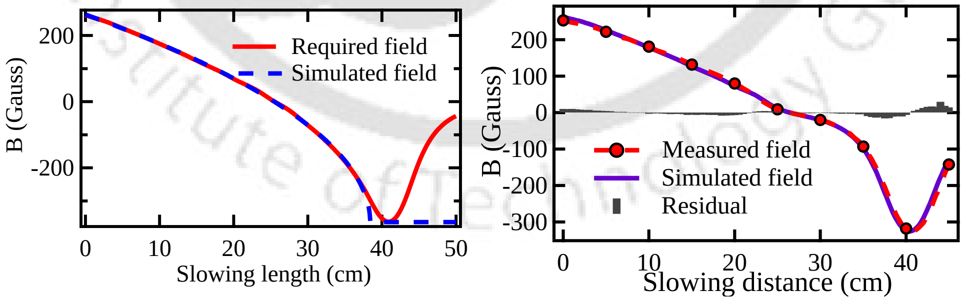

(a) (b)

Figure 3.13: (a) Required magnetic field profile (simulated magnetic field) in red line (blue dashed line) for the Zeeman slower. (b) Simulated magnetic field (in blue solid line) and measured magnetic field (red dotted with circle) of the dummy nipple. The residual difference between the two profiles is also shown in black bars.

3.4.1 Zeeman slower testing

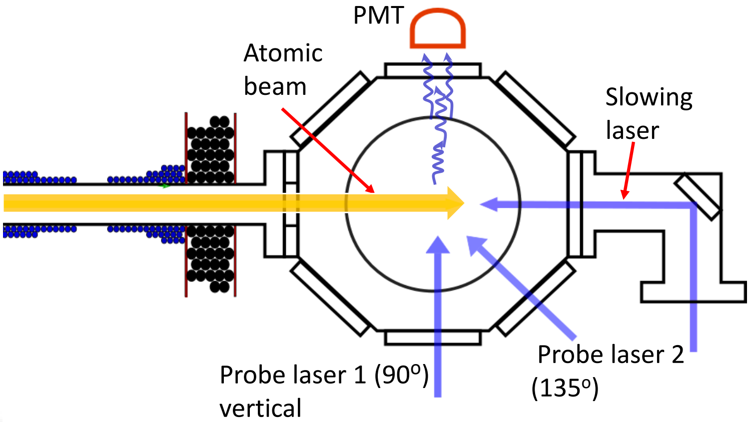

Figure 3.14: Optics scheme for testing of Zeeman slower performance.

The Zeeman slower was tested using two blue laser probe beams directed into the MOT chamber at angles of 135° and 90° with respect to the atomic beam direction, as shown in Fig. 3.14. The probe beam at 135° provides information about the atomic velocity distribution through the Doppler effect, while the probe beam at 90° is used as a Doppler-free reference.

The Zeeman slowing beam, which counter-propagates with the atomic beam, was detuned by 500 MHz to selectively slow ^{174}Yb atoms with an initial velocity of approximately 350 m/s. The fluorescence spectra obtained in the presence of both probe beams and the slowing beam under different magnetic field strengths are shown in Fig. 3.15.

In Figs. 3.15(a)–(c), a prominent peak appears on the left side (marked by a red rectangle), corresponding to the slowed atoms produced by the Zeeman slower at lower operating currents. The peak on the right side (marked by a black rectangle) originates from the zero-velocity group of ^{174}Yb atoms due to the probe beam 1 at 90°. With an increase in the coil current, and hence the magnetic field strength, the fluorescence peak from the slowed atoms moves closer to the reference peak associated with zero-velocity atoms. When the coil current reaches the designed operating value, the two peaks merge, as shown in Fig. 3.15(d), indicating that the atomic beam is efficiently slowed.

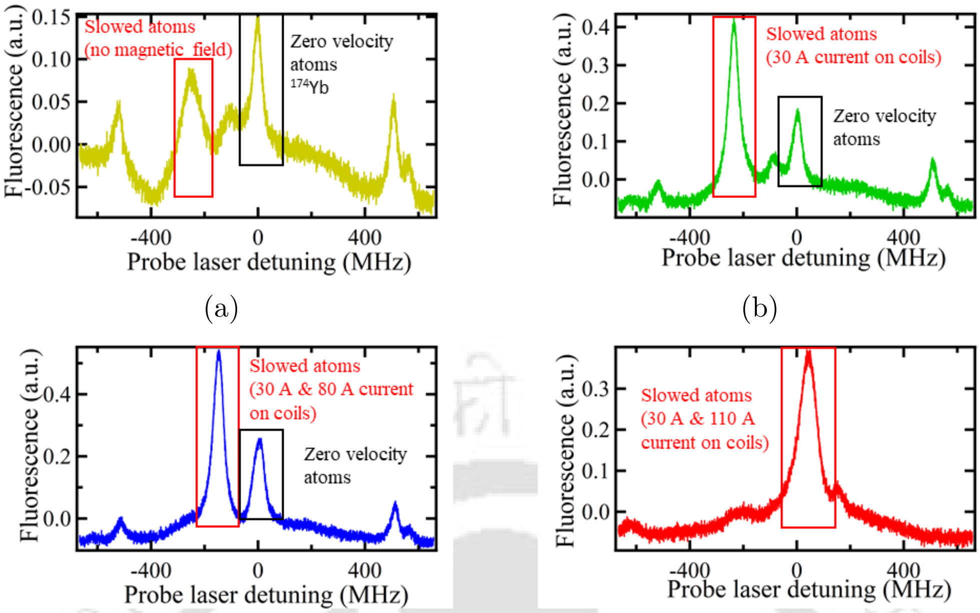

(a) (b)

(c) (d)

Figure 3.15: Fluorescence spectrum in the presence of both probe beams (a) in the presence of slowing beam with no magnetic field,(b) 30 A in coil B, and C and 0 A in coil A, and D, (c) 30 A in coil B, and C and 80 A in coil A and D, and (d) 30 A in coil B, and C and 110 A in coil A and D.

3.5 Laser system

3.5.1 399 nm laser system

We used two laser systems for addressing the blue transition $^1S_0 \rightarrow {}^1P_1$ at 398.9 nm. One is a commercial Toptica DL Pro HP laser used for the MOT, and the other is a MOGLabs injection locking amplifier (ILA) system for the Zeeman slower beam. Initially, we expected the MOGLabs ILA to be sufficient for our requirements. However, we encountered a persistent operational problem with the system. Therefore, we later upgraded the existing 420 nm Toptica laser to operate at 399 nm by replacing the laser diode.

The Toptica system is a commercial external-cavity diode laser (ECDL) that provides a maximum output power of approximately 120 mW. This laser system is dedicated to MOT cooling beams.

Injection locking amplifier (ILA) laser system

A schematic diagram of the commercial injection-locked laser system from MOGLabs (Model: ILA) is shown in Fig. 3.16. It has a low-power stable seed laser and a high-power amplifier laser. The seed laser is an ECDL with a Nichia laser diode (NDUA116T) of 75 mW output power, while the amplifier laser is made of a laser diode, emitting 250 mW of output power. The seed and amplifier lasers are optically isolated by Faraday isolators. Both lasers are controlled by different laser controllers (DLC for the seed laser and ILD for the amplifier diode laser). The laser beam from the seed laser passes the half-wave plate and PBS, which splits the beam into two parts. One part of the beam (around 20-30 mW power) is injected into the amplifier laser through two mirrors, while the remaining part of the beam can be used for stabilization of seed laser frequency at $^1S_0 \rightarrow {}^1P_1$ broad transition. A laser beam with a power of 250 mW is delivered from the amplifier as the final output. When the amplifier laser diode is seeded with the seed laser, the amplified output retains the same spectral characteristics as the seed. The tiny portion of the output light from the amplifier laser is sent to beam-sampling optics to monitor the active injection of locking of the amplifier. A major challenge encountered with the system was the recurring failure of the amplifier diode module.

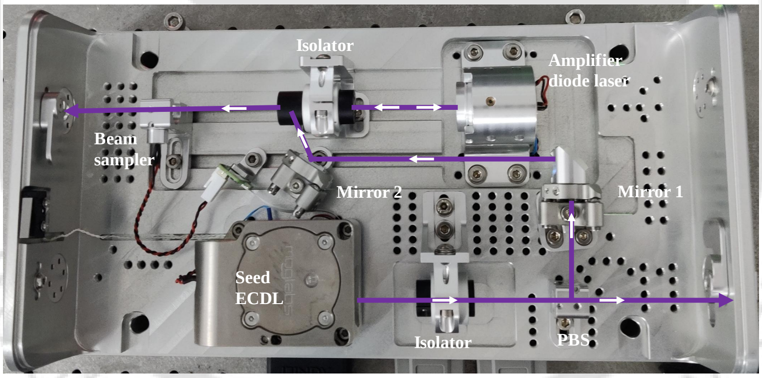

Figure 3.16: ILA laser system.

The first failure: After the installation of the laser, it operated normally for some time until a day when we observed abnormal behavior of the amplifier diode laser. The output power of the amplifier laser suddenly dropped from about 210 mW to less than 100 mW while operating at an amplifier diode current of 250 mA with an injected seed power of 30 mW.

Further, we measured the amplifier laser output power (after the isolator) as a function of the amplifier diode current without seed injection. The measurement showed that the amplifier power began to decrease beyond 180 mA. Moreover, the obtained power–current (PI) curve did not match the reference measurement taken during the initial installation of the laser (or the test report from the company), as shown in Fig. 3.17.

Next, we passively locked the amplifier laser to the seed laser (30 mW injected power) and observed that seeding occurred only up to an amplifier diode current of about 130 mA. Beyond this point, the output power started to drop, and the beam quality deteriorated, showing a dark line along the beam center, as shown in Fig. 3.18.

The issue was reported to MOGLabs; however, the cause could not be identified remotely. Consequently, the ILA system was sent back to the company for inspection, where the amplifier diode was replaced after their evaluation.

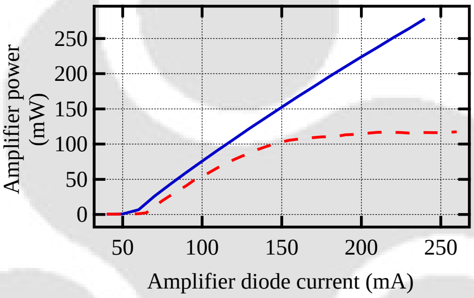

Figure 3.17: The power comparison of the amplifier output during the installation (blue solid line) and after the failure (red dashed line). The power measured after the isolator with no seeding.

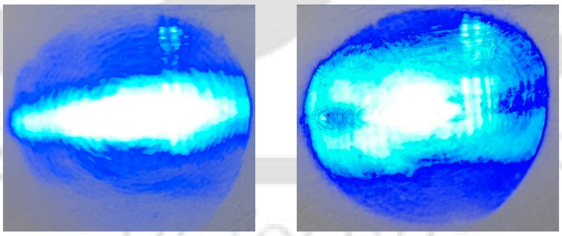

(a) (b)

Figure 3.18: Amplifier output beam quality (a) at amplifier diode current at 110 mA (b) at 140 mA with 30 mW injected seed power. The beam is expanded using a single lens.

The second failure: After the first amplifier diode failed, a new diode (serial number: A20M570034, reference: RMA2022-82) was installed in the MOGLabs ILA system at the factory. However, after only a few days of operation, its performance again started to degrade. The threshold current of the amplifier (without seed) increased from about 70 mA to 120 mA, and the PI curve changed noticeably, both with and without seeding (20 mW at 398.91 nm) as shown in Fig. 3.19. The beam shape also became distorted as shown in Fig. 3.20. During this time, the amplifier was operated at a current of 140–150 mA and a temperature of 18 °C, with seed power of 20 mW. The issue was reported to MOGLabs, and they explained that the performance limitations were mainly due to the restricted availability of reliable diodes at this wavelength. The manufacturer had already reduced the specifications of this model based on earlier failures. The diode was covered under warranty, and a replacement unit was arranged while the failed diode was returned to MOGLabs for further investigation by the company.

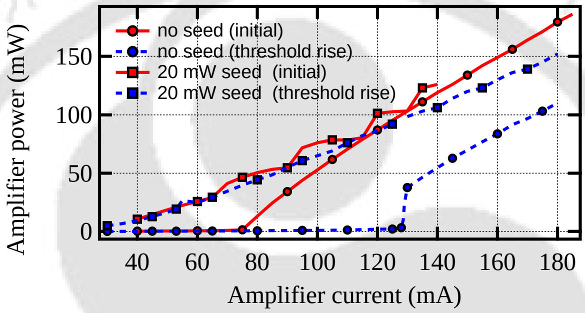

Figure 3.19: The power comparison of the amplifier output after replacement (red solid line) and after the failure (blue dashed line). The amplifier power measured with (square marker) and without (circle marker) seeding.

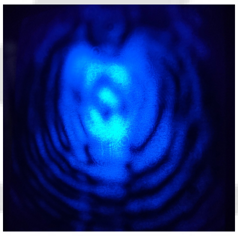

Figure 3.20: Amplifier output beam quality degradation. The beam is expanded using a single lens.

The third failure and diagnostic investigation: This time, the new replacement amplifier diode (serial number: BA8220-3, reference RMA2024-12) was replaced manually by us with the help of the instruction manual. It failed again after just 60 hours of operation, after the replacement, by showing similar failure behaviors such as a reduction in power and beam profile degradation. We were operating the amplifier diode at approximately 117 mA with a seed injection of 4 mW, both of which are below the suggested operating current (140 mA) and seed power (7.4 mW). To prevent another failure, we intentionally operated the diode at lower currents with low seed injection. Despite these precautions, the diode exhibited the same problematic behavior as the previously failed diodes. Upon consulting MOGLabs technical support, it was suggested that the failures were unlikely due to the diodes themselves, as similar repeated failures had not been reported by other users. Two possible causes were proposed: (i) environmental factors such as condensation or grounding-related current surges, and (ii) faults in the amplifier diode current controller (ILD). Since the seed laser, operating under the same thermal and environmental conditions, did not exhibit similar degradation, the latter possibility appeared more likely.

We also verified the electrical grounding configuration. The amplifier diode mount was isolated from the chassis using nylon washers, as specified in the mounting instructions, while the seed laser body was shorted to the chassis. The chassis itself was grounded to the optical table, which had an insulating surface coating but was not electrically isolated from ground. MOGLabs later clarified that the amplifier diode should remain isolated, while isolation of the seed laser is preferable but not critical unless electrical noise is observed. Additionally, MOGLabs explained that the amplifier diode body must be electrically isolated from ground because, for several diode models, the diode can be internally connected to the cathode. Since the ILD operates in a common-anode configuration—where the anode is held at ground potential—the cathode must be maintained at a negative potential for current to flow. If the amplifier diode body were not isolated, both the cathode and anode would be grounded simultaneously, preventing current flow through the diode.

To investigate further, we examined the current ramping behavior of the ILD. When the amplifier laser was switched on, the operating current was observed to rise instantaneously to the set value without the expected soft-start behavior. The ILD display confirmed that the measured current jumped directly to the I-set point. Power measurements of the amplifier laser using a fast photodetector showed a rise time of approximately 25 ms (at 120 mA), while the seed laser exhibited a much slower rise time of 2.3 s (at 60 mA), confirming that the amplifier current is applied much more abruptly.

Furthermore, MOGLabs confirmed that the ILD controller is designed to include a soft-start feature, and under normal conditions, a rise time of approximately 100 ms is expected for a 100 mA current setpoint. However, upon further internal investigation, their engineering team discovered that the ILD exhibited unexpected behavior in the current rise and fall characteristics, leading to large transient current spikes during laser diode switch-

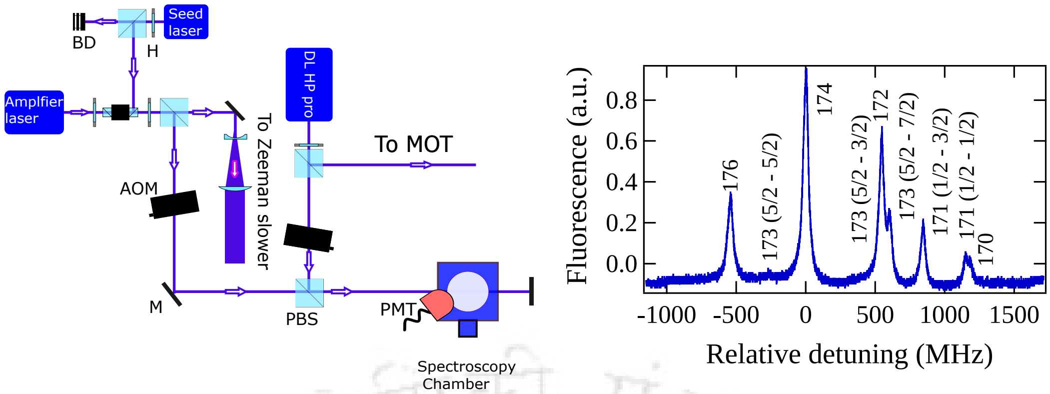

(a) (b)

Figure 3.21: (a) A schematic of the fluorescence spectroscopy setup for blue lasers. (b) Fluorescence spectrum for blue transition at 399 nm.

ing. These transients were believed to be the primary cause of the diode degradation and premature failure observed in our system.

MOGLabs subsequently developed and tested a new firmware version that corrects these issues. They also arranged to provide a replacement amplifier diode (serial number: BA8456-1, reference RMA2024-53) and detailed instructions for performing the firmware update on our ILD controller. After performing the firmware update, we measured the rise time of the existing failed amplifier diode and found it to be approximately 300 ms at 110 mA, compared to 25 ms with the earlier firmware version, confirming a significant improvement in the current ramping behavior.

However, since our experiments had already been hampered by repeated diode failures, we decided to replace the diode and mount the amplifier diode assembly in our home-built laser housing, driven by a Thorlabs current controller. The system could be successfully seeded using the existing ILA seed laser. The passive injection lock was found to be sufficiently stable for operating the magneto-optical trap (MOT) experiments. This laser system is currently dedicated to serving as the Zeeman slower beam in the experiment.

Frequency stabilization using fluorescence spectroscopy

Both blue lasers are frequency-stabilized using fluorescence spectroscopy performed in a single spectroscopy chamber, as shown in Fig. 3.21(a). The beams from the two lasers are combined using a polarizing beam splitter (PBS) and directed into the spectroscopy chamber. The laser frequency is modulated using an acousto-optic modulator (AOM), and the beam interacts at 90° with the thermal atomic beam. The resulting fluorescence emitted by the excited atoms is detected by a photomultiplier tube (PMT).

The two spectroscopy beams are modulated at different modulation frequencies: 10 kHz for the Toptica laser and 50 kHz for the MOGLabs laser. For the ILA system (MOGLabs), the fluorescence signal is processed by a homemade lock-in detection box that generates the error signal. This error signal is then fed to the seed ECDL controller, which uses its internal PID loop to stabilize the laser frequency. It is important to note that there is a small frequency offset between the amplifier and seed laser frequencies, as the amplifier does not exactly follow the seed laser frequency. Therefore, the seed laser is locked in such a way that the amplifier output frequency precisely addresses the desired atomic transition, and the spectroscopy is performed using the amplifier output.

In the case of the Toptica laser, a DigiLock 110 module is used to generate the error signal and stabilize the frequency. The observed fluorescence spectrum for the different isotopes of Yb atoms is shown in Fig. 3.21(b).

3.5.2 556 nm laser system

The 556 nm laser is generated (typically 10 mW) by frequency doubling using a Potassium Niobate ($KNbO_3$) crystal inside a bow-tie cavity. The fundamental laser at 1112 nm with a typical power of 200 mW is generated using an ECDL made of a diode laser (SM-1120-TO-500, Innolume). The 556 nm laser beam is further divided into two portions using PBS for spectroscopy and MOT. A pair of AOMs is used on the path of the spectroscopy beam for the MOT detuning and the frequency modulation required for the laser stabilization, as shown in Fig. 3.22(a). The frequency of the 556 nm laser is stabilized using fluorescence spectroscopy on the intercombination transition. The spectroscopy beam, derived from one branch of the divided 556 nm output, is directed through a thermal atomic beam at an angle of 90° inside the spectroscopy chamber. The fluorescence emitted by the excited atoms is detected using a photomultiplier tube (PMT). The green transition fluorescence spectrum for the different isotopes of Yb atoms is shown in Fig. 3.22(b).

The fluorescence signal is then processed by a Digilock to generate an error signal, which is fed back to the piezo of the 1112 nm ECDL for active frequency stabilization via its internal PID controller.

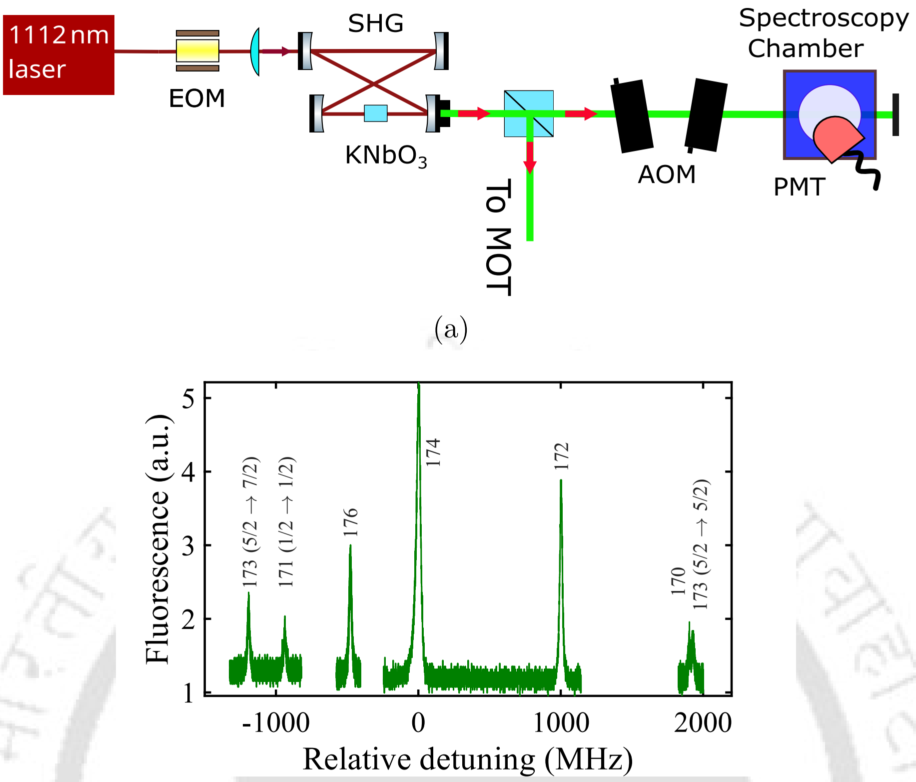

(a)

(b)

Figure 3.22: (a) A schematic of the 556 nm laser system. (b) Fluorescence spectrum for green transition at 556 nm.

3.5.3 507 nm laser system for $^1S_0 \rightarrow {}^3P_2$ clock excitation

We constructed a home-made ECDL system for $^1S_0 \rightarrow {}^3P_2$ clock transition. A laser diode (RLT510-50MGS, Roithner) is assembled in Littrow configuration [90] with a cavity length of 4.5 cm as shown in Fig. 3.23. The typical gain bandwidth of the free-running laser diode is around 504 nm. However, the gain bandwidth of the laser diode was pulled to near 507 nm at 37 °C in Littrow configuration using a holographic grating (GH13-24U, Thorlabs). It delivers maximum power of 15 mW at 37 °C. We tried to increase the cavity length further to reduce the linewidth of the laser; however, the laser diode did not operate at the desired wavelength.

Saturation Absorption Spectroscopy of Iodine at 507 nm

We performed saturation absorption spectroscopy (SAS) on iodine (I2) molecules using the 507 nm laser. The hyperfine transition P(40) (52–0) of iodine serves as a frequency

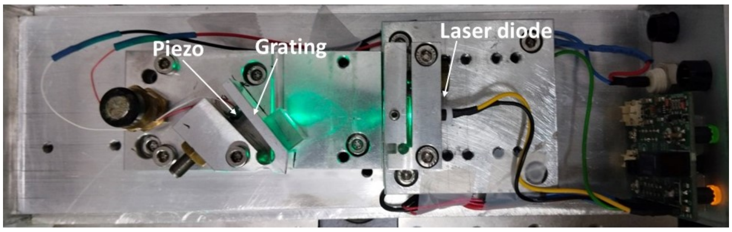

Figure 3.23: 507 nm laser system.

reference for the ^{1}S0 → $^{3}P_{2}$ clock transition of Yb as this transition frequency is very close to the $^{1}S_{0}$ → $^{3}P_{2}$ Yb clock transition. The transition notation follows the form P(J″) $\gamma'' \leftarrow \gamma'$, where the first letter (P or R) indicates the rotational branch, J″ denotes the rotational quantum number of the excited state (ΔJ = -1 for the P branch), and γ' and γ'' represent the vibrational quantum numbers of the ground and excited states, respectively.

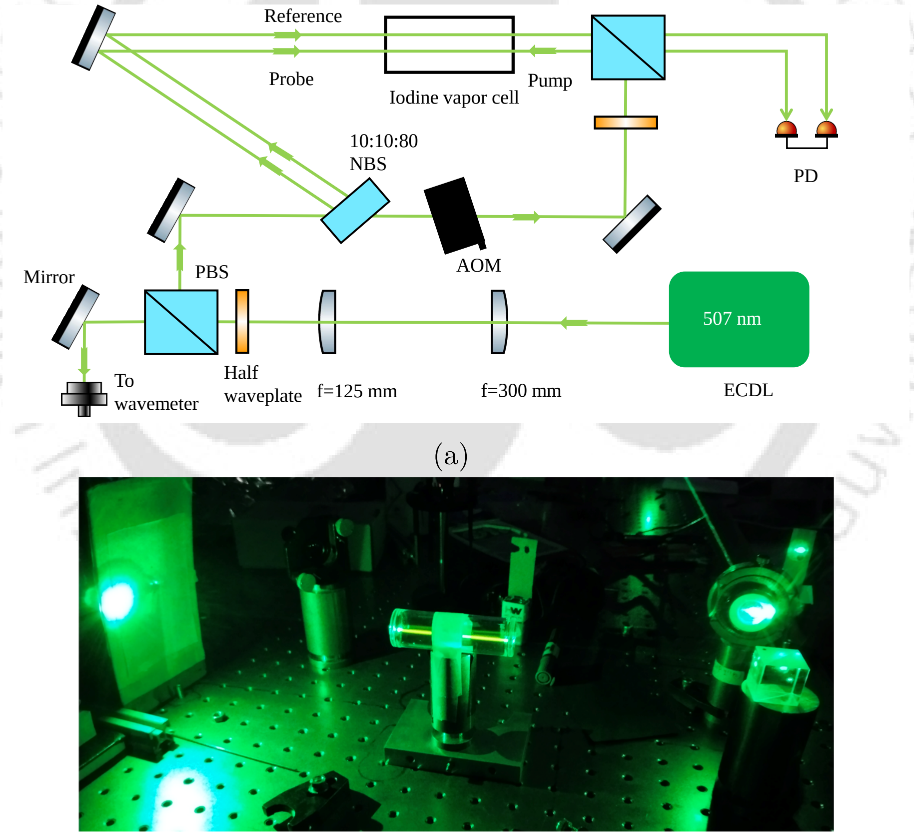

(a)

(b)

Figure 3.24: (a) A schematic of the optics layout for the SAS setup.
(b) 507 nm fluorescence from the iodine vapor cell.

For the P(40) (52–0) transition, there are 15 hyperfine components since J″ is an even number. A schematic of the experimental setup for saturation absorption spectroscopy

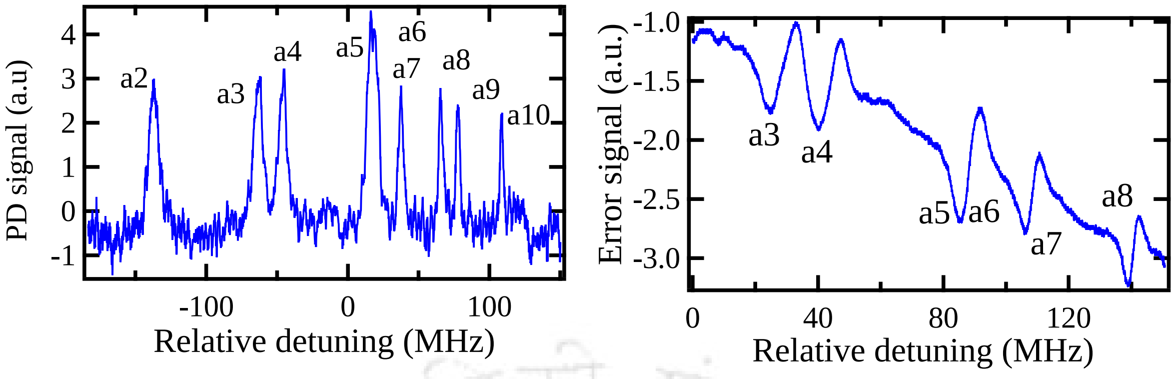

(a) (b)

Figure 3.25: The observed (a) SAS spectrum and (b) error signal for the P(40) (52–0) transition of the iodine molecule at 507 nm.

is shown in Fig. 3.24. An iodine vapor cell of 8 cm length and 20 mm diameter is used as the reference medium. The pump and probe beam powers are 5 mW and 350 μW, respectively, with a beam diameter of 1.5 mm.

A reference beam is used to subtract the Doppler background; however, it does not completely eliminate the background signal. The absorption signal is detected using a photodiode (PD) and sent to a lock-in amplifier to further suppress the Doppler background through lock-in detection. The pump beam is modulated by an AOM at 2.5 kHz to provide the required modulation for the lock-in technique.

The resulting spectrum is shown in Fig. 3.25(a). In the observed spectrum, nine hyperfine peaks out of the expected fifteen are visible, denoted as a2–a10, limited by the mode-hop-free tuning range of the laser. The narrowest observed linewidth among these peaks is approximately 2 MHz. The corresponding error signal generated from the SAS measurement is shown in Fig. 3.25(b).

4

Yb Experiments

Contents

In this chapter, we present the experimental results related to laser cooling and trapping of Yb atoms. This chapter discusses the blue MOT, the narrow-linewidth green MOT, and our initial attempts to achieve three-photon Rydberg excitation in Yb atoms.

4.1 Blue MOT using the 399 nm transition

The relevant energy-level structure of Yb is shown in Fig. 3.1. Yb possesses two key optical transitions that are suitable for laser cooling: a strong, broad singlet transition at 399 nm corresponding to the $6s^2\ {}^1S_0 \rightarrow 6s6p\ {}^1P_1$ transition, and a weak, narrow-linewidth triplet transition at 556 nm corresponding to the $6s^2\ {}^1S_0 \rightarrow 6s6p\ {}^3P_1$ transition. The singlet transition at 398.9 nm has a natural linewidth of 29 MHz, making it suitable for the first stage of cooling and trapping. The optical layout of the blue magneto-optical trap (MOT) based on the 399 nm transition is shown in Fig. 4.1. The MOT operates in a standard three-beam retroreflection configuration in the presence of a magnetic field gradient of about 45 G/cm. The atomic beam emerging from the oven is pre-slowed by a Zeeman slower beam, which is detuned by approximately 500 MHz below the ${}^1S_0 \rightarrow {}^1P_1$ resonance of ^{174}Yb. This slowing beam is designed to capture atoms with velocities up to ∼250 m/s, typical of Yb thermal velocities at the operating oven temperature. The Zeeman slower beam, which counter-propagates to the atomic beam, has a beam diameter of 16 mm at the entrance window and converges to 6 mm at the nozzle. The slowed atoms are then captured and further cooled in the MOT region by the six cooling beams and the quadrupole magnetic field. Each MOT beam has a diameter of about 30 mm, providing a large capture volume. The MOT beam is detuned by 56 MHz from the resonance. The total power in the MOT beams is approximately 30 mW, while the Zeeman slower beam power is about 60 mW. Once the MOT is loaded, the atom number and temperature are measured using absorption imaging with a weak resonant probe beam at 399 nm. The image of the blue MOT is shown in Fig. 4.2. Under typical operating conditions, the blue MOT contains approximately 5×10^8 atoms at a temperature of around 11 mK. The temperature of the atoms in the MOT was determined using time-of-flight (TOF) absorption imaging. After switching off the trapping fields, the atomic cloud was allowed to expand freely for a variable duration before being imaged using a near-resonant imaging beam. The temperature was extracted from the increase in the spatial width of the cloud between two absorption images taken at different time-of-flight durations. The temperature can be further reduced by lowering the blue-beam power during the final stage of MOT loading. However, the blue MOT is not critical for our experiment. Therefore, we did not attempt to further reduce the temperature and proceeded directly to the green MOT.

4.2 Green MOT using the 556 nm transition

Alkaline-earth elements, such as strontium (Sr), and alkaline-earth-like elements, such as ytterbium (Yb), have attracted significant interest within the field of cold atom physics due to their complex electronic structures and versatile transition properties because of their double-valence electrons. Unlike single-valence-electron species, two-valence-electron atoms offer a spectrum of optical transitions, ranging from broad to ultranarrow-linewidths, which enhance their utility across a variety of cutting-edge applications such as quantum precision measurements [91], serving as frequency references in optical atomic clocks [51, 52], and play pivotal roles in quantum simulations [92] and computation [47–50]. The absence of electron spin in certain isotopes, or the existence of purely nuclear hyperfine levels, further extends their suitability for applications where minimal decoherence is desired. These elements have also emerged as ideal candidates for exploring Rydberg states for quantum computation and simulation, where the dual valence electrons facili-

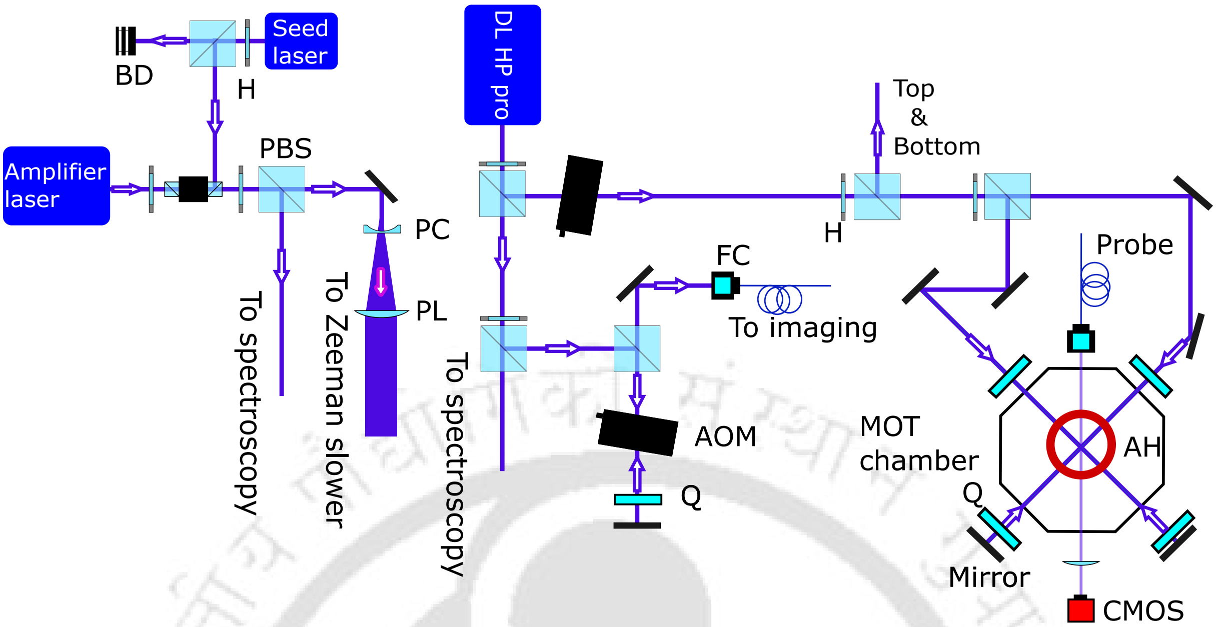

Figure 4.1: Optics layout for the blue MOT. Figure abbreviations: PL– Plano-convex lens, PC–Plano-concave lens, BD– Beam dump, PBS–Polarising beam splitter, Q – $\lambda/4$ wave plate, H – $\lambda/2$ wave plate, FC – fiber coupler, AH – Anti-Helmholtz coil.

tate simultaneous trapping of ground and excited states in optical tweezers [93], as well as optical imaging of Rydberg atoms [94].

For the above applications, one of the important steps is the cooling and trapping in magneto-optical trap (MOT) using narrow intercombination line, as it provides low temperature. However, trapping at this transition is challenging because of low capture velocity. Two-step MOT is used for loading the atoms at narrow transition, where a broad transition is first employed to rapidly capture atoms up to high velocity. This is followed by a transfer to the MOT at the narrow transition by switching off the broad

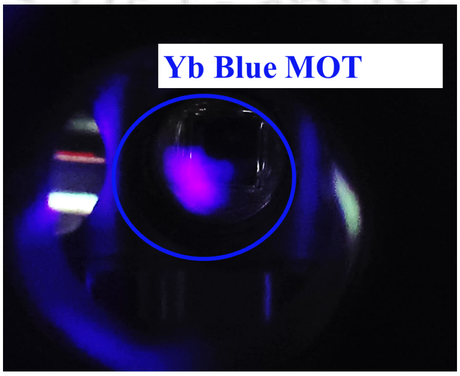

Figure 4.2: Image of the blue MOT.

transition laser beam and lowering the magnetic field gradient. The MOT using narrow transition provides lower temperatures and higher density clouds [95–103]. In many cases, such as in Yb and Sr, the broad transition is not completely closed and limits the number of atoms in the MOT. Therefore, it is preferable to directly load atoms into the MOT using a narrow-linewidth transition, as this transition is closed.

In the case of Yb, direct loading has been demonstrated using the green inter-combination transition at 556 nm (green MOT). The green MOT loads a larger number of atoms, but with a slow loading rate [104]. The direct loading of the green MOT is possible by utilizing the power broadening effect or broadening the laser linewidth using an acousto-optic modulator (AOM) or an electro-optic modulator (EOM), but requires high power of the green laser [95]. The green laser at 556 nm is not directly available from diode lasers and is typically generated either by frequency doubling of an infrared laser or using a dye laser pumped by an argon-ion laser [95]. To generate high green power (on the order of a few hundred mW), frequency doubling is performed using a cavity-enhanced setup, where a nonlinear crystal is placed inside a resonant cavity. This cavity increases the circulating power of the fundamental laser, thereby improving the conversion to green light. However, lower green powers (a few tens of mW) can be achieved using a simpler single-pass frequency doubling through a nonlinear crystal [105]. For applications such as portable atomic clocks, it is desired to avoid the frequency-doubling cavity and hence to load the green MOT even with low power of the green laser. Core-shell configuration [106, 107], where a hollow core is created (by masking) in the laser beam of the broad transition and filled by the weak transition laser beam, has been very useful for loading the green MOT faster.

In this work, we load the green MOT of Yb using low green laser power in the core-shell configuration. We create a hollow core in the blue laser beam such that the masked (using a mirror) portion can be utilized for 2D cooling. We also explore the other configuration of center-shifted dual MOT. In this configuration, the overlap region of the three counter-propagating broad transition (blue) laser beams is shifted towards Zeeman slower with a non-zero magnetic field. The atoms are pre-cooled and partially trapped by the blue transition as the magnetic field is non-zero. These atoms are trapped in the green MOT once they enter the green MOT region.

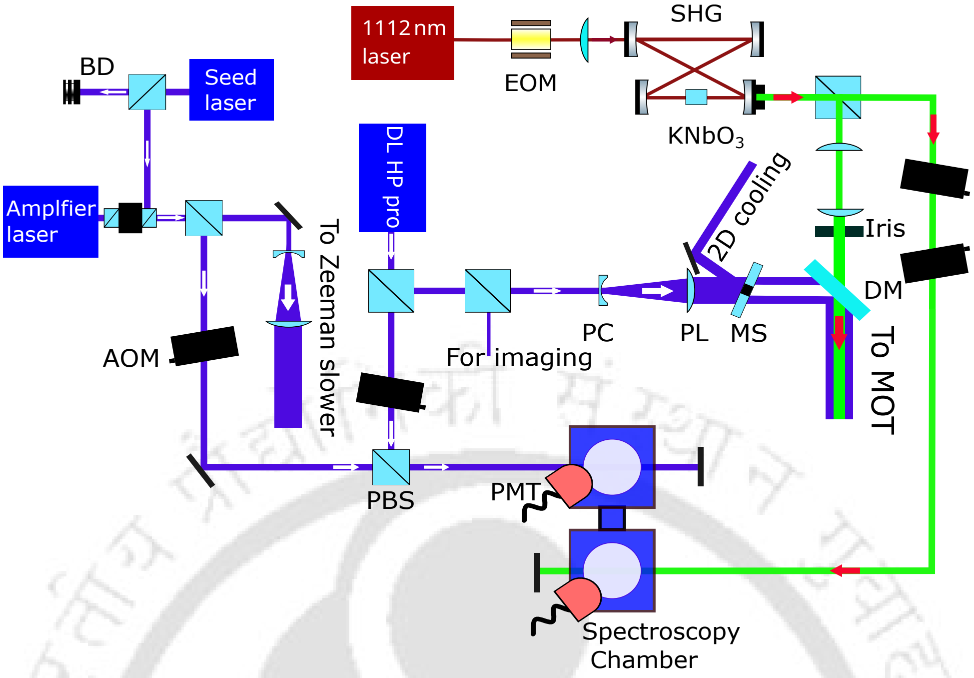

Figure 4.3: Optics layout for core-shell MOT. Figure abbreviations: PL– Plano-convex lens, PC–Plano-concave lens, DM– Dichroic mirror, PMT– Photomultiplier tube, BD– Beam dump, MS–Mask, PBS–Polarising beam splitter.

4.2.1 Optics scheme

The MOT mixing scheme for the core-shell configuration is shown in Fig. 4.4(a). A hole is created at the center of the blue beam by passing it through a circular mirror attached to a glass window, which is placed in its path. It reflects the central portion of the beam and is utilized for 2D cooling. This approach allows the unused (masked) power to be recycled for experiments. The hole is then filled with green light of a desired size using a dichroic mirror. An iris is placed in the path of the green beam to control its beam size. The mixed beams are further split into three beams using PBSs and sent to the MOT chamber. Mechanical shutters are used in the paths of lasers for switching the lasers off and on.

In the center-shifted dual MOT configuration, the blue beam and green beam are aligned side-by-side as shown in Fig. 4.4(b). The blue and green beams have the same beam diameter of 9 mm with powers of 30 mW and 9 mW, respectively. The blue beam diameter is limited to 9 mm due to constraints on the optical access of the MOT chamber windows. The overlapping region of green MOT beams is aligned to coincide with the region of zero magnetic field, while the blue beams create the blue MOT between the green MOT

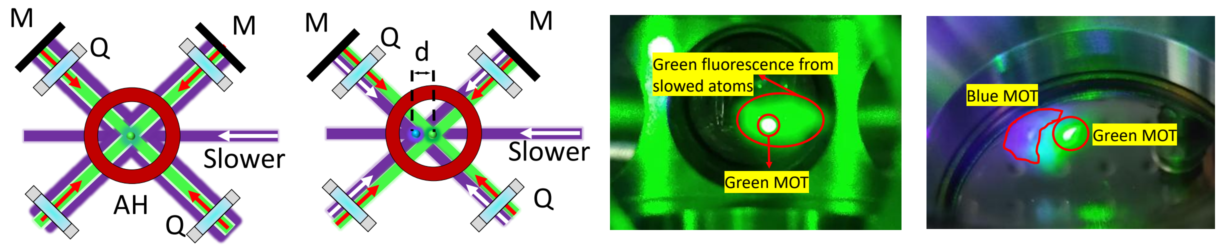

(a) (b) (c) (d)

Figure 4.4: Top view of the MOT set-up of (a) core-shell and (b) center-shifted dual MOT configuration. Figure abbreviations: AH – Anti-Helmholtz coil, M– Mirror, Q – Dual $\lambda/4$ wave plate, d – distance between blue and green MOT. The 399 nm and 556 nm beams are shown in violet and green color, respectively. Images of green MOT in core-shell configuration (c) and center-shifted dual MOT configuration (d).

and the exit of the Zeeman slower, positioned closer to the green MOT at a non-zero magnetic field. We use absorption imaging analysis with a CMOS camera (CS135MUN, Thorlabs) to measure the number of atoms in the green MOT. The atom number was obtained from the absorption images by calculating the optical density of the atomic cloud from the probe and reference images. The optical density was integrated over the cloud area and converted to atom number using the resonant absorption cross-section of the transition [59].

4.2.2 Numerical simulation

We numerically simulate the capture dynamics of the 3D MOT using a Monte Carlo approach for both center-shifted and core–shell configurations. The schematic representation of the simulation geometry is shown in Fig. 4.5. Atoms are initialized at the exit of the Zeeman slower and propagate toward the MOT center. Initial atomic positions are sampled uniformly over a circular Zeeman slower aperture of radius r_{aper} by generating the radial coordinate as $r = r_{\text{aper}}\sqrt{\xi}$ and the azimuthal angle as $\phi = 2\pi\eta$, where ξ and η are uniformly distributed random numbers in the interval $[0, 1]$. The square-root transformation ensures a uniform spatial distribution over the circular aperture. The corresponding Cartesian coordinates are given by $x = x_{\text{aper}}$, $y = r\cos\phi$, and $z = r\sin\phi$, where $r \in [0, r_{\text{aper}}]$. Here, x_{aper} denotes the longitudinal position of the Zeeman slower exit. Initial velocities are directed along the atomic beam axis toward the MOT center with magnitude v_0, such that $\mathbf{v}_0 = v_0\hat{\mathbf{e}}_{\text{axis}}$.

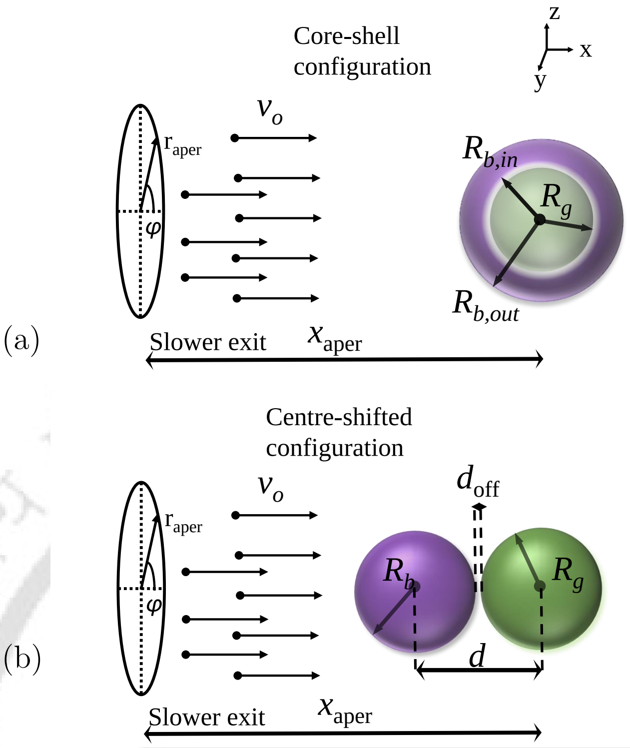

Figure 4.5: Illustration of the simulation geometry for (a) core-shell and (b) center-shifted MOT configurations.

For the core-shell region, the MOT configuration consists of a narrow-line green trapping region of radius R_g at the center and a surrounding broad-line blue shell extending from inner radius $R_\mathrm{b,in}$ to outer radius $R_\mathrm{b,out}$. In the core–shell configuration, the radiative force from the blue beam is assumed to act only in the outer shell region, while the green beam is confined to the central core region.

For the center-shifted configuration, the MOT consists of a broad-line blue trapping region that is spatially displaced from the narrow-line green MOT center by a fixed longitudinal distance d. In this geometry, the green MOT of radius R_g is located at the origin and provides the final cooling and trapping, while the blue MOT of radius R_b is centered at $x = -d$ and acts as a pre-cooling region for incoming atoms. The blue and green laser fields contribute independently to the radiative force only within their respective spatial regions, such that atoms are first decelerated and compressed by the blue MOT before entering the green MOT region, where they are further cooled and captured.

For both configurations, the radiation pressure force acting on an atom is calculated independently along each spatial direction and is given by $F_i = \hbar k(R_i^+ - R_i^-)$, where

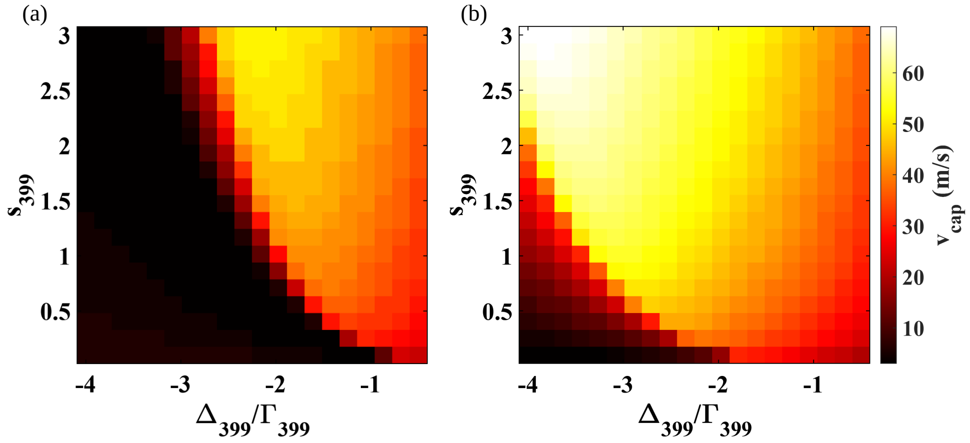

Figure 4.6: Capture velocities vs detuning (Δ_{399}) and saturation parameter (s_{399}) of blue laser for (a) center-shifted and (b) core-shell configurations. The simulation parameters for center-shifted are, $s_{556} = 100$, B = 12 G/cm, $\Delta_{556} = -10\Gamma_{556}$, $R_\mathrm{B} = 4.5$ mm, $R_\mathrm{g} = 4.5$ mm, and $d_\mathrm{off} = 0$ mm, and for core-shell are, $s_{556} = 100$, B = 12 G/cm, $\Delta_{556} = -10\Gamma_{556}$, $R_\mathrm{b,out} = 9$ mm, $R_\mathrm{b,in} = 3$ mm, and $R_\mathrm{g} = 3$ mm.

$R_i^\pm$ are the scattering rates from the counter-propagating laser beams. Each scattering rate is modeled as $R^\pm = (\Gamma/2)\, s \big/ \left[1 + s + 4\left((\Delta \mp kv \mp \Delta_Z)/\Gamma\right)^2\right]$, where s is the local saturation parameter [60, 61, 64], Δ is the laser detuning, kv is the Doppler shift, and Δ_Z is the Zeeman shift. A magnetic quadrupole field of the form $\mathbf{B} = B'(x\hat{x} + y\hat{y} - 2z\hat{z})$ is assumed, leading to a Zeeman shift that is linear in position and provides the restoring force necessary for trapping.

The atomic equations of motion, $\dot{\mathbf{r}} = \mathbf{v}$ and $\dot{\mathbf{v}} = \mathbf{F}(\mathbf{r}, \mathbf{v})/m$, are integrated using a fixed-step fourth-order Runge–Kutta method. Each trajectory is propagated until the atom either leaves the simulation spherical space or reaches the green MOT region with sufficiently low velocity. An atom is considered captured if it satisfies $\|\mathbf{r} - \mathbf{r}_\mathrm{MOT}\| \leq R_\mathrm{g}$ and $\|\mathbf{v}\| \leq v_\mathrm{cap,th}$, where $v_\mathrm{cap,th}$ is a predefined capture velocity threshold less than the Doppler limit velocity of green transition. The simulation is repeated for a range of initial longitudinal velocities v_0, and for each velocity, the capture fraction is defined as the fraction of atoms that meet the capture criterion. The capture velocity is extracted as the maximum initial velocity for which the capture fraction remains non-zero.

The simulated capture efficiency vs detuning and saturation parameter of the blue laser is shown in Fig. 4.6(a) for the center-shifted and Fig. 4.6(b) for the core–shell MOT configuration. The maximum capture velocity is about 70 m/s for the core–shell configuration at $s_{399} = 3$ and $\Delta_{399} = -3.5\Gamma_{399}$, and about 50 m/s for the center-shifted configuration

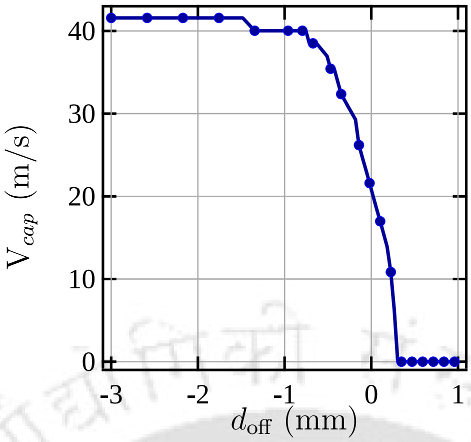

Figure 4.7: Capture velocity vs distance (d_{off}) between the periphery of blue and green MOT regions in center-shifted MOT configuration. The simulation parameters are, $s_{556} = 100$, $s_{399} = 1$, B = 12 G/cm, $\Delta_{556} = -10\Gamma_{556}$, $R_{\mathrm{b}} = 4.5$mm, and $R_{\mathrm{g}} = 4.5$ mm.

at $s_{399} = 3$ and $\Delta_{399} = -2\Gamma_{399}$.

In the experiment, the blue-beam saturation parameter (s_{399}) in the center-shifted configuration is approximately twice that in the core–shell configuration. For the experimental parameters used, the capture velocity is about 40 m/s for the core-shell configuration and 20 m/s for the center-shifted configuration. Consequently, we observe that a larger number of atoms are loaded into the green MOT in the core–shell configuration compared to the center-shifted configuration, even though the blue-beam intensity is higher in the latter case. This behaviour arises because the center-shifted MOT is highly sensitive to the spatial separation between the blue MOT and the green MOT regions, as shown in Fig. 4.7. When the two regions overlap, the capture efficiency is comparable. However, as the separation increases, the capture velocity rapidly decreases and eventually drops to zero. In this regime, even atoms with zero initial velocity are not captured because the magnetic field gradient accelerates them via the blue magneto-optical force to velocities beyond the capture range of the green MOT.

4.2.3 Results and discussion

Table 4.1 summarizes the number of atoms loaded in green MOT with various configurations. The image of the green MOT loaded in the core-shell configuration is shown in Fig 4.4(c). The blue beam with a diameter, $\phi_{\mathrm{B}} = 18$ mm and the hollow core (HC)

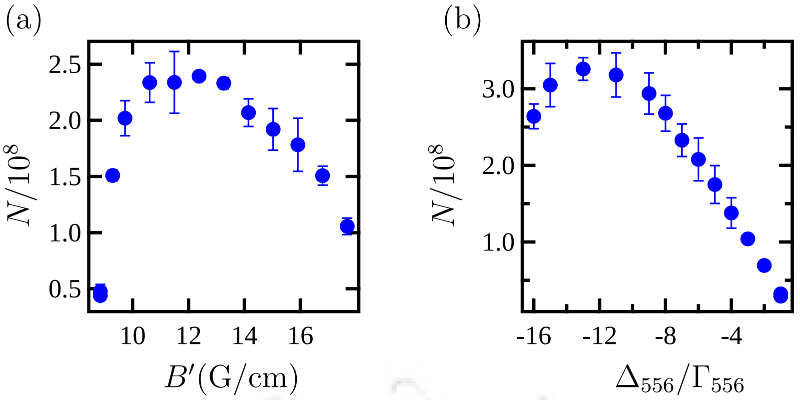

Figure 4.8: Number of atoms (N) in the green MOT vs (a) magnetic field gradient (B') and (b) detuning (Δ_{556}) of the green laser. Experimental parameters: blue MOT laser power, $P_{399} = 25$ mW, green MOT laser power, $P_{556} = 7$ mW, blue MOT laser detuning, $\Delta_{399} = -2\Gamma_{399}$, blue beam diameter, $\phi_{\mathrm{B}} = 18$ mm and the diameters of the hollow core and the green beam are both $\phi_{\mathrm{G/HC}} = 6$ mm.

diameter, $\phi_{\mathrm{HC}} = 6$ mm gives the maximum number of atoms. The total power in the blue MOT beam after creating a hollow core is 30 mW. We reflect 12 mW of blue power that can be used for 2D cooling. We now discuss our experimental results of the green MOT in the core-shell configuration.

First, we discuss the atom number (N) of the green MOT with magnetic field gradient (B') and the green MOT laser detuning (Δ_{556}) as shown in Fig. 4.8. N reaches maximum at around $B' = 12$ G/cm and then it decreases with further increase in B' as shown in Fig. 4.8(a). For green MOT laser detuning, N is maximum at $\Delta_{556} = -12\Gamma_{556}$ as shown in Fig. 4.8(b). At the operating intensity, the green transition is strongly power-broadened, $\Gamma' = \Gamma_{556}\sqrt{1+s} \approx 19\,\Gamma_{556}$, so a red detuning of $\Delta_{556} \approx -12\,\Gamma_{556}$ remains within the broadened resonance while providing optimum number of atoms. For the narrow-line green MOT, the Zeeman shift produced by the magnetic field must compensate the laser detuning over a sufficiently large capture volume. At lower gradients, the restoring force is weak and atoms transferred from the blue shell are not efficiently captured. At higher gradients, the Zeeman shift increases rapidly with position, reducing the effective capture volume of the green MOT and thereby decreasing the loading efficiency. The observed optimum at 12 G/cm results from the best compromise between capture efficiency and confinement.

Now, we study the variation of the atom number in the green MOT with various green beam sizes in Fig. 4.9(a). With an increase in the diameter of the green laser beam (ϕ_{G}), the atom number increases and saturates. The saturation point is $\phi_{\mathrm{G}} \approx \phi_{\mathrm{HC}}$. This is

Table 4.1: Number of atoms (N) in the green MOT with various configurations.

	ϕ_{B} (mm)	ϕ_{G} & ϕ_{HC} (mm)	N
Core-shell MOT	18	6	3.4×10^{8}
	18	10	1.0×10^{8}
	30	16	4.5×10^{7}
Center-shifted MOT	9	9	1.9×10^{7}

because in the presence of both blue and green lasers, the cooling is mainly determined by the blue laser, as the blue transition is a stronger transition by two orders of magnitude. Unlike the previous study in Rb, where the weak transition is only 4-5 times weaker, the presence of the weaker transition helps, and the core was overfilled by the weak transition laser [107]. For high power of green laser, such that the power broadened linewidth of weak transition is comparable to the broad transition, we may see the effect of overfilling due to cooling by the green transition.

Further, we study the loading rate of the green MOT for the hollow core and green beam sizes ϕ_{HC} & $\phi_{\text{G}} = 6$ mm and 10 mm with $\phi_{\text{B}} = 18$ mm. The loading rate is determined by turning on the blue and green MOT for a given time (loading time) and determining the number of atoms. The loaded atoms, N_{norm} (normalized with maximum number of atoms) vs loading time (t) is shown in Fig. 4.9(b) by blue solid circle (ϕ_{HC} & $\phi_{\text{G}} =$ 6 mm) and black triangular markers (ϕ_{HC} & $\phi_{\text{G}} =$ 10 mm). The curve is fitted with $N(t) = N_0(1 - e^{-t/t_{\text{L}}})$ and shown in red curve. The loading time (t_{L}) for these two configurations, ϕ_{HC} & $\phi_{\text{G}} = 6$ mm and ϕ_{HC} & $\phi_{\text{G}} = 10$ mm with ϕ_{B} =18 mm, are 0.4 s and 0.6 s respectively.

We further study N with the power of the green MOT and blue MOT lasers, as shown in Fig. 4.10. N versus green MOT laser power (P_{556}) shown in Fig. 4.10(a) shows saturation, suggesting that the available green laser power is sufficient for trapping. In contrast, the N versus blue laser power (P_{399}) curve in Fig. 4.10(b) shows a linear relationship, indicating that increasing the blue MOT laser power continues to increase the number of atoms, indicating higher power is desirable.

In the core-shell configuration, the central core of the blue beam is masked (even though it is redirected for use in 2D cooling), resulting in a limitation of the available blue power for MOT formation. To overcome this limitation and fully utilize the blue MOT beam power, we implement center-shifted dual MOT configuration. In this configuration, the overlap region of the three counter-propagating blue laser beams is shifted towards Zeeman slower,

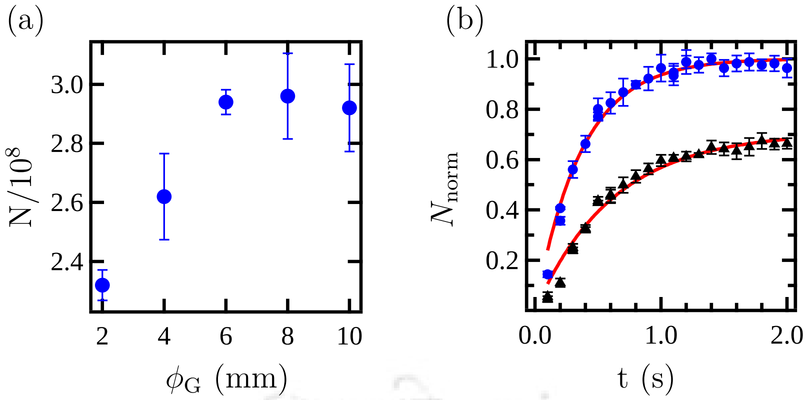

Figure 4.9: (a) Number of atoms (N) in the green MOT vs green beam size (ϕ_G) with $\phi_B = 18$ mm, $\phi_{HC} = 6$ mm, and $\Delta_{556} = -10\Gamma_{556}$. (b) Loading curve with $\phi_B = 18$ mm and $\phi_{HC/G} = 6$ mm (blue circle) and 10 mm (black triangle) with $\Delta_{556} = -10\Gamma_{556}$. The red solid lines are the corresponding exponential fit.

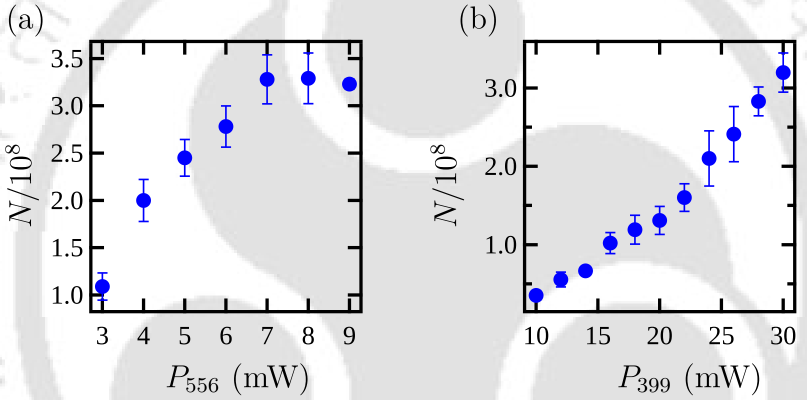

Figure 4.10: Number of atoms (N) in the green MOT vs (a) green beam power (P_{556}) and (b) blue beam power (P_{399}). Experimental parameters: $\Delta_{399} = -2\Gamma_{399}$, $\Delta_{556} = -10\Gamma_{556}$, $\phi_B = 18$ mm and ϕ_{HC} & $\phi_G = 6$ mm.

where the magnetic field is non-zero. The atoms emerging from the Zeeman slower are first pre-cooled and partially trapped in the blue MOT. These atoms subsequently enter the green MOT (zero magnetic field) region and are trapped and cooled further. However, in this method, the maximum number of atoms we loaded in the green MOT is around 2×10^7 atoms, which is one order of magnitude lower than the number of atoms trapped in the core-shell MOT configuration. As shown in the simulations (Fig. 4.7), the separation between the blue and green MOT regions plays a crucial role in determining the capture efficiency. Even a small displacement between the two regions can significantly reduce the number of atoms loaded into the green MOT, which likely explains the lower efficiency observed in the center-shifted configuration. The image of the center-shifted dual MOT is shown in Fig 4.4(d). The non-spherical shape of the center-shifted MOT arises from the displacement of the blue-MOT beams overlap region away from the magnetic-field zero. At this location, the atoms experience a non-zero magnetic field, which modifies the balance of the scattering forces from the counter-propagating beams. As a result, the restoring force becomes asymmetric, leading to an elongated and distorted cloud shape. Although the green MOT is centered at the magnetic-field zero, the loading process is not spatially symmetric, which can result in an elongated cloud shape.

The results presented in this section appear in the following publication: Thilagaraj Ravi, Rajnandan Choudhury Das, Heramb Vivek Bhusane, Samrat Roy, and Kanhaiya Pandey, **"Efficient direct loading of the green MOT of Yb with low green laser power**," *Physics Letters A* **577** (2026), 131429.

4.3 Three-photon Rydberg excitation

Rydberg excitation in Yb atoms plays a crucial role in advancing neutral-atom-based quantum computation and quantum simulation platforms. In Yb, Rydberg excitation can be achieved via two-photon excitation from the excited states 6s6p ^{1}P1 [108], 6s6p ^{3}P1 [93], or from the metastable state 6s6p $^3P_2$ [109]. Among these possible intermediate levels, the one with the smallest natural linewidth is most favorable for achieving coherent Rydberg excitation, as it minimizes spontaneous emission and decoherence [110].

However, the second step in such two-photon schemes typically requires ultraviolet (UV) laser light to couple to the Rydberg state. At these short wavelengths, laser generation becomes technically challenging, since frequency doubling is often the only viable approach. The available output power from such systems is usually limited, which poses a significant challenge because a high laser intensity is required to compensate for the weak dipole matrix element of the Rydberg transition.

An alternative approach is to employ a three-photon excitation scheme, which avoids the need for UV light. In this configuration, the final excitation step usually lies in the infrared (IR) region, where high-power, narrow-linewidth lasers are easier to construct and stabilize. In our work, we implemented this approach and aimed to realize Rydberg excitation in Yb through a three-photon excitation pathway, as illustrated in Fig. 4.11.

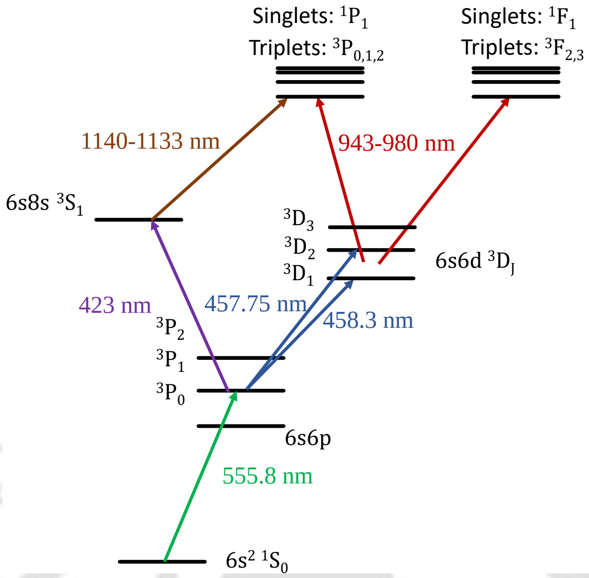

Figure 4.11: Transition pathways for three-photon Rydberg excitations in Yb.

The first excitation pathway we considered was

$$6s^2\ {}^1S_0 \rightarrow 6s6p\ {}^3P_1 \rightarrow \left\{ \begin{matrix} 6s6d\ {}^3D_1 \\ 6s6d\ {}^3D_2 \end{matrix} \right\} \rightarrow \left\{ \begin{matrix} 6snp\ {}^3P_0 \\ 6snp\ {}^3P_1 \\ 6snp\ {}^3P_2 \\ 6snf\ {}^3F_2 \\ 6snf\ {}^3F_3 \\ 6snp\ {}^1P_1 \\ 6snf\ {}^1F_3 \end{matrix} \right.$$

This pathway is particularly advantageous because it provides access to both P and F Rydberg states, allowing exploration of a broader range of angular momentum levels. Different angular momentum states possess different interaction properties and selection rules, enabling greater flexibility for spectroscopy and quantum-control applications. To investigate this excitation route, laser systems operating at 556 nm, 457 nm, and 940–980 nm were required. The 556 nm light corresponds to the intercombination transition used for initial excitation, while the 457 nm and near-IR lasers couple to higher excited and Rydberg levels, respectively.

We constructed external cavity diode lasers (ECDLs) designed to operate near 457 nm and 960 nm using commercially available laser diodes. However, despite extensive optimization efforts—including adjustments of the grating alignment, cavity length, and diode temperature—we were unable to achieve stable single-mode lasing at the target wavelength of 457 nm. This difficulty was primarily due to the limited tunability and mode-hop-free range of available blue diodes. As a result, this excitation pathway was not pursued further in our experiment.

The alternate excitation pathway that we pursued is given by

$$6s^2\ {}^1S_0 \rightarrow 6s6p\ {}^3P_1 \rightarrow 6s8s\ {}^3S_1 \rightarrow \begin{cases} 6snp\ {}^3P_0 \\ 6snp\ {}^3P_1 \\ 6snp\ {}^3P_2 \\ 6snp\ {}^1P_1 \end{cases}$$

This excitation route was feasible for us because the corresponding laser systems operating at 556 nm, 423 nm, and 1137 nm were already available in our setup. The 556 nm laser system is generated by frequency doubling of a 1112 nm fundamental laser, while both the 423 nm and 1137 nm lasers are home-built external cavity diode lasers (ECDLs) designed for narrow-linewidth operation and wide tunability across the desired transitions.

We therefore proceeded with this excitation scheme involving the 423 nm and 1137 nm transitions, which provide access to the desired np Rydberg states. The initial experiments were carried out using thermal Yb atoms in the spectroscopy chamber. Although this configuration allowed convenient optical alignment, no measurable Rydberg excitation signal was detected. The absence of a signal was likely due to Doppler broadening of the optical transitions and the low excitation probability at room temperature, both of which reduce the efficiency of population transfer to the Rydberg states.

To overcome these limitations, we subsequently conducted the experiment using atoms in the blue MOT, where the atoms are laser-cooled and trapped. The reduced temperature and confinement in the MOT considerably minimize Doppler effects and provide better control over the spatial overlap of the excitation beams. However, a clear Rydberg excitation signal was still not observed.

This was most likely because the atoms decayed into metastable states from the intermediate level 6s8s $^3S_1$. To avoid this problem, it is important to use repumping lasers at 770 nm and 649 nm to bring the atoms back from the metastable states to the main cooling cycle. At that time, we could not use these repumping lasers because we did not have enough laser controllers to operate all the required lasers. We have now procured additional controllers, which will allow us to include the repumping beams in future experiments.

We are now working on improving the frequency stability and narrowing the linewidth of the 1137 nm laser, and also on fine-tuning the beam alignment and detection setup. With these upgrades, we expect to finally achieve efficient three-photon excitation to the Rydberg states in our upcoming experiments.

4.4 Summary

In summary, we successfully loaded approximately 5×10^8 atoms at a temperature of around 11 mK. Further, we also demonstrated the loading of the green MOT at narrow-linewidth green transition using both core-shell and center-shifted dual MOT configurations with limited green laser power of approximately 10 mW. In the core-shell configuration, the green beam is superimposed onto a central hole within the core of the blue beam. Additionally, the center-shifted MOT configuration was implemented, allowing the entire power of the blue beam to be utilized in the MOT without any loss. However, the core-shell configuration was able to trap a higher number of atoms, with 3.4×10^8 atoms compared to 2×10^7 atoms in the center-shifted MOT configuration. This study will be useful for portable optical clocks using Yb and also for quantum computation using Yb tweezer arrays. Alongside the MOT work, we also explored three-photon Rydberg excitation in Yb atoms using our existing laser systems at 556 nm, 423 nm, and 1137 nm. Although we have not yet observed a clear Rydberg signal, our ongoing efforts are focused on improving the setup to achieve efficient Rydberg excitation in future experiments.

5

Microscopic Optical Dipole Trap of Rb Atoms

Contents

5.1 Introduction

The ability to trap and manipulate a single neutral atom marks a major milestone in the development of quantum optics and quantum technology. A single atom confined in a microscopic potential serves as a fundamental building block for quantum simulation and computation, enabling precise control of quantum states and interactions at the individual particle level. Several experimental techniques have been developed to realize such trapping, among which optical dipole traps have proven particularly powerful and versatile. These traps exploit the dipole force arising from the interaction between an atom and an off-resonant light field, enabling confinement at the focus of a tightly focused laser beam. Under suitable loading conditions, an optical dipole trap can operate in the collisional blockade regime, where at most one atom remains trapped. In this regime, light-assisted collisions rapidly remove pairs of atoms, resulting in a sub-Poissonian atom number distribution with only zero- or one-atom occupancy. This phenomenon, first demonstrated by the Grangier group [73, 111], represents a crucial step toward deterministic single-atom control and provides the foundation for scalable neutral-atom quantum technologies. Following this breakthrough, significant progress has been made toward creating arrays of individually trapped atoms, where each trapping site is occupied by a single atom. Such defect-free arrays form the basis for scalable quantum registers, enabling the realization of logical qubits with high fidelity. These systems provide a versatile platform for implementing quantum gates, performing quantum simulations of complex many-body systems, and exploring phenomena such as entanglement and quantum phase transitions with unprecedented control and precision.

In this chapter, we describe the experimental realization of a single rubidium (Rb) atom in an optical dipole trap. The chapter begins with an overview of the experimental setup, including the vacuum chamber, magnetic field coils, and laser systems, along with their frequency stabilization schemes. We then discuss the Doppler and sub-Doppler cooling techniques implemented to prepare atoms at micro-kelvin temperatures. Finally, we present the design and implementation of the microscopic optical dipole trap and the experimental results demonstrating single-atom trapping.

5.2 Experimental setup

In this section, we describe the experimental setup developed for the cooling and trapping of ^{87}Rb atoms. The setup consists of several essential subsystems, including the vacuum chamber, laser systems for cooling and repumping, and frequency stabilization. The vacuum system provides a low-pressure environment necessary to achieve long trap lifetimes by minimizing collisions with background atoms. The laser system generates the required frequencies for the magneto-optical trap (MOT), optical molasses, and optical dipole trap (ODT). Further, frequency stabilization techniques are implemented to ensure stable and tunable laser detuning from the atomic resonance.

5.2.1 Vacuum system

The vacuum system designed for cooling and trapping ^{87}Rb atoms is a compact and straightforward setup. Unlike the Yb system, it does not incorporate complex technical

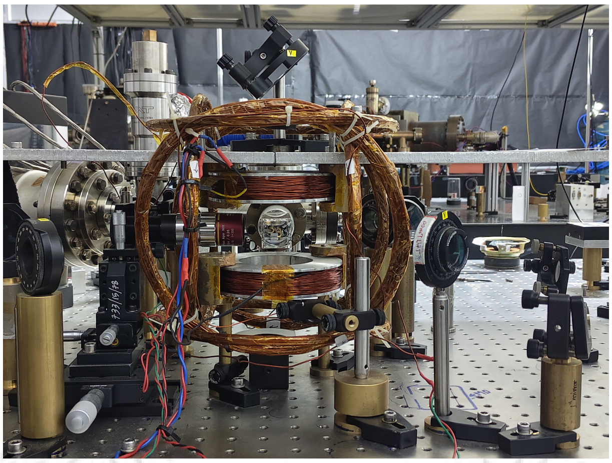

Figure 5.1: Rb MOT setup.

.

components such as two-dimensional cooling stage or a Zeeman slower. Instead, the MOT is directly loaded from a Rb dispenser. We upgraded our previous vacuum system (details can be found in Ref. [58]) by introducing a few modifications to make it suitable for ODT experiments. The upgraded vacuum system is shown in Fig. 5.2. In the earlier setup, the ion pump was attached very close to the MOT glass chamber, which introduced unwanted stray magnetic fields and restricted the available space for mounting optics near the chamber. To address this issue, the ion pump was repositioned at an angle and connected using an extended-length adapter to minimize its influence. Additionally, a viewport (VPZ38LABBAR-LN, Torr Scientific), AR coated for 375 nm to 866 nm, was installed along the longitudinal axis of the glass chamber that allows us to send laser beams or image the atoms in that direction as well. The MOT chamber is made of Pyrex glass with dimensions 75 mm × 28 mm × 28 mm with a wall thickness of 2.5 mm. The Rb atoms are sourced from a commercial dispenser (AlfaVakuo e.U, AS-Rb-0090-2C), which contains 90 mg of Rb in the form of a RbBi40 alloy. The dispenser is made of a cylindrical metallic tube that acts as a resistive heating element and encloses the alloy material. When current is passed through the dispenser, it heats up and releases Rb vapor into the vacuum chamber. The dispenser is positioned close to the MOT glass chamber and electrically connected through a two-pin feedthrough for current supply. The entire vacuum system was baked for approximately two weeks to remove adsorbed gases and achieve ultra-high vacuum conditions. The final base pressure achieved is below 5×10^{-11} mbar when the dispenser is turned off, and 2×10^{-10} mbar when the dispenser current is 2 A.

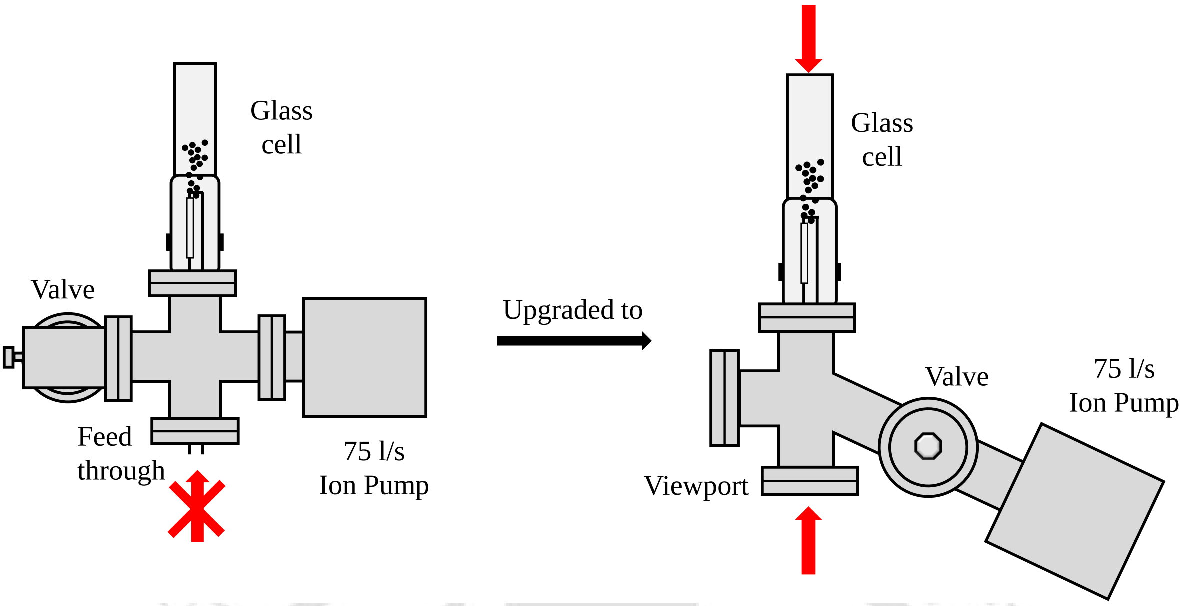

Figure 5.2: Overview of upgraded vacuum system.

.

5.2.2 Magnetic field coils

The magnetic field required for the MOT is generated by a pair of anti-Helmholtz coils wound with copper wire on an aluminium frame. The aluminium frame has a 2-mm-wide slit to minimize eddy currents induced during fast switching of the magnetic field. Each coil has an inner diameter of 72 mm and an outer diameter of 130 mm, and consists of 600 turns of copper wire with a diameter of 1.5 mm. This coil configuration produces a magnetic field gradient of approximately 18 G/cm per ampere of coil current.

Three pairs of 230 mm diameter coils are arranged in a Helmholtz configuration to cancel stray magnetic fields and to apply a bias field. Each pair can generate a magnetic field of $\approx$ 2 G/A. The coils are shown in Fig. 5.1.

5.2.3 Laser system and stabilization

For trapping and cooling of Rb atoms in MOT, we utilized D2 line transition $5S_{1/2}$, $F = 2 \rightarrow 5P_{3/2}$, $F = 3$ for cooling and $5S_{1/2}$, $F = 1 \rightarrow 5P_{3/2}$, $F = 1$ for repumping, as shown in Fig. 5.3. We need two main lasers at 780 nm that are crucial for cooling and repumping. Many of the lasers used in the Rb experiment are home-built external cavity diode lasers (ECDL), which operate in Littrow configuration with a reflective holographic grating,

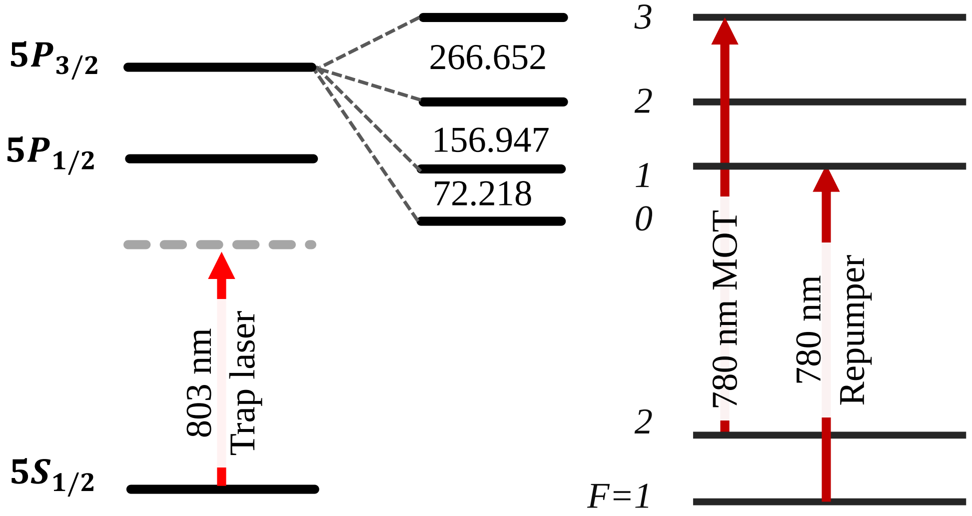

Figure 5.3: Energy-level diagram of ^{87}Rb showing the optical transitions used in the experiment. The 780 nm cooling and repumper lasers drive the $5S_{1/2} \rightarrow 5P_{3/2}$ transitions for magneto-optical trapping, while the 803 nm laser is used for the optical dipole trap. Hyperfine splittings of the relevant excited states are also indicated.

except the dipole trap laser, which is only a free-running diode laser.

MOT laser system and spectroscopy In the earlier stage of the experiments, our MOT laser was a single ECDL laser at 780 nm, made of a laser diode (Model: L785H1, Make: Thorlabs) of output power 120 mW stabilized using frequency modulation spectroscopy. However, in order to implement the molasses stage and to image the atoms trapped in ODT, the frequency tuning of the laser should be wider, by at least around 100 MHz. It is not possible with only AOM frequency tuning (used on the path of the spectroscopy arm). Therefore, we implemented the beat-locking scheme, similar to that described in [112], which consists of two home-built ECDLs as shown in Fig. 5.4, a reference (ECDL1) and a main laser (ECDL2). The reference laser is a low-power laser (Model: L785P090, Make: Thorlabs), which is frequency-stabilized to the $5S_{1/2}$, $F = 2 \rightarrow 5P_{3/2}$, $F = 1,3$ crossover peak using polarization spectroscopy. This laser frequency serves as a reference to the main laser. The main laser is (Model: L785H1, Make: Thorlabs), capable of delivering an output of 120 mW power, whose frequency is offset-locked relative to the reference laser frequency. The optical setup for the beat-locking system is shown in Fig. 5.4. A small fraction of light from both lasers is combined using a non-polarizing beam splitter and sent to a high-bandwidth fast photodetector (PD) (Model: APD430A2/M, Make: Thorlabs), which detects the beat signal between the two lasers.

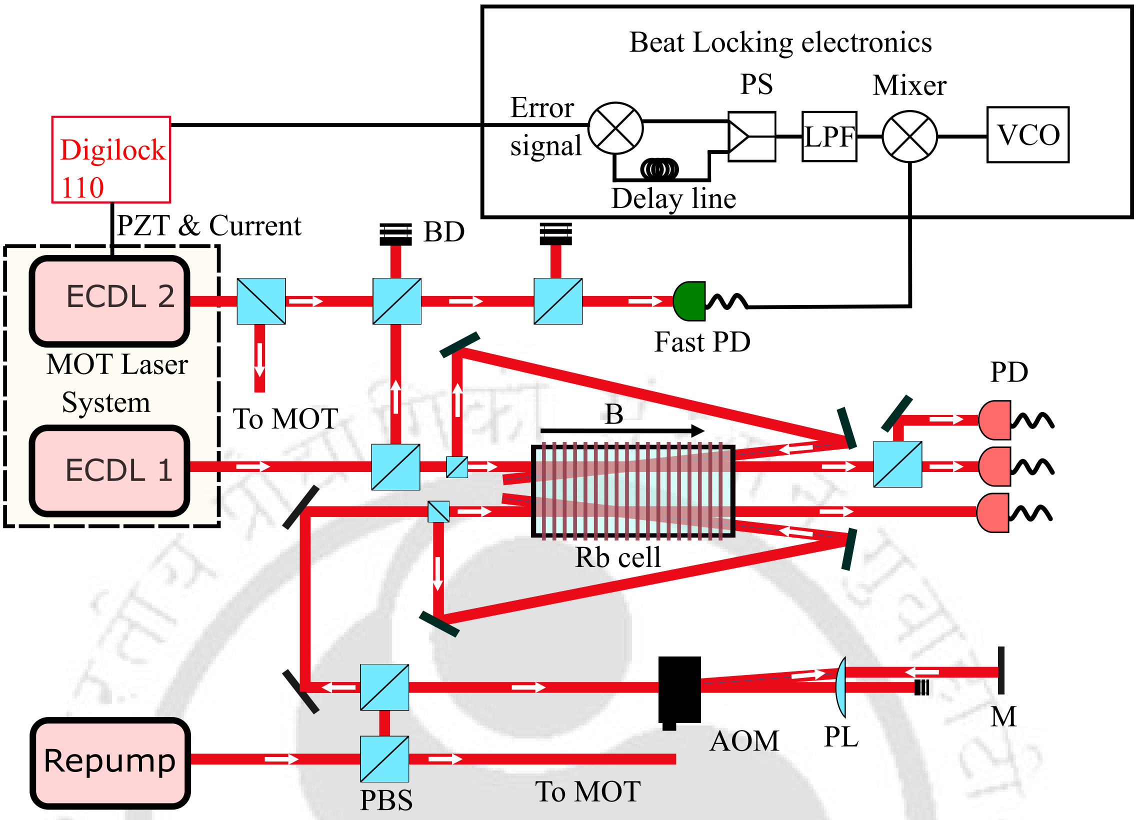

Figure 5.4: The schematic overview of the spectroscopy setup of MOT and repumper laser systems.

This beat frequency corresponds to the frequency difference between the lasers. The signal from the PD is sent to an electronic feedback circuit that generates an error signal. The corresponding electronics configuration [112] is shown in Fig. 5.4. The beat signal from the PD is mixed with the reference signal of the voltage-controlled local oscillator (VCO) (Model: ZOS-150, Make: Mini-circuits) using a mixer (Model: ZEM-M2TMH+, Make: Mini-circuits). The mixed signal is sent to a power splitter (PS) (Model: ZSC-2-1+, Make: Mini-circuits) through a low-pass filter (LPF) (Model: BLP-30+, Make: Mini-circuits) to divide into two portions. The split signals are mixed again using another mixer (Model: ZAD-1-1+, Make: Mini-circuits), after introducing a phase delay (using a 10 m coaxial BNC cable) in one of them. The output of the mixer is used as an error signal, as shown in Fig. 5.5(b), and is fed to a Digilock (Model: Digilock 110, Make: Toptica) to actively stabilize the frequency of the main laser through two PID controllers, one for the current and one for the piezo. This setup allows us to precisely control the detuning of the MOT laser frequency from the atomic resonance by adjusting the local VCO frequency. The relation between the local VCO frequency and the beat frequency of the main and reference lasers is shown in Fig. 5.5(c), when the main laser is locked to the lock point of the error signal shown in Fig. 5.5(b). We observed that the frequency of the main laser

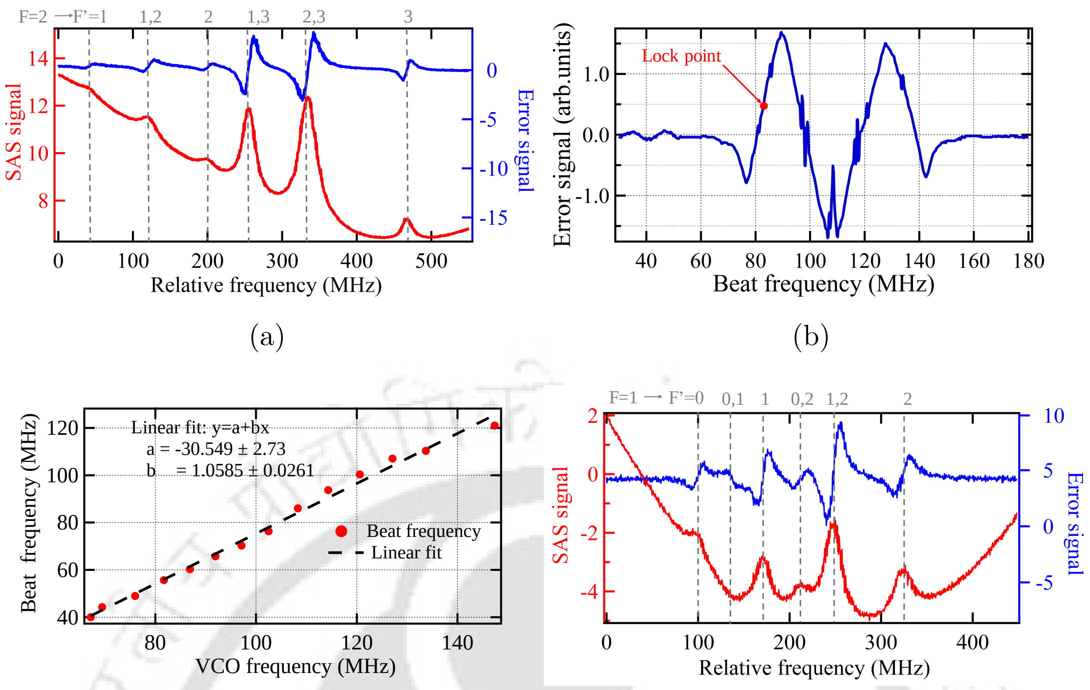

(a) (b)

(c) (d)

Figure 5.5: (a) The MOT spectrum (red line) and error signal (blue line) for the transition $5S_{1/2}$, $F = 2 \rightarrow 5P_{3/2}$, $F = \mathrm{X}$ obtained with ECDL 1, (b) The error signal generated using beat locking mechanism for the MOT ECDL 2, (c) The relation between the local VCO and the beat frequency between ECDL 1 and ECDL 2, and (d) The repumper spectrum (red line) and error signal (blue line) for the transition $5S_{1/2}$, $F = 1 \rightarrow 5P_{3/2}$, $F = \mathrm{X}$.

relative to the reference can be varied to a wide range (in discrete steps) within a total duration as short as 10 ms, without unlocking the laser.

Repumper laser system The repumper laser is an ECDL identical to the main laser of the MOT laser system. The role of the repumper is to re-excite atoms that decay off-resonantly from the state $5P_{3/2}$, $F = 3$ to the ground state $5S_{1/2}$, $F = 1$ hyperfine level. Without the repumper, atoms accumulating in $5S_{1/2}$, $F = 1$ state would no longer interact with the cooling light, which leads to a loss of atoms from the cooling cycle. The repumper thus ensures that atoms remain within the closed optical cycle required for efficient laser cooling. The repumper is stabilized to $5S_{1/2}$, $F = 1 \rightarrow 5P_{3/2}$, $F = 1$ transition using frequency modulation spectroscopy. The spectroscopy setup is shown in Fig. 5.4. The small portion of the beam is up-shifted by 2×40 MHz using an AOM in double pass configuration, and then it is split into two parts as probe and coupling beams.

The same AOM is used to modulate the laser frequency at 50 kHz. We use the Digilock module for modulation and generating the error signal. The absorption spectrum and the error signal of the repumper laser are shown in Fig. 5.5(d).

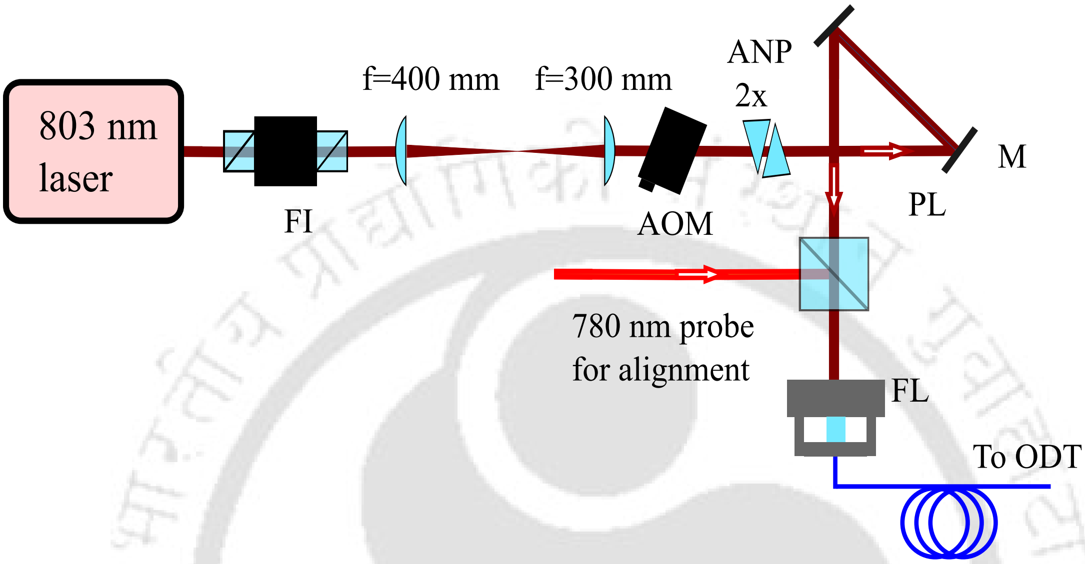

Figure 5.6: Dipole trap laser system at 803 nm.

Dipole trap laser The schematic overview of the dipole trap laser system is shown in Fig. 5.6. The trap laser is a diode laser (Model: LD808–SE500, Make: Thorlabs) that delivers up to 300 mW of output power at a wavelength around 803 nm. According to the manufacturer, the diode is highly sensitive to back reflections, and even 2% back reflection can cause permanent damage. The laser is relatively narrow in frequency and does not require additional frequency stabilization for our application. Therefore, we operate it as a free-running diode without an external cavity (grating) setup. During the initial characterization of the LD, we observed that the diode emits unpolarized light over a narrow range of operating currents. Outside this range, the polarization is stable, and the laser performs reliably. The output beam has an elliptical profile of size approximately 2 × 4 mm. An optical isolator is placed immediately after the laser to block back reflections from downstream optics. After the isolator, a telescope (f = 400 mm and f = 200 mm) reduces the beam diameter by a factor of two. The beam then passes through an acousto-optic modulator (AOM) for fast switching of the trap. An anamorphic prism pair (ANP-2×) follows the AOM to convert the elliptical beam into a near-circular profile for efficient fiber-coupling. The trap beam is then mixed with the 780 nm resonance beam for the initial alignment of ODT. Both beams are coupled into a single-mode fiber using a fiber launch system.

5.3 Magneto-optical trap

The first important step for any cold atom technology is to laser cool and trap the atoms in magneto-optical trap (MOT) using three pairs of counterpropagating σ^+-σ^- laser beams. As discussed earlier, we need to have two sets of lasers, one for cooling, addressing the transition $5S_{1/2}$, $F = 2 \to 5P_{3/2}$, $F = 3$, and another for repumping, addressing the transition $5S_{1/2}$, $F = 1 \to 5P_{3/2}$, $F = 1$. The most commonly used repumping path is $5S_{1/2}$, $F = 1 \to 5P_{3/2}$, $F = 2$. We opted for the transition $F = 1$ to $F' = 1$ because the blue detuned repumper laser addressing this transition also assists in cooling as well as repumping [113]. The complete optics layout for the MOT setup is shown in Fig. 5.7. The cooling and repumping beams first pass through acousto-optic modulators (AOMs) operating at +120 MHz and +100 MHz, respectively. These AOMs are used for fast switching and power control of the laser beams. The first order of the cooling and repumping AOMs are mixed and the elliptical beam profile is then converted into a circular shape using a pair of cylindrical lenses with focal lengths of 150 mm and 75 mm to improve fiber coupling efficiency. After beam shaping, the cooling and repumping beams are coupled into a polarization-maintaining single-mode optical fiber to deliver it to the MOT setup. After the fiber collimator, the beam is expanded to a diameter of 18 mm, and it is split into 6 beams using PBSs and half-wave plates, which helps us to balance the intensity of the MOT arms. The beams are directed over a free-space path of approximately 1 m to the MOT glass cell, and their polarization is converted from linear to σ^+/σ^- using quarter-wave plates. The optical power in each arm is approximately 2 mW for the cooling beam and 1 mW for the repumper. The cooling beam is detuned by -12 MHz from the transition $5S_{1/2}$, $F = 2 \to 5P_{3/2}$, $F = 3$ and the repumping beam is detuned by +20 MHz from the transition $5S_{1/2}$, $F = 1 \to 5P_{3/2}$, $F = 1$. The MOT is directly loaded from the background vapor produced by the Rb dispenser operating at 2 A current, and the magnetic field gradient applied during loading is 18 G/cm. The temperature is measured with the time-of-flight (TOF) method using absorption imaging [59]. A weak probe beam addressing the transition $5S_{1/2}$, $F = 2 \to 5P_{3/2}$, $F = 3$ detuned by 4 MHz is used for absorption imaging. The absorption images of the cloud were taken after two different free-expansion times. The temporal evolution of the cloud size during TOF expansion is given by

$$\sigma^2(t) = \sigma_0^2 + \frac{k_B T}{m_{\mathrm{Rb}}} t^2, \tag{5.3.1}$$

where $\sigma(t)$ is the Gaussian root-mean-square (rms) radius of the atomic cloud after an expansion time t, σ_0 is the initial cloud radius in the trap, k_B is the Boltzmann constant, T is the temperature of the atomic ensemble, and m_{Rb} is the mass of a Rb atom. Using this

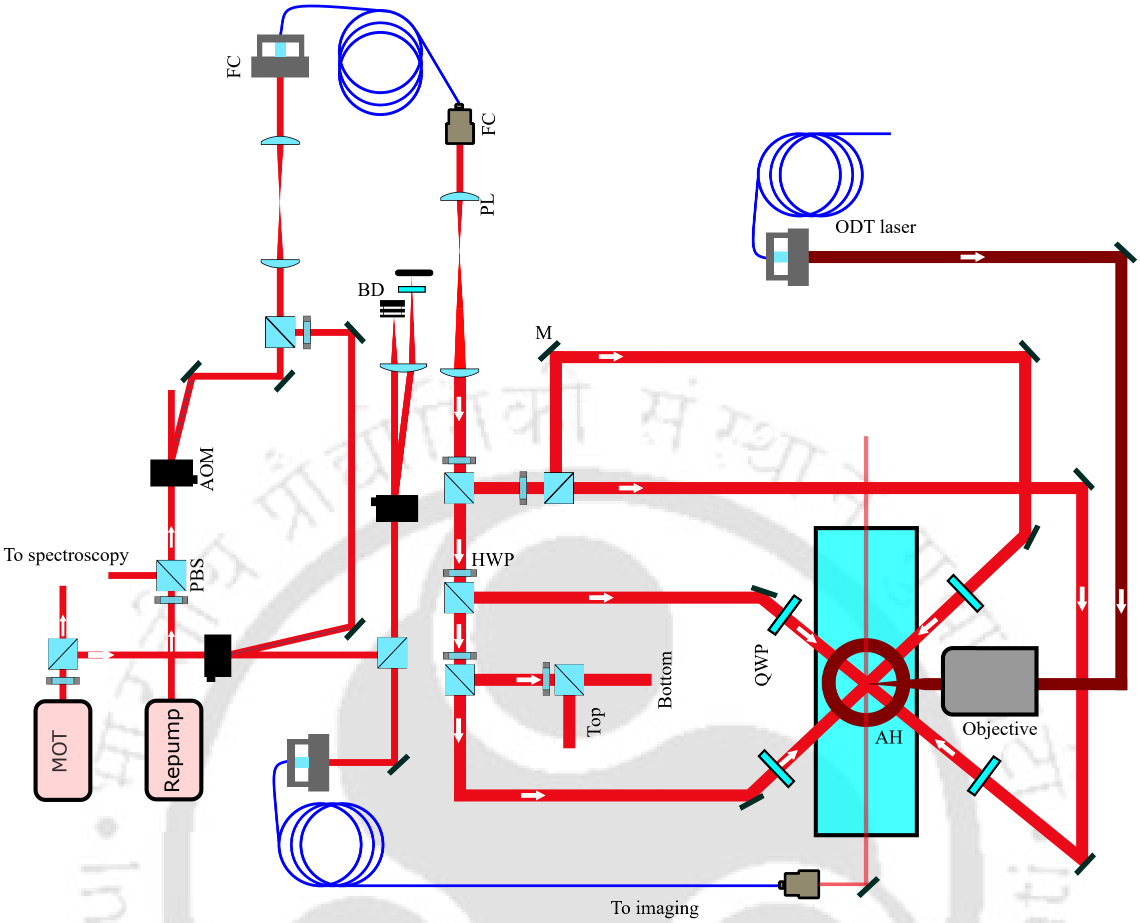

Figure 5.7: Schematic overview of the MOT optics arrangement.

equation, one can find out the temperature of the MOT cloud. The minimum temperature of the cloud observed is around 180 μK.

5.4 Sub-Doppler cooling

We employed sub-Doppler cooling using σ^+-σ^- molasses beams to reduce the atomic cloud temperature below the Doppler limit. In order to implement sub-Doppler cooling, the magnetic field needs to be extinguished completely. Even small stray magnetic fields affect its cooling efficiency. The residual magnetic field was compensated by applying controlled magnetic fields along all three axes using shim coils. The initial nullification was performed by measuring the magnetic field with a Gauss meter near the glass chamber and applying appropriate compensating fields using the shim coils. Fine adjustment was then carried out by optimizing the cloud temperature. The atomic cloud temperature versus the shim coil magnetic field is shown in Fig. 5.8. Sub-Doppler cooling is effective

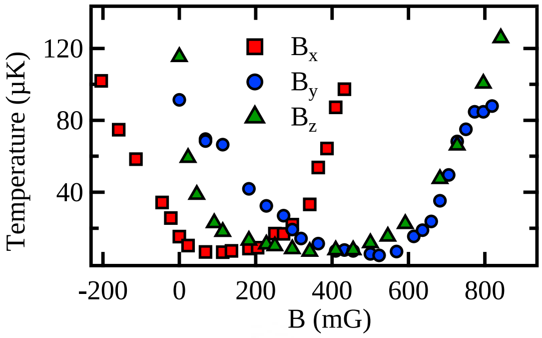

Figure 5.8: Temperature of the cloud vs magnetic field applied along all three directions using the shim coil.

for the magnetic field span around 200 mG. Beyond that, it becomes ineffective, and the temperature starts increasing. Next, the laser frequency needs to be further red-detuned by at least 40–60 MHz to reach a lower temperature of about 10 μK. Before the beat locking scheme was implemented in our lab, our only available option was to introduce an additional AOM in the path of the zeroth-order beam from the AOM whose first-order output was already being used for the MOT beams. The molasses beams were turned on when the MOT AOM was switched off. This approach allowed us to achieve the frequency shift of -60 MHz for the molasses phase without interfering with the MOT beam configuration. In this configuration, we observed that sub-Doppler cooling was not effective when the molasses phase was activated immediately after switching off the magnetic field and MOT beams. The atomic cloud temperature remained high at around 200 μK. This may be due to the magnetic field not being completely extinguished when the molasses beams, detuned by 60 MHz, were turned on immediately. The residual magnetic field can disrupt the sub-Doppler cooling, leading to less efficient temperature reduction. The issue was resolved by introducing a short delay between turning off the magnetic field and switching off the MOT beams. A delay of a few milliseconds was sufficient to allow the magnetic field to decay completely. After this delay, the MOT beams were switched off, and the molasses beams were turned on immediately for a duration of 5 ms. The minimum temperature of below 10 μK was obtained when the delay time was 7 ms. The dependence of temperature with delay time and the molasses duration is shown in Fig. 5.9(a) and (b), respectively. A molasses duration of 5 ms was found to be sufficient to reach the minimum temperature. To confirm the temperature further, the Gaussian radius $\sigma(t)$ of the cloud was measured for different expansion times, and the values of $\sigma^2(t)$ were plotted as a function of t^2 as shown in Fig. 5.9(c). The data were fitted with a straight line based on Eq. 5.3.1, from which the temperature was extracted from the slope. The temperature of the atomic cloud was found to be 7.77 ±0.11 μK.

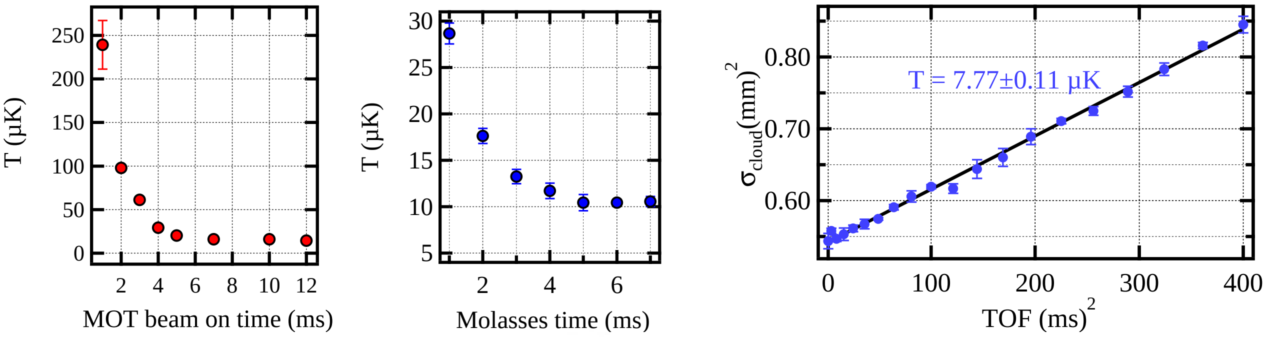

(a) (b) (c)

Figure 5.9: Temperature measurements during the optical molasses stage. (a) Temperature as a function of MOT beam on-time with molasses phase of 5 ms. (b) Temperature as a function of molasses duration with MOT beam on time of 7 ms, showing cooling to a minimum temperature of approximately 8 μK. (c) Mean-square cloud size, σ^2_{cloud}, as a function of time of flight. A linear fit yields a temperature of 7.77 ± 0.11 μK. Error bars represent the standard deviation obtained from repeated measurements.

In the later stage of the experiment, we implemented a beat-lock scheme to achieve a large frequency shift, which allowed the MOT beams to be used as molasses beams by changing the laser frequency. However, the minimum time required to apply a frequency shift of 60–70 MHz is about 10 ms. This delay limits fast switching between the MOT and molasses phases. The response time can be improved by applying fast frequency feedback to the laser current through a bias tee.

5.5 Optical dipole trap

In this section, we discuss optical dipole trapping of Rb atoms. We begin with the experimental setup for the optical dipole trap and the loading of atoms into traps with different spot sizes. Finally, we discuss single-atom trapping of Rb atoms.

5.5.1 Experimental setup

Our trapping laser operates at a wavelength of 803 nm. Since this wavelength lies close to the D_1 transition (≈795 nm) of Rb, it also induces Raman scattering, which leads to heating of the trapped atoms and consequently reduces the lifetime of the ODT. However, this wavelength allows us to achieve a higher trap depth with relatively low optical power. We therefore proceeded with the 803 nm laser for the initial trapping experiments.

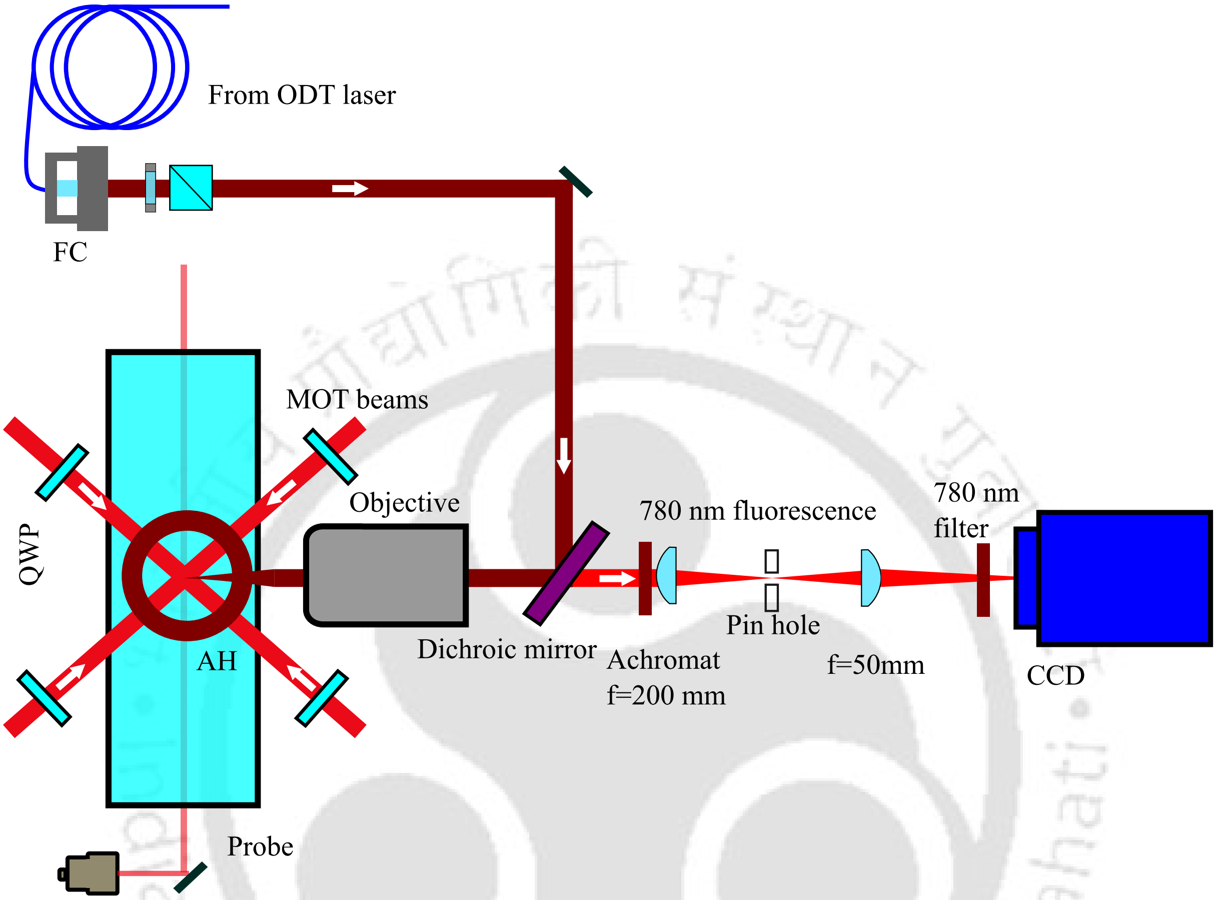

Figure 5.10: Schematic overview of the ODT setup and imaging setup.

The schematic overview of the ODT setup is shown in Fig. 5.10. The output beam from the fiber is collimated to the desired diameter to obtain the required ODT spot size, and we were able to achieve around 100 mW of power after the collimator. Following the fiber collimator, the beam passed through a wave plate and PBS combination to ensure well-defined linear polarization. This arrangement compensated for polarization rotation introduced by the optical fiber over extended operation periods. We use an objective lens (Model: MY10X-823, Make: Mitutoyo) with a numerical aperture of 0.26 and a working distance of 31 mm to create the ODT spot and to collect the emitted fluorescence from the trapped atoms. While selecting the objective lens, several factors must be considered, primarily the numerical aperture (NA) and the working distance.

The NA determines the light-collection efficiency of the objective. The collection efficiency can be estimated by calculating the fraction of the solid angle subtended by the collection cone with respect to the total emission solid angle of an isotropic source, which is 4π. Mathematically, the collection efficiency can be expressed as

$$\eta = \frac{1-\cos\theta}{2}, \tag{5.5.1}$$

where θ is the half-angle corresponding to the numerical aperture, related through NA $= n\sin\theta$. A higher NA indicates that the lens can collect more light from an isotropic point source. A higher NA is desirable to collect a larger fraction of light from a single atom. For example, the collection efficiency of the objective lens of NA=0.5 is 6.7% while 1.7% for NA=0.26. However, lenses with higher NA generally have shorter working distances or focal lengths, which impose constraints on the experimental design. To overcome this limitation, one can use either an in-vacuum objective lens or a custom-designed long working distance objective. In the case of the in-vacuum lens setup, special care must be taken to accommodate the MOT beam geometry, and the alignment becomes more challenging since the lens has to be positioned very close to the MOT cloud. Although a custom-designed objective lens is desirable, it is a considerably more expensive option. An important factor to consider when using an outside-vacuum objective lens is the thickness correction factor. As the emitted light passes from the vacuum into the glass window of the chamber, refraction at the interface causes the rays to bend and deviate from their ideal path. To compensate for this issue, it is better to use desired thickness corrected objectives. Although our current objective is not thickness-corrected, we proceeded with it for the initial setup of the ODT experiments. Moreover, since the numerical aperture (NA) is relatively low (0.26), this limitation is not a significant concern at the present stage.

The objective lens is housed in a kinematic mount and mounted on a three-axis translation stage to achieve precise adjustment of the focal point. The same objective lens is used to collect the fluorescence emitted from the trapped atoms, as shown in Fig. 5.10. The collected fluorescence is separated from the ODT laser using a dichroic mirror (DMSP805L, Thorlabs). After the dichroic mirror, an achromatic lens with a focal length of 200 mm focuses the fluorescence onto an intermediate image plane. The achromatic lens is mounted on the translational stage for fine adjustment of the focus. A pinhole is positioned at this intermediate plane to block unwanted scattered light from the MOT and repumper lasers. A second lens with a focal length of 50 mm forms the final image on the camera. The final magnification of this setup is 12.5. Three 780 nm bandpass filters are used in front of the camera to transmit only the 780 nm fluorescence. The overall collection efficiency of the imaging system is about 0.8% after accounting for all optical losses.

We performed the ODT with three different beam waists of 7.5 μm, 4.5 μm, and 1.6 μm. The beam waists were estimated using the Gaussian beam propagation formula from the measured input beam parameters.

Two types of cameras were used for the ODT experiments. A CMOS camera was used for traps with beam waists of 7.5 μm and 4.5 μm. A CCD camera was used for the trap with 1.6 μm beam waist. The quantum efficiency of the CMOS camera at 780 nm is about 40 %, and the read noise is 7 e^-. It provides a fast frame rate and enables real-time alignment. It can be used for experiments that require shorter readout times. For comparison, the CCD camera has a similar quantum efficiency of 40 % but a lower read noise of 2.6 e^-. The photon count to ADC conversion factor is available for the CCD camera. This information is useful for estimating the number of atoms from the recorded pixel intensity.

CMOS and CCD cameras are less sensitive than electron-multiplying CCD (EMCCD) cameras or single-photon detectors and are therefore not adequate for single-atom detection at the present stage of the experiment. Nevertheless, these cameras were used during the initial phase of the work. At this stage, the primary objective was limited to the construction and characterization of the optical dipole trap (ODT) setup, rather than achieving single-atom detection efficiency. Accordingly, the current ODT system was developed using available resources to gain practical experience in system alignment, imaging optimization, and data acquisition. This experience provides an essential foundation for future developments aimed at single-atom trapping and the realization of single-atom optical tweezer arrays.

5.5.2 Loading of ODT

Initially, we attempted to load the atoms directly into the ODT with a beam waist of 1.6 μm. The attempt did not result in any observable trapping. The small trap volume at this beam waist was likely the reason for not detecting the ODT. In addition, our imaging system was not optimized to detect fluorescence from such a small trap volume. To understand the loading behavior better, we began with a larger beam waist around $\approx$7.5 μm to increase the trap volume, which helped in capturing more atoms at the initial stage. After confirming successful loading, the beam waist was gradually reduced to achieve a tighter confinement suitable for single-atom trapping.

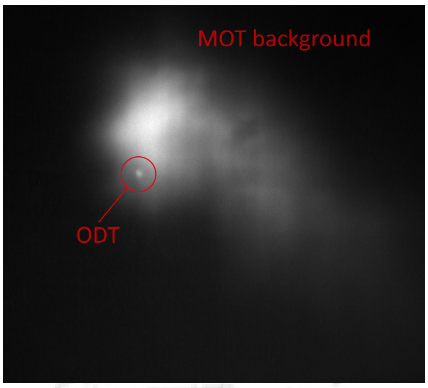

Figure 5.11: The optical dipole trap in the continuous MOT.

.

A larger trap at 7.5 μm beam waist The ODT with a beam waist of 7.5 μm is easier to operate because of its larger trap volume, which improves the loading efficiency. The trapping beam power was ≈45 mW on the atoms, corresponding to a calculated trap depth of about 1.0 mK.

It is important to make sure that the trapping beam is focused at the center of the MOT for proper loading of the atoms into the ODT. Since the trap wavelength is 803 nm, it is also difficult to determine whether the trapping beam is going through the MOT or not. Therefore, the initial alignment of the trapping beam was performed with the help of a 780 nm resonance beam co-propagating (by coupling both beams with the same fiber) with the trapping beam, as shown in Fig. 5.6. Co-propagation of these two beams ensured that they shared the same optical path through the optical elements and the glass cell. The diameter of the trapping beam before the objective is around 1.4 mm, which gives the ODT beam waist of ≈ 7.5 μm. The first step in the alignment was to verify that the ODT beam is intersecting the MOT region. To confirm this, the 780 nm resonance beam (co-propagating with the trapping laser) was directed onto the MOT. The MOT was immediately disrupted and destroyed, which confirmed that the resonance beam (trapping beam) intersected the atomic cloud. The objective lens was then mounted, and the 780 nm beam was focused at the MOT center. When the focused beam was applied, the atoms were pushed out of the trapping region. This confirmed that the trapping beam was properly aligned through the center of the MOT.

After aligning the trapping beam, the imaging system was aligned to detect the fluorescence from the trapped atoms. Detecting fluorescence from atoms in the ODT is more challenging because of the smaller trap volume and reduced photon scattering rate. Therefore, we used the focused 780 nm beam by shining it onto the MOT. The resulting

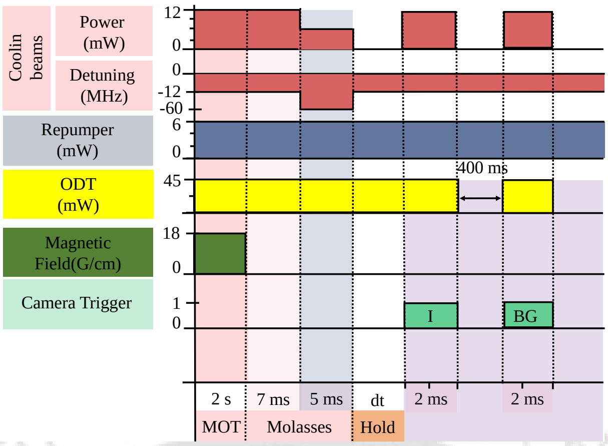

Figure 5.12: Time sequence for measuring the ODT lifetime for the trap waist of 7.5 μm.

fluorescence spot was monitored on the CMOS camera, and the pixel area of the fluorescence spot was marked on the camera. To locate the ODT at the marked area on the camera, the trap was first loaded from the MOT under a strong loading regime. In this stage, the MOT beam power was reduced to lower the MOT temperature. As a result, only the colder atoms were confined near the ODT, and this improved the ODT loading efficiency. Under the strong loading conditions, the ODT appeared as a bright localized spot on the camera, as shown in Fig. 5.11. The ODT loaded from a continuously operated MOT confirmed successful alignment and fluorescence collection through the objective lens. A CMOS camera was used during this procedure because of its high frame rate and fast readout, which allowed real-time observation of the alignment.

Following the completion of the alignment, we proceeded to the loading and lifetime measurement of the ODT. The complete experimental sequence for loading and lifetime measurement of the ODT is shown in Fig. 5.12. The MOT was loaded for 2 s with a cooling beam detuning of -12 MHz and a magnetic field gradient of about 18 G/cm. The repumper remained on throughout this period to maintain the population balance. The ODT beam was also on during this phase, which allowed continuous loading of atoms into the trap during the MOT loading. A molasses phase of 12 ms followed the MOT loading to enhance the transfer efficiency of atoms into the ODT. In the final stage, atoms confined in the ODT were held for a variable time delay (dt) to measure the ODT lifetime. After this delay, the atoms were imaged using MOT beams detuned by -12 MHz for a 2 ms exposure. A second image was recorded 400 ms later for background subtraction. Each image was obtained as an average of ten repetitions. The decay of the ODT fluorescence signal with increasing hold time is shown in Fig. 5.13. The ODT remained visible for

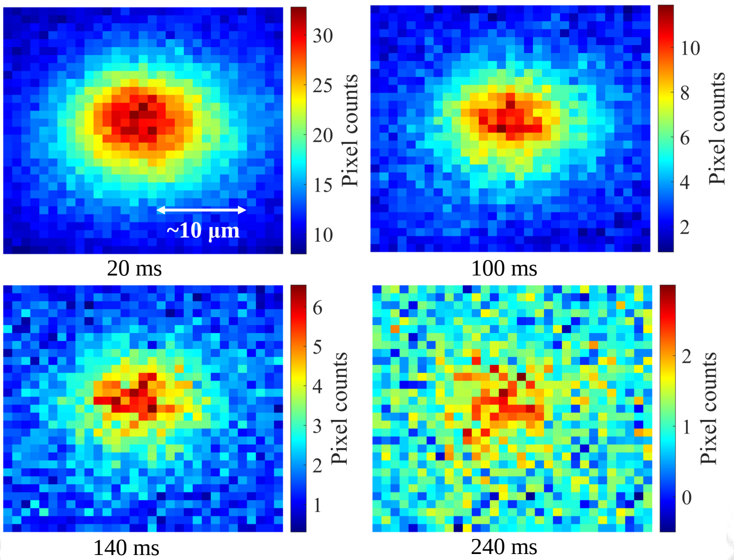

20 ms

100 ms

140 ms

240 ms

Figure 5.13: Fluorescence image (Background subtracted-average of 10) of the trapped atoms in ODT of beam waist 7.5 μm with various holding time (dt).

up to about 250 ms for this beam waist. The holding-time dependence of the integrated fluorescence (pixel sum) obtained from a 30 × 30 pixel region of interest for the ODT is shown in Fig. 5.14. A rapid initial loss during the first 40 ms is followed by a slower decay at longer hold times, indicating the presence of multiple loss mechanisms. The initial fast decay is attributed to density-dependent two-body collisions and the loss of atoms that are not fully thermalized immediately after loading into the tightly confining 7.5 μm waist trap. As the atomic density decreases, two-body losses become less significant, and the decay is dominated by one-body losses arising from collisions with the background gas.

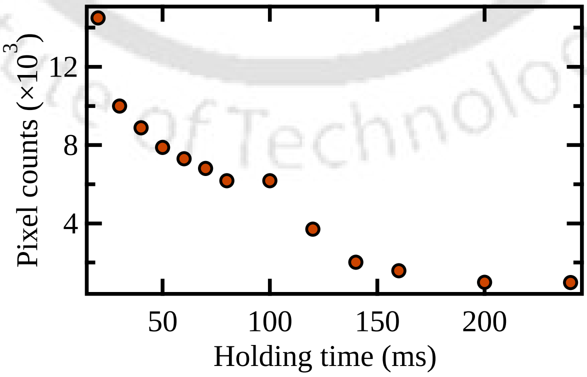

Figure 5.14: The holding-time dependence of the integrated fluorescence (pixel sum) measured in a 30 × 30 pixel region of interest for the ODT with 7.5 μm waist.

This transition results in the slower decay observed at longer hold times.

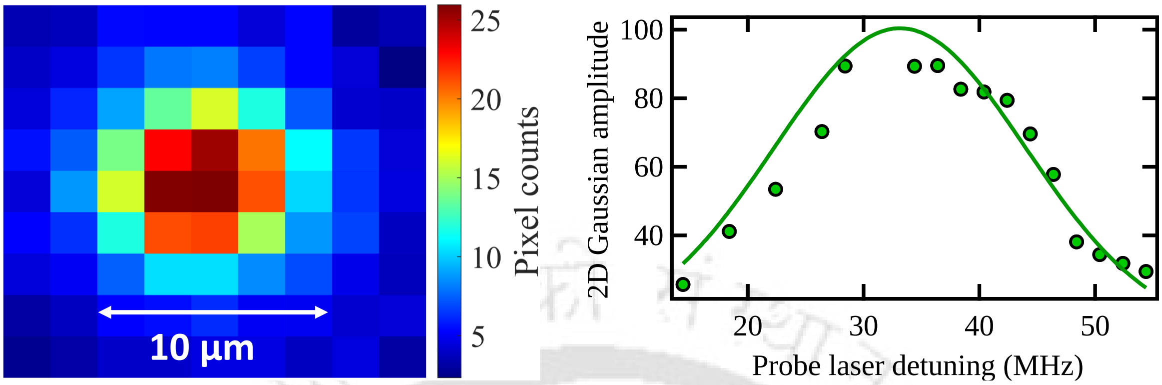

(a) (b)

Figure 5.15: (a) Fluorescence image (background subtracted-average of 20) of the optical dipole trap with a beam waist of 4.5 μm, obtained using a probe beam detuned by 35 MHz from the bare atomic resonance. (b) Integrated fluorescence (pixel sum) as a function of the probe frequency detuning from the bare resonance, measured within 8×8 pixel region of interest for the ODT with a 4.5 μm waist.

.

A smaller trap at 4.5 μm beam waist Next, we moved to the optical dipole trap with a beam waist of 4.5 μm. In this configuration, the input trap beam diameter before the objective was adjusted to approximately 2.2 mm. The calculated trap depth for this beam waist was about 2.9 mK at an input power of 45 mW. At this trap depth, the ODT could not be directly detected using the MOT beams with a detuning of -12 MHz due to the light shift of the $5S_{1/2}$, $F = 2 \rightarrow 5P_{3/2}$, $F' = 3$ transition. To overcome this limitation, a separate imaging probe beam was used for fluorescence imaging. The imaging beam was introduced along the orthogonal direction to the ODT beam.

This probe beam was derived from the zeroth-order output of the MOT AOM and passed through the AOM operated at 66 MHz in a dual-pass configuration. The dual-pass arrangement allowed precise control of the probe frequency relative to the atomic resonance without altering the beam alignment or fiber coupling. The experimental sequence was as follows: the MOT was first loaded for 2 s, followed by a 12 ms molasses phase to cool the atoms before transferring them into the ODT. After switching off the MOT beams, a waiting period of 20 ms was introduced to allow the MOT cloud to disperse. Subsequently, the ODT was imaged by scanning the probe frequency across the resonance with the imaging duration of 10 ms. The imaging beam had a diameter of approximately 15 mm, a power of 0.5 mW, and was used in a retro-reflected configuration. The ODT

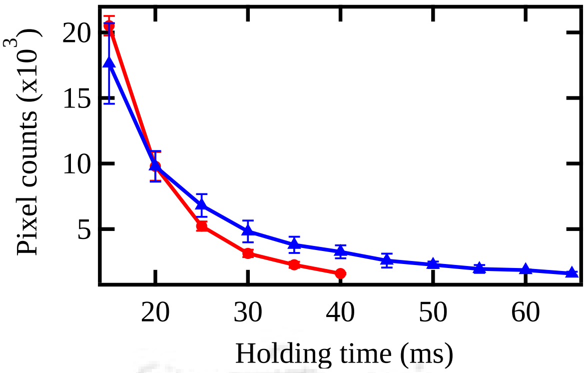

Figure 5.16: The holding-time dependence of the integrated fluorescence (pixel sum) measured within an 8×8 pixel region of interest for the ODT with a 4.5 μm waist. The blue line represents data recorded with the repumper beam on during the holding time, and the red line shows data without the repumper beam.

image shown in Fig. 5.15(a) represents the average of 20, with an exposure time of 10 ms, using a probe beam detuned by 35 MHz from the bare atomic resonance. The measured resonance curve obtained by varying the probe detuning is shown in Fig. 5.15(b). The ODT fluorescence image was fitted with a 2D Gaussian, and the fitted amplitude was plotted as a function of the probe frequency. The resonance peak appeared at approximately 35 MHz relative to the bare atomic transition. The spectrum in Fig. 5.15(b) corresponds to the excitation lineshape of atoms trapped in the optical dipole trap. The observed linewidth of ∼22 MHz is significantly larger than the natural linewidth of the D2 transition (6 MHz). This broadening is attributed to the inhomogeneous AC Stark shift experienced by atoms at different positions within the trap, resulting in a distribution of resonance frequencies. The spectrum is shifted by approximately 35 MHz to the blue of the bare atomic resonance. This shift arises from the differential light shift induced by the 803 nm trapping laser, where the ground state experiences a larger shift than the excited state. The observed displacement confirms that the fluorescence originates from trapped atoms and explains the choice of a 35 MHz probe detuning for imaging, which maximizes the trapped-atom signal.

The trap lifetime was further measured using the MOT beams for fluorescence imaging. For this purpose, the trap depth was reduced by lowering the ODT power to 30 mW so that the MOT beams could be used without excessive light shifts. The experimental timing sequence for this measurement is similar to that used for the 7.5 μm trap except for the imaging time. The ODT was imaged for 10 ms. The holding-time dependence of the integrated fluorescence (pixel sum) obtained from an 8×8 pixel region of interest for the

ODT with a 4.5 μm beam waist is shown in Fig. 5.16. A rapid initial loss is followed by a slower decay at longer hold times, indicating the presence of multiple loss mechanisms. The initial decay is attributed to density-dependent two-body collisions, while the slower long-time decay is dominated by one-body losses due to collisions with the background gas. Two experimental conditions were compared: with the repumper beam kept on (blue curve) and with the repumper beam turned off (red curve) during the holding period. The repumper is resonant with the transition $5S_{1/2}$, $F = 1 \rightarrow 5P_{3/2}$, $F' = 1$ in this case. Similar decay behavior was observed in both cases, indicating that the repumper has a negligible effect on the trap lifetime under the present experimental conditions.

Typically, atoms confined in an optical dipole trap exhibit lifetimes exceeding a second under ultrahigh-vacuum conditions. The observed reduction in lifetime for both beam sizes is likely due to heating caused by Raman scattering processes associated with the 803 nm trapping wavelength. Such off-resonant scattering induces recoil heating, which accelerates atom loss from the trap.

5.5.3 Single atom trapping

After achieving reliable operation of the optical dipole trapping at larger beam waists, we proceeded to the single-atom trapping experiment. The input trap beam diameter was increased to approximately 6.5 mm, corresponding to an ODT beam waist of 1.6 μm at the focus. In this stage, the CMOS camera was replaced with a CCD camera, as the latter offers higher sensitivity and includes a cooling option for the image sensor, which helps reduce the dark current noise and improve the signal-to-noise ratio. The optical dipole trap power was set to 3.5 mW, corresponding to a calculated trap depth of about 1.9 mK.

The MOT and repumper laser detunings were set to -12 MHz for the $F = 2 \rightarrow F' = 3$ transition and $+20$ MHz for the $F = 1 \rightarrow F' = 1$ transition, respectively. To operate in the weak loading regime, the dispenser current was reduced to 1 A. Additionally, the MOT and repumper beam diameters were decreased to about 7 mm to minimize scattered light reaching the imaging system. The powers of the MOT and repumping beam were around 2 mW and 1 mW on each arm, respectively. The MOT was loaded for 2 s with the ODT beam kept on during this period. After switching off the magnetic field, the MOT beams were left on for an additional 15 ms to induce photoassociation, ensuring that the trap contained either zero or one atom. The system was then allowed to wait for approximately 30 ms to allow untrapped background atoms to disperse before imaging.

Imaging was performed by illuminating the atoms with the MOT beams for 200 ms while

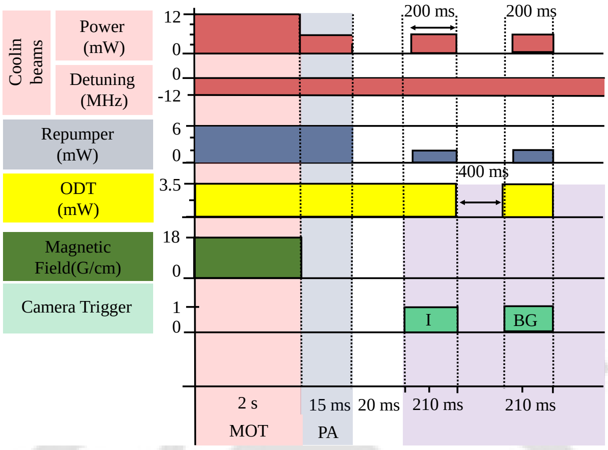

Figure 5.17: Time sequence for single atom loading in the ODT of 1.6 μm trap waist.

.

the camera exposure time was set to 210 ms. The powers of the MOT and repumper beams were reduced to about 1 mW and 0.5 mW per arm, respectively, to reduce background noise. A corresponding background image was also recorded for background subtraction after 400 ms of the first image. To confirm the single-atom loading probability, the entire sequence was repeated multiple times, and a histogram was generated from the integrated fluorescence counts within a 3×3 pixel region of interest. The resulting histogram, shown in Fig. 5.18(a), exhibited two distinct peaks corresponding to the background and single-atom events. The two peaks appeared close to each other due to the limited fluorescence collection efficiency and the relatively low sensitivity of the CCD camera.

The image shown in Fig. 5.18(b) represents the averaged signal obtained from multiple experimental runs with an exposure time of 200 ms. Single-shot atom detection was not possible in this system because the signal from a single atom was comparable to the background noise level.

5.5.4 Technical improvement required

The results presented in this work represent the preliminary stage of single-atom trapping experiments. Further detailed characterization could not be carried out with the current setup due to several technical limitations that require improvement. The foremost issue is the limited fluorescence collection efficiency of the imaging system. This can be signifi-

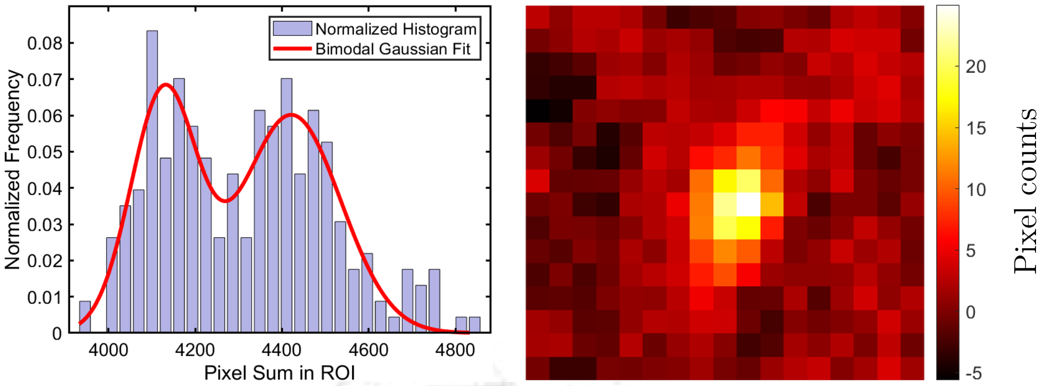

(a)

(b)

Figure 5.18: (a) Histogram of the integrated fluorescence (pixel sum) showing the probability distribution for single-atom loading events. The two peaks correspond to background counts (zero atom) and single-atom fluorescence, respectively. (b) Fluorescence image (background subtracted-average of 200) of the optical dipole trap with a beam waist of 1.6 μm.

cantly enhanced by replacing the present objective lens with a higher numerical aperture (NA) objective, typically around 0.5, which would improve both the spatial resolution and photon collection rate.

Another limitation arises from the sensitivity of the CCD camera used in the experiment. The current camera requires longer exposure times to detect the fluorescence signal from a single atom, which restricts time-resolved measurements, such as temperature determination, that require exposure durations in the microsecond range. To overcome this, a highly sensitive EMCCD camera will be integrated into the system to enable real-time observation and characterization of single atoms. In addition, the long optical path — over one meter — from the fiber output to the MOT chamber makes the beam alignment sensitive to mechanical drifts, resulting in day-to-day variations in MOT loading and fluorescence signal. Addressing these issues through improved and compact beam-delivery optics is expected to improve the stability and reproducibility of the trapping performance. Ongoing work focuses on implementing these upgrades to establish a robust, reliable experimental platform for future studies of single-atom control, cooling dynamics, and quantum-state manipulation.

5.6 Summary

In summary, this chapter presented the complete description of the experimental system developed for the laser cooling and trapping of Rb atoms. The design and upgradation of the vacuum system were discussed. The laser systems used for cooling, repumping, and optical dipole trapping were described in detail, along with the frequency stabilization schemes. Subsequently, the realization of the Rb MOT was demonstrated. Following the MOT, an optical molasses stage was implemented, during which we achieved a minimum atomic temperature of approximately 8 μK, confirming efficient sub-Doppler cooling. The optical dipole trapping of Rb atoms was then explored for different beam waist configurations of 7.5 μm, 4.5 μm, and 1.6 μm.

6

EIT in V+Inverted Ξ and Inverted Ξ Systems Using Rydberg State in Thermal Rb Atoms

Contents

6.1 Introduction

For atomic platforms, Rydberg excitation is key for quantum computation [45, 46] and simulation [114, 115], as it enables the multi-qubit operation through Rydberg blockade. In Rb, one of the most extensively used paths for Rydberg excitation is $5S_{1/2} \rightarrow 5P_{3/2}$ at 780 nm and $5P_{3/2} \rightarrow r$ (Rydberg states) at around 480 nm [116, 117]. However, the other scheme $5S_{1/2} \rightarrow 6P_{3/2}$ at 420 nm and $6P_{3/2} \rightarrow r$ at 1013 nm for Rydberg excitation is better for quantum computation. This is because (i) the narrow linewidth [102, 110] of the intermediate state ($6P_{3/2}$) reduces the decoherence rate for two-photon coherent Rydberg excitation, (ii) it is easier to produce a high-power 1013 nm laser.

The coherent Rydberg excitation requires frequency stability of Rydberg lasers, and a spectroscopic tool will be a good option for it. The stabilization of the blue laser is possible through saturated absorption spectroscopy (SAS) [102, 118–120]; however, the spectroscopy of the IR laser is not possible through SAS as there is no population in the excited state ($6P$), and hence EIT spectrum will be a good option for it.

EIT in thermal vapor for ^{87}Rb atoms in $5S_{1/2} \rightarrow 6P_{3/2} \rightarrow r$ (Rydberg state) inverted Ξ system has been studied before [121]. In the inverted Ξ system, probe wavelength ($\lambda_{\mathrm{p}} \approx$ 421 nm) is considerably shorter than the control laser wavelength ($\lambda_{\mathrm{c}} \approx$ 1003 nm) and termed an inverted Ξ system [122]. Note that the system with $\lambda_{\mathrm{p}} > \lambda_{\mathrm{c}}$ is termed an Ξ system [123–125]. The signal-to-noise ratio of the EIT spectrum for the inverted Ξ system happens to be poor because (i) absorption of blue probe is weak, (ii) in the weak (first order) probe limit [126] there is no EIT at room temperature, however, at high power (in higher order of probe) EIT exists [122, 127, 128]. For significant absorption of the blue probe [102] to detect a change caused by EIT, we need to heat the cell up to 80-90 ^{o}C. Further, we also need a blue-sensitive photodetector.

To improve the signal-to-noise ratio, we investigate EIT spectrum in thermal vapor for ^{87}Rb atoms in the V+inverted Ξ system $5S_{1/2} \rightarrow 5P_{3/2} + 5S_{1/2} \rightarrow 6P_{1/2} \rightarrow 69D_{3/2}$ with 780 nm probe and 421 nm and 1003 nm as control lasers. As the probe at 780 nm has stronger absorption as compared to the 421 nm probe, we get the EIT spectrum with a better signal-to-noise ratio even without heating the cell. Further, it also does not require a blue-sensitive photodetector. The probe ($5S_{1/2}, F = 2 \rightarrow 5P_{3/2}, F = 3$) absorption is monitored as scan of the $6P_{1/2} \rightarrow 69D_{3/2}$, 1003 nm control laser with fixed frequency of $5S_{1/2} \rightarrow 6P_{1/2}$ [121], 421 nm control laser. For completeness and comparison, we also study the inverted Ξ system in this work.

Further, the EIT has been theoretically studied in the V+Ξ system [129, 130] for various applications such as sub- and super-luminal light propagation [131], all-optical grating [132] but with limited experimental studies [133]. To the best of our knowledge, this is the first experimental study on the V+inverted Ξ system.

6.2 V+inverted Ξ system

6.2.1 Experimental setup

The energy-level diagram for the V+inverted Ξ system is shown in Fig. 6.1(a). The experiment is conducted in a cylindrical quartz vapor cell of diameter 25 mm and length $L = 5$ cm as shown in Fig. 6.1(b). The blue control beam is derived from a home-built external cavity diode laser (ECDL) with a linewidth < 500 kHz and output power of 70 mW, and the IR control beam is generated by another home-built ECDL of typical linewidth < 500 kHz, with a laser diode (Model: SM-1000-TO-300, Make: Innolume) that can deliver up to 200 mW power. The probe, blue control, and IR control beams are focused at the center of the vapor cell with typical beam waists of $w_{12}^{(0)} = 70\ \mu$m, $w_{13}^{(0)} = 30\ \mu$m and $w_{34}^{(0)} = 70\ \mu$m, respectively, and spatially overlapped in the vapor cell using dichroic mirrors. The 780 nm probe is stabilized at $5S_{1/2}$, $F = 2 \rightarrow 5P_{3/2}$, $F = 3$ transition using SAS. The IR control addresses various Rydberg levels, and its wavelength is monitored by a wavemeter (WS7-60, High Finesse) while the SAS setup is used to stabilize the blue control $5S_{1/2}$, $F = 2 \rightarrow 6P_{1/2}$, $F = 2$ transition [102]. The probe 780 nm and blue control beams are co-propagating, and the IR control beam is counter-propagating to both inside the cell. The absorption of the 780 nm probe beam is monitored on the photodetector and sent to the oscilloscope. For error signal generation, the IR laser was current-modulated at 20 kHz using a DigiLock lock-in module. The photodetector (Make: Thorlabs, Model: PDA36A-EC) signal was fed into the DigiLock for signal processing and generation of the corresponding error signal.

6.2.2 Results and discussion

We now discuss the spectrum of the V+inverted Ξ system. The transparency window (experimental and theoretical fitting) of the 780 nm probe with a scan of the IR control laser is shown in Fig. 6.2. For a low power of 780 nm probe and blue control lasers, the spectrum can be understood by population transfer to long-lived $69D_{3/2}$ Rydberg state through step excitation by blue and IR control lasers. As the blue laser is fixed to $5S_{1/2},\ F = 2 \rightarrow 6P_{1/2},\ F = 2$ transition, we observe a transparency window with a scan of the IR control laser. At lower probe power, we observe only one peak (unlike inverted Ξ system) even though IR control laser is scanning across both the hyperfine levels $6P_{1/2}$, $F = 1$ and $F = 2$. This is because only the zero velocity group of atoms can be in resonance with both the 780 nm probe and blue control laser. Even though the hyperfine separation between $F = 3$ and $F = 2$ of $5P_{3/2}$ and $F = 2$ and $F = 1$ of $6P_{1/2}$ is similar, due to different wavelengths of the probe and blue control lasers, there is no velocity group which can make the probe in resonance with $5S_{1/2},\ F = 2 \rightarrow 5P_{3/2},\ F = 2$ and also blue control $5S_{1/2},\ F = 2 \rightarrow 6P_{1/2},\ F = 1$. The signal-to-noise ratio $((V_{\text{signal}})^2/(V_{\text{noise}})^2)$ is 64 for the spectrum with eight averages, and 25 for the error signal without averaging. The generated error signal is shown in Fig. 6.3.

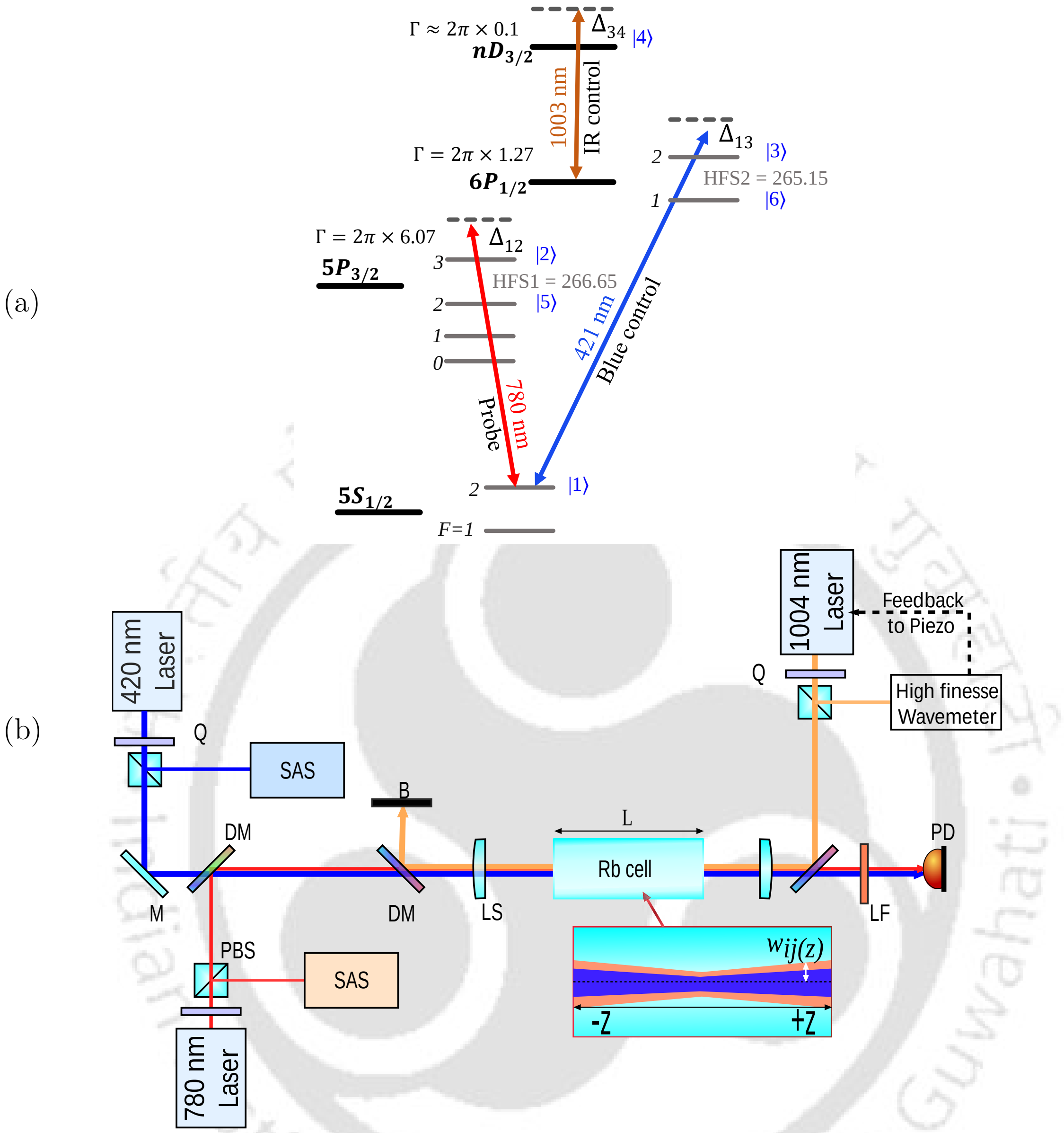

Figure 6.1: **(a)** Energy level diagram for V+inverted Ξ system in ^{87}Rb atoms. The numbers denoted are the hyperfine splitting of the levels in MHz. Γ is the population decay rate (in MHz) of corresponding levels. **(b)** Optics layout for the experimental setup. LS: Plano-convex lens, DM: Dichroic mirror, PD: Photodiode, Q: Half-wave plate, B: Beam dump, M: Mirror, LF: Spectral filter.

The V+inverted Ξ system can be modelled as four-level system $|1\rangle \rightarrow |2\rangle$ and $|1\rangle \rightarrow |3\rangle \rightarrow |4\rangle$ shown in Fig. 6.1(a). This system can be theoretically studied using density matrix analysis to compare it with experimental spectral features. The Hamiltonian for the system can be written as

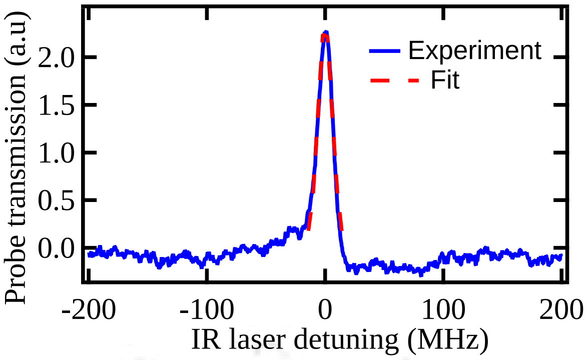

Figure 6.2: Probe transmission vs IR control laser detuning. Blue curve (experiment after averaging of eight traces) with the 780 nm probe, blue control, and IR control laser powers are 7 μW (calculated $\Omega_{12}^{(0)}$= 15 MHz), 0.2 mW (calculated $\Omega_{13}^{(0)}$= 8 MHz), and 40 mW (calculated $\Omega_{34}^{(0)}$= 16 MHz), respectively. Rabi frequencies ($\Omega_{ij}^{(0)}$) are calculated using the ARC package based on the cross-sectional average intensity for the minimum waist. Red curve (fitting): The extracted Rabi frequency from fitting $\Omega_{12}^{(0)} = 10$ MHz, $\Omega_{13}^{(0)} = 11$ MHz, and $\Omega_{34}^{(0)}$=16 MHz.

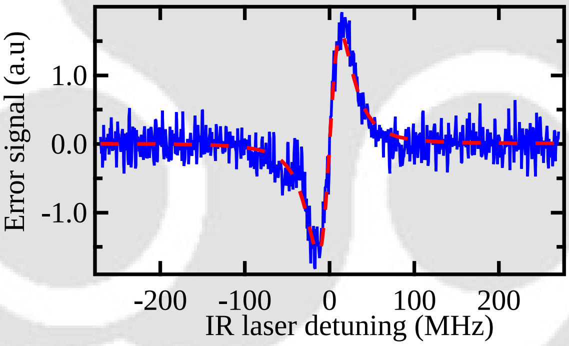

Figure 6.3: The generated error signal vs IR control laser detuning. Blue curve (experiment after averaging of four traces) with the 780 nm probe, blue control, and IR control laser powers are 40 μW, 2.3 mW, and 110 mW, respectively. The blue dot (red dashed line) is the experimental data (dispersive curve fit).

$$\begin{aligned} H = \hbar[&-\delta_{12}\left|2\right\rangle\left\langle 2\right| - \delta_{13}\left|3\right\rangle\left\langle 3\right| - (\delta_{13}+\delta_{34})\left|4\right\rangle\left\langle 4\right| \\ &+ \frac{\Omega_{12}}{2}\left|1\right\rangle\left\langle 2\right| + \frac{\Omega_{13}}{2}\left|1\right\rangle\left\langle 3\right| + \frac{\Omega_{34}}{2}\left|3\right\rangle\left\langle 4\right| + h.c.] \end{aligned} \tag{6.2.1}$$

where the $\delta_{12} = \Delta_{12} + k_{12}v$, $\delta_{13} = \Delta_{13} + k_{13}v$, and $\delta_{34} = \Delta_{34} - k_{34}v$ for the atoms moving with v velocity along the direction of the propagation of IR control laser. Here, $k_{12} = 1/780$ nm, $k_{13} = 1/421$ nm and $k_{34} = 1/1003$ nm and Δ_{12}, Δ_{13}, and Δ_{34} are detuning of the 780 nm, 421 nm, and 1003 nm lasers for stationary atoms. Ω_{12}, Ω_{13}, and Ω_{34} are the Rabi frequencies.

The dynamics of the system can be studied using the Liouville-von Neumann equation,

$$\frac{d\rho}{dt} = -\frac{i}{\hbar}[H, \rho] + L(\rho) \tag{6.2.2}$$

Here, $L(\rho)$ accounts for the spontaneous decay of atoms via various channels [59, 62, 134]. The above equation contains 16 coupled differential equations. We solve the above equation numerically with initial condition $\rho_{ij} = 0 \; \forall \; i$ and $j \in \{1, 2, 3, 4\}$ except $\rho_{11} = 1$, to find out the ρ_{21} whose imaginary part is related to the absorption of the 780 nm probe laser. We perform averaging for the longitudinal and transverse velocities with respect to the laser propagation direction. The longitudinal velocity effects ρ_{21} through Doppler effect and transverse velocity causes finite interaction time given as $2w_{ij}(z)/v_t$, where $w_{ij}(z)$ is beam waist at position z as shown in Fig. 6.1(b). To reduce computation time, we take a constant Rabi frequency in the cross-section of the laser beams and vary it along the propagation direction using the Gaussian beam propagation formula. The averaged ρ_{21} is given by

$$\begin{aligned}\rho_{21}^{\text{ave}} = A \int_{0}^{v_p} dv_t \int_{-v_p}^{v_p} dv_l \\ \times \int_{\frac{-L}{2}}^{\frac{L}{2}} dz \rho_{21}(v_t, v_l, \Omega_{12}(z), \Omega_{13}(z), \Omega_{34}(z)) v_t e^{-\frac{m(v_t^2+v_l^2)}{2k_BT}} \pi \times (w_{ij}(z))^2,\end{aligned} \tag{6.2.3}$$

where, $v_p = \sqrt{\frac{2k_BT}{m}}$, $A = \sqrt{1/2\pi}(m/k_BT)^{3/2}$ and $\Omega_{ij}(z) = \Omega_{ij}^{(0)}[1 + (z/z_R)^2]$. $\Omega_{ij}(z)$ is Rabi frequency at position z for $|i\rangle \rightarrow |j\rangle$ transition. L is the length of the Rb cell. The numerical integration is done with step size $\Delta v_t = \Delta v_l = 2$m/s and $\Delta z = L/8$.

We fit experimental data points (plotted with the blue curve) of Fig. 6.2 using the above numerical solution with $\Omega_{12}^{(0)}$, $\Omega_{13}^{(0)}$, and $\Omega_{34}^{(0)}$ fitting parameters. To reduce computation time, we use only 18 experimental data points in the fitting region from -14 MHz to 14 MHz. The fitting is shown with a red curve. There is a mismatch between the extracted Rabi frequencies from fitting and the calculated values. This could be due to misalignment of the laser beams, the presence of multiple magnetic sublevels, and the imperfect Gaussian beam shape of the lasers.

The transparency window splits when we increase the power of the 780 nm probe and blue control lasers, as shown in Fig. 6.4(a) due to Autler-Townes splitting [135]. With high power of 780 nm probe we see splitting of the main peak (near 0 MHz) and another small peak at ∼154 MHz as shown in Fig. 6.4(a). The peak at ∼154 MHz is due to moving atoms with velocity ∼112 m/s along the direction of propagation of the 780 nm probe and blue control lasers. The Doppler shift for this velocity will bring the blue control laser in resonance to $5S_{1/2},\ F = 2 \rightarrow 6P_{1/2},\ F = 1$ transition. The frequency of IR control laser for this velocity will be up-shifted by ∼ 111 MHz, and we need to increase the frequency by another ∼154 MHz to bring the IR laser in resonance with $6P_{1/2},\ F = 1 \rightarrow 69D_{3/2}$ transition.

For this velocity group, the 780 nm probe laser is Doppler shifted by approximately 143 MHz, bringing it close to resonance with the $5S_{1/2},\ F = 2 \rightarrow 5P_{3/2},\ F = 3$ transition. At high probe powers, power broadening increases the effective linewidth of the transition, allowing off-resonant coupling to the nearby $5S_{1/2},\ F = 2 \rightarrow 5P_{3/2},\ F = 2$ transition as well.

The splitting of the main peak is asymmetric because the 780 nm probe and blue control lasers are also driving other closely spaced hyperfine levels off-resonantly, causing a light shift of $5S_{1/2},\ F = 2$ resulting in the detuning for the transitions. These effects can be incorporated by including the nearby hyperfine levels, $5S_{1/2},\ F = 2$ and $6P_{1/2},\ F = 1$ with the following modified Hamiltonian.

$$\begin{aligned} H = \hbar[&-\delta_{12}\left|2\right\rangle\left\langle 2\right| - \delta_{13}\left|3\right\rangle\left\langle 3\right| - (\delta_{13}+\delta_{34})\left|4\right\rangle\left\langle 4\right| \\ &- (\delta_{12}+HFS1)\left|5\right\rangle\left\langle 5\right| - (\delta_{13}+HFS2)\left|6\right\rangle\left\langle 6\right| \\ &+ \frac{\Omega_{12}}{2}\left|1\right\rangle\left\langle 2\right| + \frac{\Omega_{13}}{2}\left|1\right\rangle\left\langle 3\right| + \frac{\Omega_{34}}{2}\left|3\right\rangle\left\langle 4\right| \\ &\frac{\Omega_{15}}{2}\left|1\right\rangle\left\langle 5\right| + \frac{\Omega_{16}}{2}\left|1\right\rangle\left\langle 6\right| + \frac{\Omega_{46}}{2}\left|6\right\rangle\left\langle 4\right| + h.c.] \end{aligned} \tag{6.2.4}$$

This Hamiltonian involves 36 coupled differential equations for the density matrix elements through Liouville-von Neumann equation. We follow a similar numerical procedure as described for the four-level system to find out ρ_{21}^{ave}. We plot ρ_{21}^{ave} vs IR laser detuning in Fig. 6.4(b) with the value of $\Omega_{12}^{(0)}$, $\Omega_{13}^{(0)}$, and $\Omega_{34}^{(0)}$ to match the spectral feature shown in Fig. 6.4(a). We also plot in Fig. 6.4(b) the case for the stationary atom to see the ideal case.

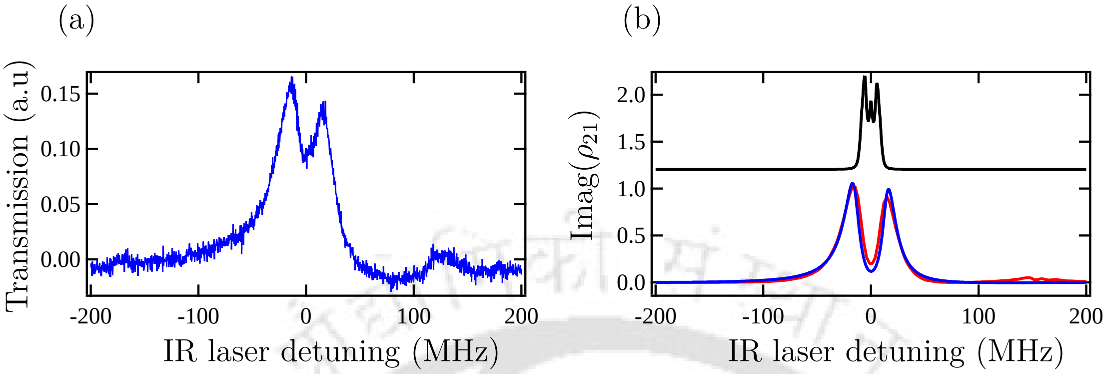

Figure 6.4: 780 nm probe transmission (arb.units) vs IR control detuning for high probe power **(a)** Experiment: The probe 780 nm probe, blue control, and IR control laser powers are 0.4 mW (calculated $\Omega_{12}^{(0)}$= 117 MHz), 7 mW (calculated $\Omega_{13}^{(0)}$= 45 MHz), and 40 mW (calculated $\Omega_{34}^{(0)}$ = 16 MHz), respectively. **(b)** Theory: The blue (red) solid line corresponds to theoretical prediction with Doppler averaging (stationary atoms) with $\Omega_{12}^{(0)}$= 50 MHz, $\Omega_{13}^{(0)}$= 45 MHz and $\Omega_{34}^{(0)}$= 16 MHz, shown to match experimental feature. The black curve also for stationary atoms with $\Omega_{12}^{(0)}$= 18 MHz, $\Omega_{13}^{(0)}$= 10 MHz and $\Omega_{34}^{(0)}$= 0.2 MHz.

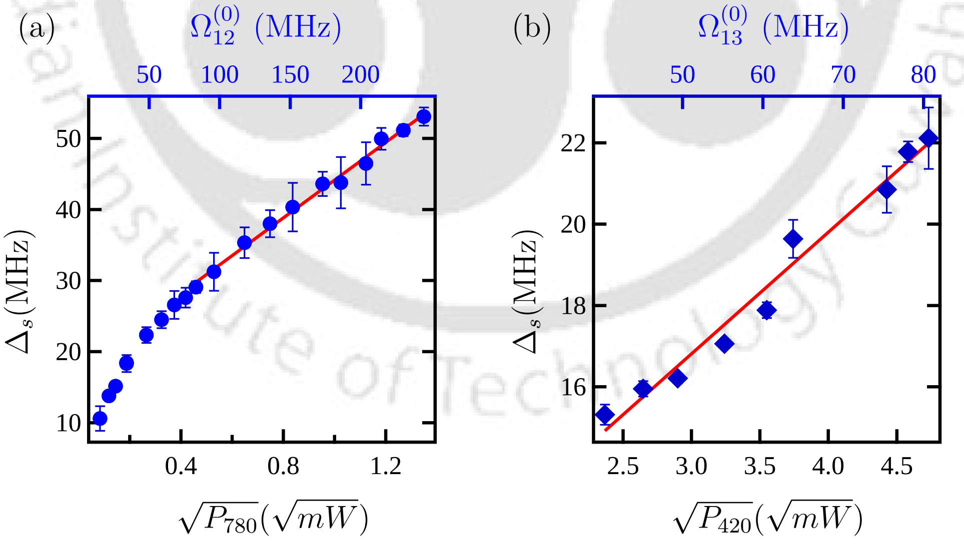

Figure 6.5: The separation (Δ_s) between doublet peaks measured under various **(a)** 780 nm probe power with blue control and IR control power of 7 mW ($\Omega_{13}^{(0)}$=45 MHz) and 40 mW ($\Omega_{34}^{(0)}$=16 MHz) respectively, and **(b)** blue control power with 780 nm probe and IR control power of 20 μW ($\Omega_{12}^{(0)}$=25 MHz) and 40 mW ($\Omega_{34}^{(0)}$=16 MHz) respectively.

The absorption profile can be further understood by the dressed state picture. In the regime of Autler-Townes splitting, i.e., with high power of the 780 nm probe and blue control lasers, three transparency peaks appear corresponding to the three dressed states:

$$|0\rangle = \frac{\Omega_{12}}{\sqrt{|\Omega_{12}|^2 + |\Omega_{13}|^2}}\,|3\rangle - \frac{\Omega_{13}}{\sqrt{|\Omega_{12}|^2 + |\Omega_{13}|^2}}\,|2\rangle\,, \tag{6.2.5}$$

$$|+\rangle = \frac{1}{\sqrt{2}}\frac{\Omega_{12}}{\sqrt{|\Omega_{12}|^2 + |\Omega_{13}|^2}}\,|3\rangle + \frac{1}{\sqrt{2}}\frac{\Omega_{13}}{\sqrt{|\Omega_{12}|^2 + |\Omega_{13}|^2}}\,|2\rangle + \frac{1}{\sqrt{2}}\,|1\rangle\,, \tag{6.2.6}$$

and

$$|-\rangle = \frac{1}{\sqrt{2}}\frac{\Omega_{12}}{\sqrt{|\Omega_{12}|^2 + |\Omega_{13}|^2}}\,|3\rangle + \frac{1}{\sqrt{2}}\frac{\Omega_{13}}{\sqrt{|\Omega_{12}|^2 + |\Omega_{13}|^2}}\,|2\rangle - \frac{1}{\sqrt{2}}\,|1\rangle\,. \tag{6.2.7}$$

The corresponding energy eigenvalues are

$$0, \qquad \frac{\sqrt{|\Omega_{12}|^2 + |\Omega_{13}|^2}}{2}, \qquad -\frac{\sqrt{|\Omega_{12}|^2 + |\Omega_{13}|^2}}{2}.$$

The three peaks are visible in Fig. 6.4(b) for a stationary atom (black curve) with a certain combination of Rabi frequencies, but with averaging the central peak disappears. The separation between the two extreme transparency peaks will be $\sqrt{|\Omega_{12}|^2 + |\Omega_{13}|^2}$. As the Rabi frequency happens to be proportional to the square root of power, we plot the separation between the doublet vs square root of power of the 780 nm probe and blue control laser in Fig. 6.5(a) and 6.5(b), respectively. When the Rabi frequency of one of the lasers is much higher than that of the other laser, it follows the linear behavior as shown by the red line in Fig. 6.5(a) and 6.5(b).

6.3 Inverted Ξ system

6.3.1 Experimental setup

The energy-level for the inverted Ξ system is shown in Fig. 6.6(a). In this case, the blue probe laser is stabilized to $5S_{1/2}$, $F = 2 \rightarrow 6P_{1/2}$, $F = 2$ transition using double resonance spectroscopy [118]. The IR coupling laser is scanning and addressing $6P_{1/2}$, $F = 1, 2 \rightarrow 69D_{3/2}$. The blue probe transmission is monitored using a blue-sensitive photodetector (Make: Thorlabs, Model: APD430A2/M). The experiment is conducted in a cylindrical quartz vapor cell of diameter 25 mm and length $L = 10$ cm as shown in Fig. 6.6(b) to increase the signal-to-noise ratio by increasing the interaction length. The vapor cell is heated to 80 °C.

6.3.2 Results and discussion

Now, we discuss the inverted Ξ-system where the probe at 421 nm is driving the $5S_{1/2}$, $F = 2 \rightarrow 6P_{1/2}$, $F = 2$ transition and IR control laser is scanning around $6P_{1/2}$, $F = 1, 2 \rightarrow 69D_{3/2}$. The transmission peak on the left side in Fig. 6.7 corresponds to the zero velocity group of the atom and the transition $6P_{1/2}$, $F = 2 \rightarrow 69D_{3/2}$. The right one corresponds to $v = 112$ m/s along propagation direction of blue probe laser and the transition $6P_{1/2}$, $F = 1 \rightarrow 69D_{3/2}$. The signal-to-noise ratio for the spectrum is 36 after eight averages, <1 without averaging, and 4 for the error signal without averaging.

To extract the linewidth and peak height, the spectrum is fitted with the sum of two Lorentzian functions. The linewidth and the transmission peak height (H) of the peak corresponding to the transition from $6P_{1/2}$, $F = 2 \rightarrow 69D_{3/2}$ with various coupling powers are shown in Fig. 6.8. The linewidth increases with increasing coupling power due to the power broadening mechanism, which fits well with the line. The minimum observed linewidth is around 8 MHz.

6.4 Conclusion

In conclusion, we have experimentally investigated the EIT spectrum using the Rydberg state in thermal Rb atoms with V+inverted Ξ system using $5S_{1/2} \rightarrow 5P_{3/2}$ and $5S_{1/2}$

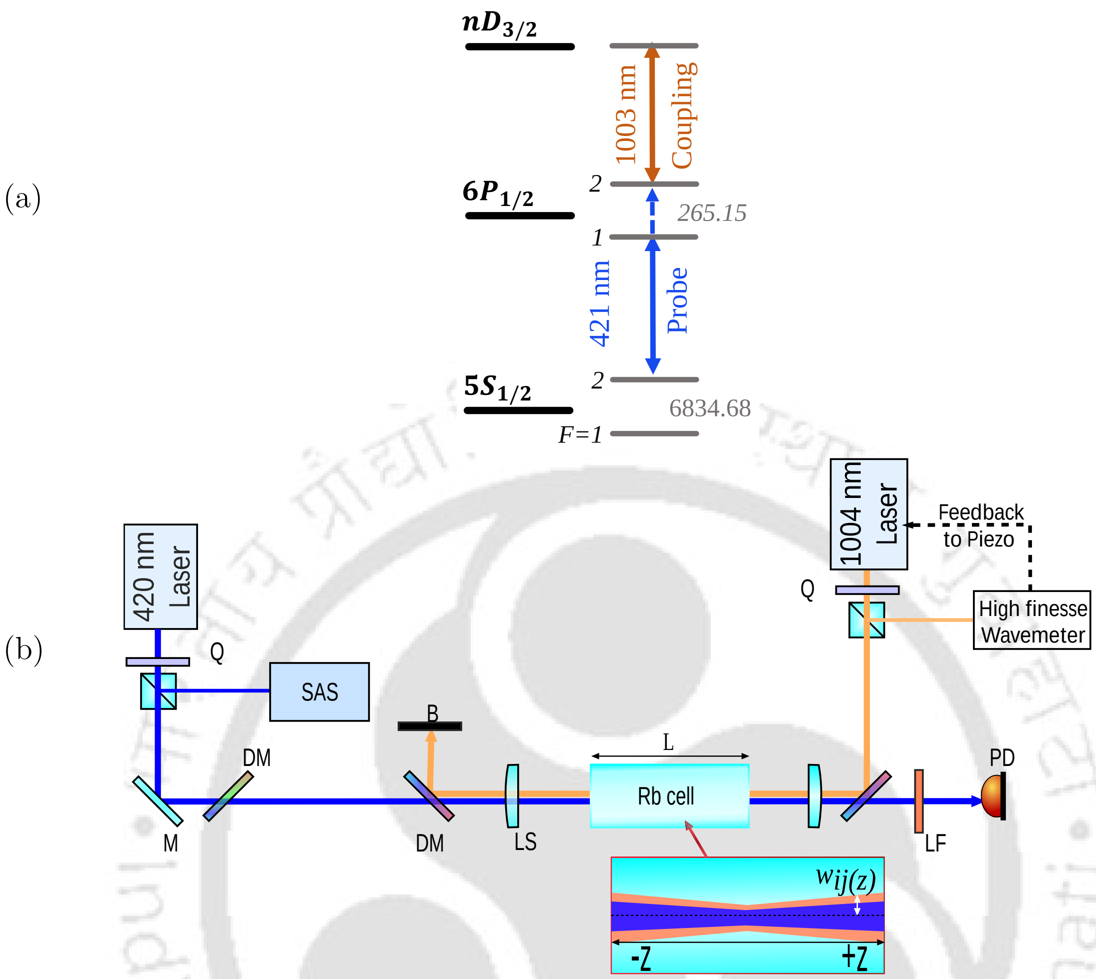

Figure 6.6: **(a)** Energy level diagram for inverted Ξ system in ^{87}Rb atoms. The numbers denoted are the hyperfine splitting of the levels in MHz. Γ is the population decay rate (in MHz) of corresponding levels. **(b)** Optics layout for the experimental setup. LS: Plano-convex lens, DM: Dichroic mirror, PD: Photodiode, Q: Half-wave plate, B: Beam dump, M: Mirror, LF: Spectral filter.

$\rightarrow 6P_{1/2} \rightarrow 69D_{3/2}$. For the V+inverted Ξ system, the probe laser at 780 nm gives a good EIT spectrum with a scan of IR Rydberg laser, even without heating of the Rb cell, and does not require a blue-sensitive photodetector to observe the EIT spectrum. The linewidth of the EIT spectrum is around 9 MHz. In comparison to the EIT spectrum in inverted Ξ (which requires heating of the Rb cell and blue-sensitive photodetector), the V+inverted Ξ system has a better signal-to-noise ratio with similar linewidth. The study will be very useful to stabilize (long term) the IR Rydberg laser for quantum computation and simulation and other proposed applications based upon the V+inverted Ξ systems.

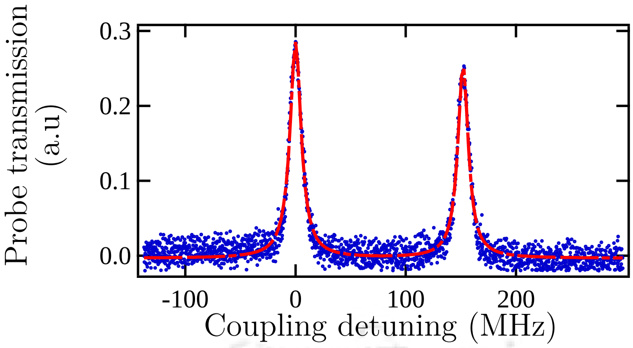

Figure 6.7: The observed probe transmission signal (after averaging of eight traces) for the excitation $5S_{1/2}$ $(F = 2) \rightarrow 6P_{1/2} \rightarrow 69D_{3/2}$ with probe and coupling power of 60 μW and 65 mW respectively. The right and left transmission peak corresponds to the hyperfine levels of $6P_{1/2}$ state, $F = 1$ and $F = 2$, respectively. The blue dot (red dashed line) is the experimental data (Lorentzian fit).

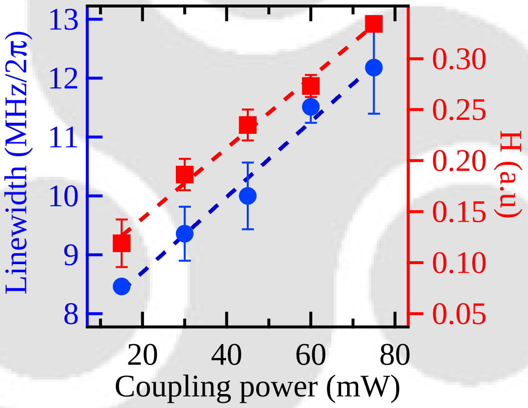

Figure 6.8: The experimental linewidth (blue circle) and the transmission peak height (H) (red square) of the transmission peak attributed to the transition $5S_{1/2}$ $(F = 2) \rightarrow 6P_{1/2}(F = 2) \rightarrow 69D_{3/2}$ as a function of the power of the coupling beam with probe power of 60 μW. The blue and red dashed lines are the line fitting for the linewidth and peak height, respectively.

The results presented in this chapter appear in the following publication:

Thilagaraj Ravi, Rajnandan Choudhury Das, Samir Khan, Heramb Vivek Bhusane, and Kanhaiya Pandey, **"EIT in V+inverted Ξ system using Rydberg state in thermal Rb atoms,"** *Optics Communications* **597** (2025) 132592.

7

Conclusions and Future Works

In this thesis, we demonstrated the laser cooling and trapping of Yb and Rb atoms and explored their relevance to neutral-atom quantum technologies, especially for quantum computing.

For Yb, we successfully loaded approximately 5×10^8 atoms in blue MOT at a temperature of around 11 mK and demonstrated efficient operation of the green MOT using both core-shell and center-shifted configurations with limited green laser power. The core-shell configuration showed the highest number of trapped atoms, reaching 3.4×10^8, which is significantly larger than the number obtained in the center-shifted configuration. These results are important for applications in portable optical clocks and for neutral-atom quantum computing using Yb tweezer arrays. We also attempted three-photon Rydberg excitation in Yb using the 556 nm, 423 nm, and 1137 nm lasers. Although a clear Rydberg signal has not yet been observed, the work reported in this thesis establishes the necessary optical and experimental setup, and the experience gained will guide future improvements toward successful Rydberg excitation.

For Rb, we developed a complete experimental system for cooling, trapping, and optical dipole trapping. We demonstrated the MOT operation, followed by an optical molasses stage, where we achieved a minimum temperature of about 8 μK, confirming efficient sub-Doppler cooling. We then studied optical dipole trapping for different beam-waist configurations, and the successful trapping of a single Rb atom in a tightly focused optical dipole trap was demonstrated. In the final part of the thesis, we studied electromagnetically induced transparency using Rydberg state in thermal rubidium. We compared the V+inverted Ξ system with the inverted Ξ system and showed that the V+inverted Ξ configuration provides a clear EIT signal without heating the vapor cell and without using a blue-sensitive detector. This configuration offers a better signal-to-noise ratio with a similar linewidth of about 9 MHz. These results will be useful for long-term stabilization of the IR Rydberg laser and for applications in quantum computation, quantum simulation, and Rydberg-based sensing.

Overall, this thesis establishes the essential cooling, trapping, and spectroscopy techniques required to build neutral-atom quantum systems using Yb and Rb. There are several directions in which this work can be extended.

For Yb, an array of optical tweezers can be developed for quantum computation, and this will be a major goal of the experiment. Achieving lower temperatures and higher densities in green MOT will support loading atoms into optical tweezers for quantum-computing applications. The three-photon Rydberg excitation pathway can be improved with higher laser power, better frequency stabilization, and improved beam alignment. A successful demonstration of Rydberg excitation in Yb will be useful for the implementation of multi-qubit gates in Yb atoms.

For Rb, the next step is to improve and optimize the setup of single-atom trapping and to extend the setup toward an array of individually addressable atoms. The platform can be extended to implement quantum gate operations. The Rydberg-EIT study in thermal rubidium can be used for robust frequency locking of the IR Rydberg laser. These techniques will support experiments involving multi-qubit operations using Rydberg excitation.

In the near future, the single-atom optical tweezer platform will be extended to multiple trapping sites using acousto-optic deflectors or spatial light modulators. This will enable the creation of one-dimensional and two-dimensional arrays of individually trapped atoms. Such arrays will provide a scalable architecture for neutral-atom quantum computing and will allow studies of atom rearrangement, site-resolved detection, and coherent control of multiple qubits. A major long-term objective is the implementation of Rydberg-mediated quantum gate operations between individually trapped atoms. This will require the integration of optical tweezers, high-fidelity single-atom imaging, and coherent excitation to Rydberg states. The realization of controlled two-qubit gates will enable the implementation of quantum algorithms and quantum simulation protocols. The techniques developed in this thesis provide the essential foundation for these future developments. In the long term, the techniques developed in this thesis can be combined to build a fully functional neutral-atom quantum platform. The integration of precise cooling, single-atom trapping, and Rydberg excitation forms a strong foundation for scalable neutral-atom quantum computation and quantum simulation.

A

Appendix

A.1 Home-assembled ECDL

Most of the lasers used in our lab are home-assembled external cavity diode laser systems (ECDL) that operate in Littrow configuration [90]. The laser system consists of a laser diode (LD) assembly, a grating mount with piezo, a thermoelectric cooler (TEC), and an electronic protection PCB, as shown in Fig. A.1. The diode assembly houses the LD along with an aspheric lens that collimates the emitted light. The slot in the diode assembly to accommodate an LD is around 9 mm in diameter. Since LDs are available in ϕ9 mm, ϕ5.6 mm, and ϕ3.8 mm packages, a mounting adapter is required when using the smaller ϕ5.6 mm or ϕ3.8 mm types. The package number refers to the flange diameter of the diode package. The diode is mounted in the assembly such that the major axis of the elliptical output profile is parallel to the optical table. This alignment can be ensured by positioning the square slot on the LD package flange parallel to the optical

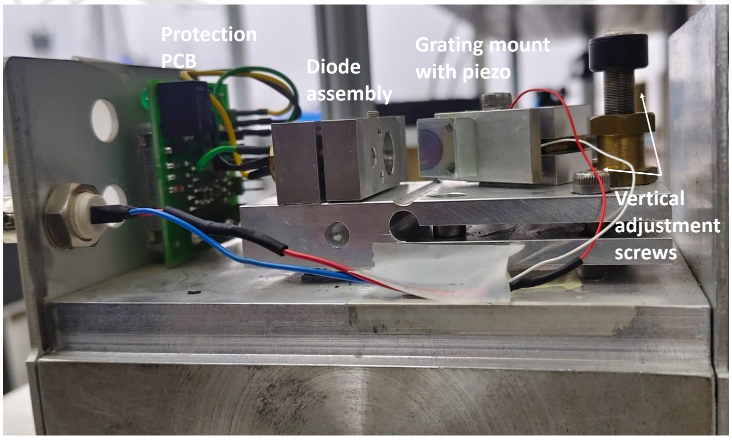

Figure A.1: Home assembled ECDL assembly.

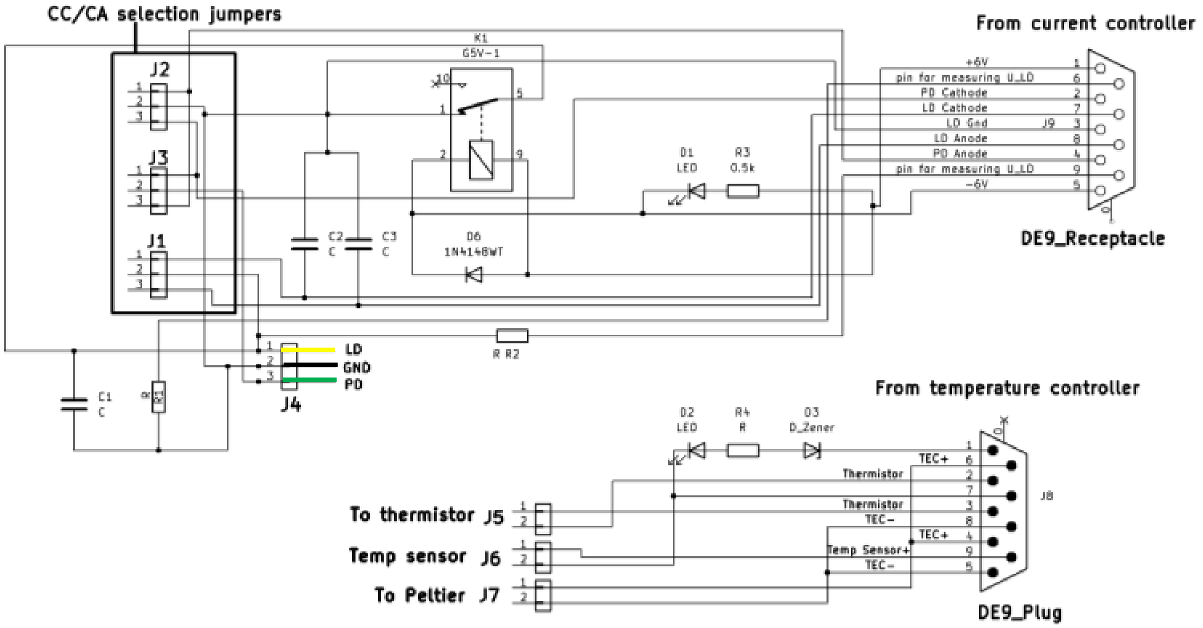

Figure A.2: Circuits of PCB of ECDL system.

table. The diode assembly accepts only the aspheric lens of outer diameter 9.2 mm with M9×0.5 thread. The holographic reflective grating is placed next to the diode assembly and positioned at an angle so that the first-order diffraction is directed back into the laser diode, while the zeroth-order reflection provides the output. The grating is oriented with its rulings parallel to the minor axis of the output beam. In this configuration, the first-order diffraction efficiency (which is directed back to the laser) is about 20–30%, as the grating rulings are parallel to the laser polarization. The grating is attached to the piezoelectric actuator that allows fine adjustment of the grating angle to actively control the laser frequency when voltage is applied. The horizontal and vertical alignment of the grating can be adjusted using the screws shown in Fig. A.1.

The electronic PCB contains two isolated circuits that interface the laser system with external temperature and current control units, as shown in Fig. A.2. The temperature circuit connects the thermoelectric cooler (TEC) and the thermistor to the temperature controller, which stabilizes the diode temperature. The current circuit delivers the drive current to the laser diode, and it also includes a relay that protects the laser diode from electrostatic discharge when the system is powered off. This relay just temporarily shorts all the legs of the laser diode until the current controller is powered on.

Laser diodes are mostly available in two packaging configurations, common cathode (CC) and common anode (CA), with an integrated photodiode. These configurations specify

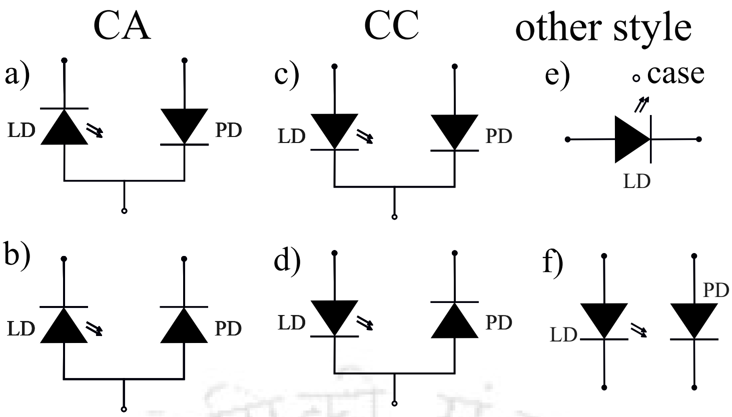

Figure A.3: Schematic representation of laser diode packaging configurations. (a) and (b) Common cathode (CC), where the cathode is electrically connected to the case. (c) and (d) Common anode (CA), where the anode is electrically connected to the case. (e) and (f) Alternative package style, where both LD and PD are not connected to the case.

whether the LD cathode (in CC) or the LD anode (in CA) is electrically connected to the metallic case of the diode. Most commercial current controllers support both configurations. These controllers provide three output terminals for biasing the laser diode, namely LD anode, LD cathode, and LD ground. In CC configuration, the LD is driven between the LD anode and LD ground outputs, with the driver operating in current-sourcing mode. In the CA configuration, the LD is driven between the LD ground and LD cathode outputs, with the driver operating in current-sinking mode. The distinction between sourcing and sinking arises from the electrical connection of the diode package to its case. For CC diodes, current must be sourced from the driver into the anode while the case is held at ground potential, whereas for CA diodes, the driver must sink current from the cathode because the case is tied to the anode held at ground potential. In both CC and CA configurations, the case of the laser diode is held at ground potential. This is done for two main reasons. First, the metallic case is in direct contact with the other mechanical parts of the laser assembly, so grounding it prevents unwanted current paths and reduces the risk of electrical shock or short circuits. Second, keeping the case grounded minimizes electrical noise and protects the laser diode from electrostatic discharge, which can easily damage the diode. There are other exceptional packages in which the laser diode terminals are not connected to the case. These package configurations are shown in Fig. A.3.

The current controller outputs are interfaced with the diode package with the help of the PCB through a three-pin connector (J4). The pin 1 (of J4) (yellow wire) is assigned to

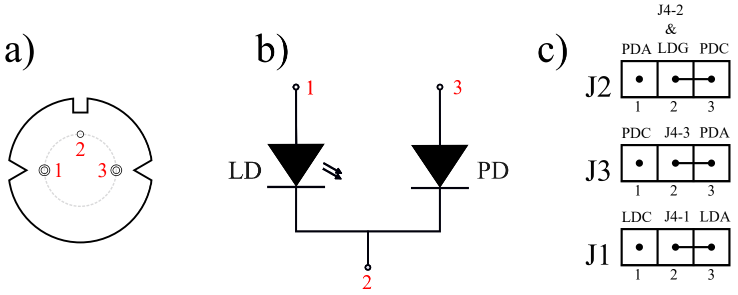

Figure A.4: Schematic representation of a common cathode (CC) laser diode package showing (a) the bottom view and (b) the pin configuration. (c) the appropriate setting of jumper J1, J2, and J3. Figure abbreviations: PDC: PD cathode output of the driver, PDA: PD anode output of the driver, LDA: LD anode output of the driver, LDC: LD cathode output of the driver, J4-1: pin 1 of J4 connector (Yellow wire), J4-2: pin 2 of J4 connector (Black wire), and J4-3: pin 3 of J4 connector (Green wire).

the laser diode terminal, pin 2 (of J4) (the black wire) to the common terminal (shared by both the LD/PD terminals and the case) which is always connected to the LD ground output, and pin 3 (of J4) (green wire) to the photodiode terminal. The three jumpers J1, J2, and J3 must be configured appropriately to operate with either the CC or CA package configuration. The jumpers set the mapping between the diode terminals (LD anode, LD cathode, PD anode, and PD cathode) and the driver outputs. Specifically, jumper J1 routes pin 1 of J4 (yellow wire, connected to the laser diode) either to LD anode output of the driver (in CC mode) or the LD cathode output of the driver (in CA mode). The jumper J2 connects the LD ground output to the photodiode terminal, which shares with the LD terminal. The jumper J3 determines whether pin 3 of J4 (green wire, connected to the photodiode) is assigned to the PD anode or cathode output of the driver.

For example, the typical pin arrangement of a common cathode (CC) laser diode is illustrated in Fig. A.4(a). In this configuration, terminals 1 and 3 correspond to the anodes of the laser diode and photodiode, respectively, while terminal 2 serves as the common ground that is connected to the case. To operate with this configuration, the jumper J1 should map the LD anode output of the driver to the Pin 1 of J4 (which will be connected to terminal 1 of LD), the jumper to J2 should map the LD Ground of the driver to Photo diode cathode output and, j3 should route the PD anode output to the pin 3 of J4 (which will be connected to terminal 3 of PD). The appropriate jumper setting is shown in Fig. A.4(c).

For packages in which the diodes are not electrically connected to the case, as shown in

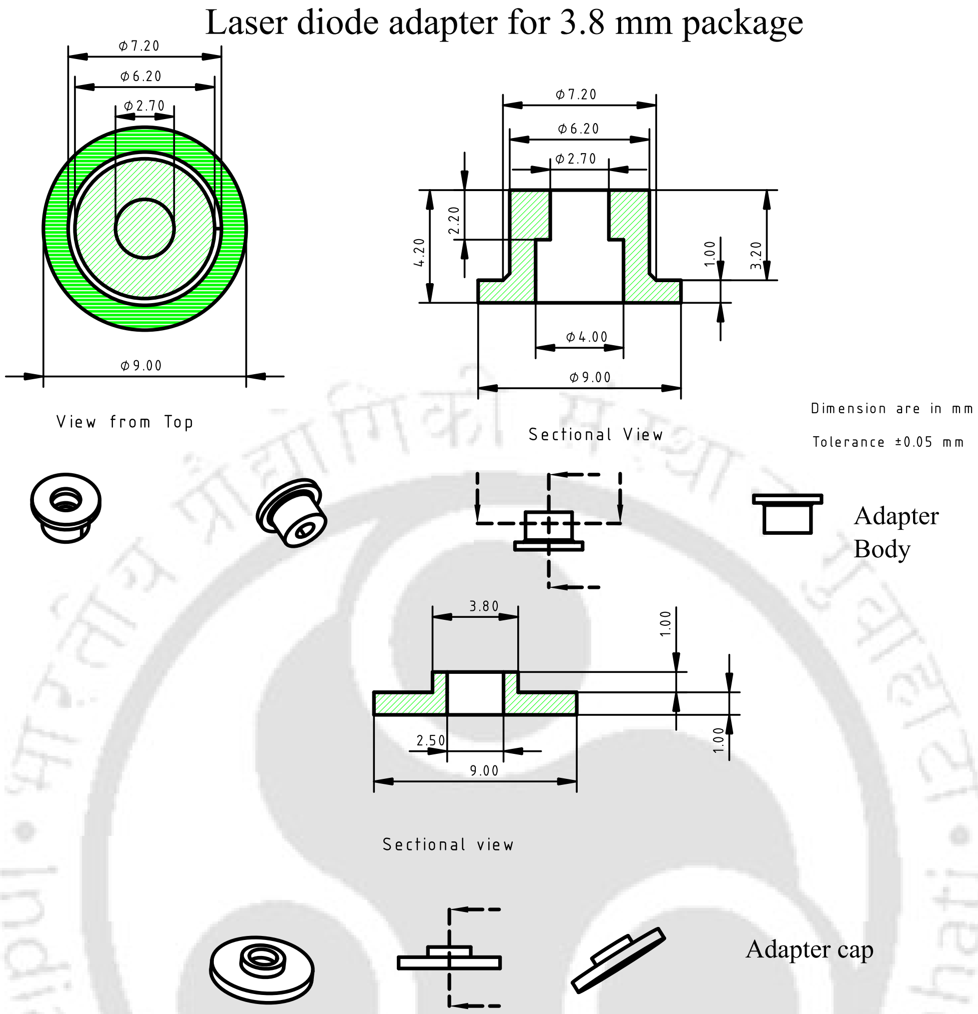

Figure A.5: Design of laser diode adapter for 3.8 mm package.

Fig. A.4(e) and A.4(f), the wiring connections must be adjusted appropriately. In such cases, the yellow and black wires must be connected to the correct terminals of the laser diode, depending on the package type.

Bibliography

[1] R. P. Feynman, International Journal of Theoretical Physics **21**, 467 (1982).

[2] D. Deutsch, Proceedings of the Royal Society A **400**, 97 (1985).

[3] P. W. Shor, in *Proceedings 35th Annual Symposium on Foundations of Computer Science* (IEEE, 1994) pp. 124–134.

[4] L. K. Grover, in *Proceedings of the 28th Annual ACM Symposium on Theory of Computing* (1996) pp. 212–219.

[5] C. Monroe, D. M. Meekhof, B. E. King, and D. J. Wineland, Phys. Rev. Lett. **75**, 4714 (1995).

[6] D. G. Cory, A. F. Fahmy, and T. F. Havel, Proceedings of the National Academy of Sciences **94**, 1634 (1997).

[7] N. A. Gershenfeld and I. L. Chuang, Science **275**, 350 (1997).

[8] D. P. DiVincenzo, Fortschritte der Physik **48**, 771 (2000).

[9] Y. Nakamura, Y. A. Pashkin, and J. S. Tsai, Nature **398**, 786 (1999).

[10] J. M. Martinis, S.-H. Nam, J. Aumentado, and C. Urbina, Phys. Rev. Lett. **89**, 117901 (2002).

[11] J. Koch, T. M. Yu, J. Gambetta, A. A. Houck, D. I. Schuster, J. Majer, A. Blais, M. H. Devoret, S. M. Girvin, and R. J. Schoelkopf, Phys. Rev. A **76**, 042319 (2007).

[12] A. P. M. Place, L. V. H. Rodgers, P. Mundada, B. M. Smitham, M. Fitzpatrick, Z. Leng, A. Premkumar, J. Bryon, A. Vrajitoarea, S. Sussman, G. Cheng, T. Madhavan, H. K. Babla, X. H. Le, Y. Gang, B. Jäck, A. Gyenis, N. Yao, R. J. Cava, N. P. de Leon, and A. A. Houck, Nature Communications **12**, 1779 (2021).

[13] S. Poorgholam-Khanjari, V. Seferai, P. Foshat, *et al.*, Scientific Reports **15**, 27113 (2025).

[14] P. Jurcevic, A. Javadi-Abhari, *et al.*, Quantum Science and Technology **6**, 025020 (2021).

[15] J. M. Gambetta, J. M. Chow, and M. Steffen, npj Quantum Information **3**, 2 (2017).

[16] K. Wright, K. M. Beck, S. Debnath, *et al.*, Nature Communications **10**, 5464 (2019).

[17] Y. Alexeev, D. Bacon, K. R. Brown, R. Calderbank, L. D. Carr, F. T. Chong, B. DeMarco, D. Englund, E. Farhi, B. Fefferman, A. V. Gorshkov, A. Houck, J. Kim, S. Kimmel, M. Lange, S. Lloyd, M. D. Lukin, D. Maslov, P. Maunz, C. Monroe, J. Preskill, M. Roetteler, M. J. Savage, and J. Thompson, PRX Quantum **2**, 017001 (2021).

[18] C. D. Bruzewicz, J. Chiaverini, R. McConnell, and J. M. Sage, Applied Physics Reviews **6**, 021314 (2019).

[19] M. Kjaergaard, M. E. Schwartz, J. Braumüller, P. Krantz, J. I.-J. Wang, S. Gustavsson, and W. D. Oliver, Annual Review of Condensed Matter Physics **11**, 369 (2020).

[20] D. Schwerdt, L. Peleg, Y. Shapira, N. Priel, Y. Florshaim, A. Gross, A. Zalic, G. Afek, N. Akerman, A. Stern, A. B. Kish, and R. Ozeri, Phys. Rev. X **14**, 041017 (2024).

[21] M. Akhtar, F. Bonus, F. R. Lebrun-Gallagher, *et al.*, Nature Communications **14**, 531 (2023).

[22] D. Kielpinski, C. Monroe, and D. J. Wineland, Nature **417**, 709 (2002).

[23] A. Ransford, M. S. Allman, J. Arkinstall, *et al.*, arXiv 10.48550/arXiv.2511.05465 (2025).

[24] R. Nigmatullin, K. Hémery, K. Ghanem, *et al.*, Nature Physics **21**, 1319 (2025).

[25] J. L. O'Brien, A. Furusawa, and J. Vučković, Nature Photonics **3**, 687 (2009).

[26] J. Bourassa, R. N. Alexander, *et al.*, Quantum **5**, 392 (2021).

[27] F. Flamini, N. Spagnolo, and F. Sciarrino, Reports on Progress in Physics **82**, 016001 (2018).

[28] N. Coste, D. A. Fioretto, N. Belabas, M. T. Rakher, M. Munsch, and A. Delteil, Nature Photonics **17**, 582 (2023).

[29] M. V. Larsen, J. E. Bourassa, S. Kocsis, *et al.*, Nature **642**, 587 (2025).

[30] B. Srivathsan, R. Gartman, R. J. A. Francis-Jones, P. J. Mosley, and J. Nunn, Phys. Rev. Lett. **135**, 150803 (2025).

[31] L. Childress and R. Hanson, MRS Bulletin **38**, 134 (2013).

[32] M. Saffman, Journal of Physics B: Atomic, Molecular and Optical Physics **49**, 202001 (2016).

[33] X. Wu, X. Liang, Y. Tian, F. Yang, C. Chen, Y.-C. Liu, M. K. Tey, and L. You, Chinese Physics B **30**, 020305 (2021).

[34] X.-F. Shi, Quantum Science and Technology **7**, 023002 (2022).

[35] M. Endres, H. Bernien, A. Keesling, H. Levine, E. R. Anschuetz, A. Krajenbrink, C. Senko, V. Vuletic, M. Greiner, and M. D. Lukin, Science **354**, 1024 (2016).

[36] D. Barredo, V. Lienhard, S. de Léséleuc, T. Lahaye, and A. Browaeys, Nature **561**, 79 (2018).

[37] D. Ohl de Mello, D. Schäffner, J. Werkmann, T. Preuschoff, L. Kohfahl, M. Schlosser, and G. Birkl, Phys. Rev. Lett. **122**, 203601 (2019).

[38] K. Singh, S. Anand, S. J. Evered, A. A. Geim, T. T. Wang, S. Ebadi, D. Bluvstein, M. Kalinowski, R. Samajdar, H. Pichler, S. Choi, M. D. Lukin, M. Greiner, and V. Vuletić, Science **380**, 1265 (2023).

[39] D. Bluvstein, H. Levine, G. Semeghini, T. T. Wang, S. Ebadi, A. Keesling, M. Kalinowski, R. Samajdar, A. Omran, H. Pichler, S. Choi, M. D. Lukin, M. Greiner, and V. Vuletić, Nature **604**, 451 (2022).

[40] T. M. Graham, Y. Song, J. Scott, C. Poole, D. Phung, S. Anand, S. J. Evered, G. Semeghini, R. Anglani, S. Ebadi, T. T. Wang, H. Levine, A. Keesling, A. Omran, R. Samajdar, H. Pichler, S. Choi, M. D. Lukin, M. Greiner, and V. Vuletić, Nature **604**, 457 (2022).

[41] T. M. Graham, M. Kwon, B. Grinkemeyer, Z. Marra, X. Jiang, M. T. Lichtman, Y. Sun, M. Ebert, and M. Saffman, Phys. Rev. Lett. **123**, 230501 (2019).

[42] T. Xia, M. Lichtman, K. Maller, A. W. Carr, M. J. Piotrowicz, L. Isenhower, and M. Saffman, Phys. Rev. Lett. **114**, 100503 (2015).

[43] D. Jaksch, J. I. Cirac, P. Zoller, S. L. Rolston, R. Côté, and M. D. Lukin, Phys. Rev. Lett. **85**, 2208 (2000).

[44] A. Kumar, T.-Y. Wu, F. Giraldo, and D. S. Weiss, Nature **561**, 83 (2018).

[45] H. Levine, A. Keesling, G. Semeghini, A. Omran, T. T. Wang, S. Ebadi, H. Bernien, M. Greiner, V. Vuletić, H. Pichler, and M. D. Lukin, Phys. Rev. Lett. **123**, 170503 (2019).

[46] H. Levine, A. Keesling, A. Omran, H. Bernien, S. Schwartz, A. S. Zibrov, M. Endres, M. Greiner, V. Vuletić, and M. D. Lukin, Phys. Rev. Lett. **121**, 123603 (2018).

[47] A. Cooper, J. P. Covey, I. S. Madjarov, S. G. Porsev, M. S. Safronova, and M. Endres, Phys. Rev. X **8**, 041055 (2018).

[48] A. Jenkins, J. W. Lis, A. Senoo, W. F. McGrew, and A. M. Kaufman, Phys. Rev. X **12**, 021027 (2022).

[49] W. Huie, L. Li, N. Chen, X. Hu, Z. Jia, W. K. C. Sun, and J. P. Covey, PRX Quantum **4**, 030337 (2023).

[50] S. Ma, A. P. Burgers, G. Liu, J. Wilson, B. Zhang, and J. D. Thompson, Phys. Rev. X **12**, 021028 (2022).

[51] N. Hinkley, J. A. Sherman, N. B. Phillips, M. Schioppo, N. D. Lemke, K. Beloy, M. Pizzocaro, C. W. Oates, and A. D. Ludlow, Science **341**, 1215 (2013).

[52] I. S. Madjarov, A. Cooper, A. L. Shaw, J. P. Covey, V. Schkolnik, T. H. Yoon, J. R. Williams, and M. Endres, Phys. Rev. X **9**, 041052 (2019).

[53] S. Ebadi, T. T. Wang, H. Levine, A. Keesling, *et al.*, Nature **595**, 227 (2021).

[54] D. Bluvstein *et al.*, Nature **626**, 58 (2024).

[55] J. F. Scholl *et al.*, Science **369**, 124 (2021).

[56] A. Computing, Atom computing demonstrates 1,225-qubit quantum processor, `https://atom-computing.com/press/1225qubit` (2023).

[57] S. E. Jones *et al.*, PRX Quantum **3**, 020331 (2022).

[58] D. Shylla, *Atomic Coherence Based Electromagnetic Wave Interferometry*, Ph.D. thesis, Indian Institute of Technology Guwahati (2023).

[59] R. C. Das, *Laser Cooling and Trapping of Rubidium using a Narrow Transition*, Ph.D. thesis, Indian Institute of Technology Guwahati (2024).

[60] H. J. Metcalf and P. van der Straten, *Laser Cooling and Trapping* (Springer, New York, 1999).

[61] C. Cohen-Tannoudji, J. Dupont-Roc, and G. Grynberg, *Atom–Photon Interactions: Basic Processes and Applications* (Wiley, New York, 1998).

[62] M. O. Scully and M. S. Zubairy, *Quantum Optics* (Cambridge University Press, Cambridge, 1997).

[63] R. Loudon, *The Quantum Theory of Light*, 3rd ed. (Oxford University Press, Oxford, 2000).

[64] L. Allen and J. H. Eberly, *Optical Resonance and Two-Level Atoms* (Dover Publications, New York, 1987).

[65] R. Grimm, M. Weidemüller, and Y. B. Ovchinnikov, Advances In Atomic, Molecular, and Optical Physics **42**, 95 (2000).

[66] B. E. A. Saleh and M. C. Teich, *Fundamentals of Photonics*, 3rd ed. (Wiley, Hoboken, 2019).

[67] C.-Y. Shih and M. S. Chapman, Phys. Rev. A **87**, 063408 (2013).

[68] M. E. Shea and D. J. Gauthier, Phys. Rev. A **96**, 027401 (2017).

[69] C.-Y. Shih, *Studies of Cold Atoms in Optical Dipole Traps*, Ph.D. thesis, Georgia Institute of Technology (2013).

[70] A. Kramida, Y. Ralchenko, J. Reader, and N. A. Team, Nist atomic spectra database (ver. 5.10), National Institute of Standards and Technology (2022), available at `https://physics.nist.gov/asd`.

[71] D. A. Steck, Rubidium 87 d line data (2003).

[72] S. J. M. Kuppens, K. L. Corwin, K. W. Miller, T. E. Chupp, and C. E. Wieman, Phys. Rev. A **62**, 013406 (2000).

[73] N. Schlosser, G. Reymond, and P. Grangier, Phys. Rev. Lett. **89**, 023005 (2002).

[74] T. Grünzweig, A. Hilliard, M. McGovern, and M. F. Andersen, Nature Physics **6**, 951 (2010).

[75] M. O. Brown, T. Thiele, C. Kiehl, T.-W. Hsu, and C. A. Regal, Phys. Rev. X **9**, 011057 (2019).

[76] A. Gaëtan, Y. Miroshnychenko, T. Wilk, A. Chotia, M. Viteau, D. Comparat, P. Pillet, A. Browaeys, and P. Grangier, Nature Physics **5**, 115 (2009).

[77] E. Urban, T. A. Johnson, T. Henage, L. Isenhower, D. D. Yavuz, T. G. Walker, and M. Saffman, Nature Physics **5**, 110 (2009).

[78] N. Šibalić and C. S. Adams, *Rydberg Physics* (IOP Publishing, 2018).

[79] D. Okuno, *Single ytterbium atoms in an optical tweezer array: high-resolution spectroscopy, single-photon Rydberg excitation, and a scheme for nondestructive detection*, Ph.D. thesis, Kyoto University (2022).

[80] L. Béguin, A. Vernier, R. Chicireanu, T. Lahaye, and A. Browaeys, Phys. Rev. Lett. **110**, 263201 (2013).

[81] T. Wilk, A. Gaëtan, C. Evellin, J. Wolters, Y. Miroshnychenko, P. Grangier, and A. Browaeys, Phys. Rev. Lett. **104**, 010502 (2010).

[82] L. Isenhower, E. Urban, X. L. Zhang, A. T. Gill, T. Henage, T. A. Johnson, T. G. Walker, and M. Saffman, Phys. Rev. Lett. **104**, 010503 (2010).

[83] K. L. Butler, *A Dual Species MOT of Yb and Cs*, Ph.D. thesis, Durham University (2014), durham Theses.

[84] A. Guttridge, *Photoassociation of Ultracold CsYb Molecules and Determination of Interspecies Scattering Lengths*, Ph.D. thesis, Durham University (2018), durham Theses.

[85] E. Wodey, R. J. Rengelink, C. Meiners, E. M. Rasel, and D. Schlippert, Journal of Physics B: Atomic, Molecular and Optical Physics **54**, 035301 (2021).

[86] F. Scazza, Probing SU(N)-symmetric orbital interactions with ytterbium fermi gases in optical lattices (2015).

[87] K. Pandey, *Laser Cooling and Trapping of Yb Towards High-Precision Measurements*, Ph.D. thesis, Indian Institute of Science, Bengaluru, India (2010).

[88] A. Chikkatur, *Colliding and Moving Bose-Einstein Condensates: Studies of Superfluidity and Optical Tweezers for Condensate Transport*, Ph.D. thesis, Massachusetts Institute of Technology, Cambridge, USA (2002).

[89] S. L. Kemp, *Laser Cooling and Optical Trapping of Ytterbium*, Ph.D. thesis, Durham University (2017).

[90] L. Ricci, M. Weidemüller, T. Esslinger, A. Hemmerich, C. Zimmermann, V. Vuletić, W. König, and T. W. Hänsch, Optics Communications **117**, 541 (1995).

[91] N. Poli, F.-Y. Wang, M. G. Tarallo, A. Alberti, M. Prevedelli, and G. M. Tino, Phys. Rev. Lett. **106**, 038501 (2011).

[92] A. W. Young, W. J. Eckner, N. Schine, A. M. Childs, and A. M. Kaufman, Science **377**, 885 (2022).

[93] J. T. Wilson, S. Saskin, Y. Meng, S. Ma, R. Dilip, A. P. Burgers, and J. D. Thompson, Phys. Rev. Lett. **128**, 033201 (2022).

[94] A. P. Burgers, S. Ma, S. Saskin, J. Wilson, M. A. Alarcón, C. H. Greene, and J. D. Thompson, PRX Quantum **3**, 020326 (2022).

[95] T. Kuwamoto, K. Honda, Y. Takahashi, and T. Yabuzaki, Phys. Rev. A **60**, R745 (1999).

[96] K. Pandey, K. D. Rathod, A. K. Singh, and V. Natarajan, Phys. Rev. A **82**, 043429 (2010).

[97] T. Yang, K. Pandey, M. S. Pramod, F. Leroux, C. C. Kwong, E. Hajiyev, Z. Y. Chia, B. Fang, and D. Wilkowski, The European Physical Journal D **69**, 226 (2015).

[98] M. Lu, S. H. Youn, and B. L. Lev, Phys. Rev. A **83**, 012510 (2011).

[99] T. Maier, H. Kadau, M. Schmitt, A. Griesmaier, and T. Pfau, Opt. Lett. **39**, 3138 (2014).

[100] D. C. McKay, D. Jervis, D. J. Fine, J. W. Simpson-Porco, G. J. A. Edge, and J. H. Thywissen, Phys. Rev. A **84**, 063420 (2011).

[101] P. M. Duarte, R. A. Hart, J. M. Hitchcock, T. A. Corcovilos, T.-L. Yang, A. Reed, and R. G. Hulet, Phys. Rev. A **84**, 061406 (2011).

[102] R. C. Das, D. Shylla, A. Bera, and K. Pandey, Journal of Physics B: Atomic, Molecular and Optical Physics **56**, 025301 (2023).

[103] Y. Miyazawa, R. Inoue, H. Matsui, K. Takanashi, and M. Kozuma, Phys. Rev. A **103**, 053122 (2021).

[104] A. Guttridge, S. A. Hopkins, S. L. Kemp, D. Boddy, R. Freytag, M. P. A. Jones, M. R. Tarbutt, E. A. Hinds, and S. L. Cornish, Journal of Physics B: Atomic, Molecular and Optical Physics **49**, 145006 (2016).

[105] A. Yamaguchi, S. Uetake, and Y. Takahashi, Applied Physics B **91**, 57 (2008).

[106] J. Lee, J. H. Lee, J. Noh, and J. Mun, Phys. Rev. A **91**, 053405 (2015).

[107] R. C. Das, T. Ravi, S. Khan, and K. Pandey, Phys. Rev. A **109**, 063107 (2024).

[108] C. Halter, A. Miethke, C. Sillus, A. Hegde, and A. Görlitz, Journal of Physics B: Atomic, Molecular and Optical Physics **56**, 055001 (2023).

[109] D. Okuno, Y. Nakamura, T. Kusano, Y. Takasu, N. Takei, H. Konishi, and Y. Takahashi, Journal of the Physical Society of Japan **91**, 084301 (2022).

[110] J. Lampen, H. Nguyen, L. Li, P. R. Berman, and A. Kuzmich, Phys. Rev. A **98**, 033411 (2018).

[111] N. Schlosser, G. Reymond, I. Protsenko, and P. Grangier, Nature **411**, 1024 (2001).

[112] U. Schünemann, H. Engler, R. Grimm, M. Weidemüller, and M. Zielonkowski, Review of Scientific Instruments **70**, 242 (1999).

[113] R. C. Das, T. Ravi, S. Khan, and K. Pandey, Phys. Rev. A **110**, 033101 (2024).

[114] P. Scholl, M. Schuler, H. J. Williams, A. A. Eberharter, D. Barredo, K.-N. Schymik, V. Lienhard, L.-P. Henry, T. C. Lang, T. Lahaye, A. M. Läuchli, and A. Browaeys, Nature **595**, 233 (2021).

[115] G. Bornet, G. Emperauger, C. Chen, F. Machado, S. Chern, L. Leclerc, B. Gély, Y. T. Chew, D. Barredo, T. Lahaye, N. Y. Yao, and A. Browaeys, Phys. Rev. Lett. **132**, 263601 (2024).

[116] S. B. S., S. K. Barik, S. Chaudhuri, and S. Roy, Opt. Continuum **1**, 1176 (2022).

[117] S. Baburaj Sheela, S. Kanti Barik, V. Shenoy, S. Chandak, R. Nath, and S. Roy, New Journal of Physics **27**, 083202 (2025).

[118] E. O. Nyakang'o, D. Shylla, V. Natarajan, and K. Pandey, Journal of Physics B: Atomic, Molecular and Optical Physics **53**, 095001 (2020).

[119] E. O. Nyakang'o and K. Pandey, Phys. Rev. A **103**, 013107 (2021).

[120] C. Glaser, F. Karlewski, J. Kluge, J. Grimmel, M. Kaiser, A. Günther, H. Hattermann, M. Krutzik, and J. Fortágh, Phys. Rev. A **102**, 012804 (2020).

[121] E. Brekke and C. Umland, J. Opt. Soc. Am. B **40**, 2758 (2023).

[122] T.-L. Chen, S.-Y. Chang, Y.-J. Huang, K. Shukla, Y.-C. Huang, T.-H. Suen, T.-Y. Kuan, J.-T. Shy, and Y.-W. Liu, Phys. Rev. A **101**, 052507 (2020).

[123] D. Li, G. Bian, J. Miao, P. Wang, Z. Meng, L. Chen, L. Huang, and J. Zhang, Phys. Rev. A **103**, 063305 (2021).

[124] Z.-S. He, J.-H. Tsai, Y.-Y. Chang, C.-C. Liao, and C.-C. Tsai, Phys. Rev. A **87**, 033402 (2013).

[125] H. S. Moon and H.-R. Noh, J. Opt. Soc. Am. B **29**, 1557 (2012).

[126] K. Pandey, Phys. Rev. A **87**, 043838 (2013).

[127] A. Urvoy, C. Carr, R. Ritter, C. S. Adams, K. J. Weatherill, and R. Löw, Journal of Physics B: Atomic, Molecular and Optical Physics **46**, 245001 (2013).

[128] Y. Zhu, S. Ghosh, S. B. Cahn, M. J. Jewell, D. H. Speller, and R. H. Maruyama, Phys. Rev. A **105**, 042808 (2022).

[129] V. Bharti and V. Natarajan, Optics Communications **356**, 510 (2015).

[130] A. Kaur, N. Singh, and P. Kaur, The European Physical Journal D **72**, 109 (2018).

[131] V. Bharti and V. Natarajan, Optics Communications **392**, 180 (2017).

[132] F. Bozorgzadeh and M. Sahrai, Phys. Rev. A **98**, 043822 (2018).

[133] J. Yuan, S. Dong, C. Wu, L. Wang, L. Xiao, and S. Jia, Opt. Express **28**, 23820 (2020).

[134] W. T. Rhodes, T. Asakura, K.-H. Brenner, T. W. Hänsch, T. Kamiya, F. Krausz, B. Monemar, H. Venghaus, H. Weber, and H. Weinfurter, eds., Quantum interference in atomic systems: Mathematical formalism, in *Quantum Interference and Coherence: Theory and Experiments* (Springer New York, New York, NY, 2005) pp. 47–84.

[135] E. O. Nyakang'o, D. Shylla, K. Indumathi, and K. Pandey, The European Physical Journal D **74**, 187 (2020).